

**STATISTICAL ANALYSIS OF ENSEMBLES OF  
NONREGULAR SHAPES**

by

Manasi Prakash Datar

A dissertation submitted to the faculty of  
The University of Utah  
in partial fulfillment of the requirements for the degree of

Doctor of Philosophy

in

Computing

School of Computing

The University of Utah

August 2016

Copyright © Manasi Prakash Datar 2016

All Rights Reserved

# The University of Utah Graduate School

## STATEMENT OF DISSERTATION APPROVAL

The dissertation of Manasi Prakash Datar  
has been approved by the following supervisory committee members:

<u>Ross Whitaker</u>	, Chair	<u>09/22/2014</u> Date Approved
<u>Guido Gerig</u>	, Member	<u>10/13/2014</u> Date Approved
<u>P Thomas Fletcher</u>	, Member	<u>10/24/2014</u> Date Approved
<u>Suresh Venkatasubramanian</u>	, Member	<u>11/21/2014</u> Date Approved
<u>Martin Styner</u>	, Member	<u>12/10/2014</u> Date Approved

and by Ross Whitaker, Chair/Dean of  
the Department/College/School of Computing

and by David B. Kieda, Dean of The Graduate School.

## ABSTRACT

Statistical shape analysis has emerged as an important tool for the quantitative analysis of anatomy in many medical imaging applications. The correspondence based approach to evaluate shape variability is a popular method, based on comparing configurations of carefully placed landmarks on each shape. In recent years, methods for automatic placement of landmarks have enhanced the ability of this approach to capture statistical properties of shape populations. However, biomedical shapes continue to present considerable difficulties in automatic correspondence optimization due to inherent geometric complexity and the need to correlate shape change with underlying biological parameters. This dissertation addresses these technical difficulties and presents improved shape correspondence models.

In particular, this dissertation builds on the *particle-based modeling* (PBM) framework described by Joshua Cates' 2010 Ph.D. dissertation. In the PBM framework, correspondences are modeled as a set of dynamic points or a *particle system*, positioned automatically on shape surfaces by optimizing entropy contained in the model, with the idea of balancing model simplicity against accuracy of the particle system representation of shapes. This dissertation is a collection of four papers that extend the PBM framework to include shape regression and longitudinal analysis and also adds new methods to improve modeling of complex shapes. It also includes a summary of two applications from the field of orthopaedics.

Technical details of the PBM framework are provided in Chapter 2, after which the first topic related to the study of shape change over time is addressed (Chapters 3 and 4). In analyses of normative growth or disease progression, shape regression models allow characterization of the underlying biological process while also facilitating comparison of a sample against a normative model. The first paper introduces a shape regression model into the PBM framework to characterize shape variability due to an underlying biological parameter. It further confirms the statistical significance of this relationship via systematic permutation testing. Simple regression models are, however, not sufficient to leverage information provided by longitudinal studies. Longitudinal studies collect data at multiple time points for each participant and have the potential to provide a rich picture of the anatomical changes occurring during development, disease progression, or recovery. The

second paper presents a linear-mixed-effects (LME) shape model in order to fully leverage the high-dimensional, complex features provided by longitudinal data. The parameters of the LME shape model are estimated in a hierarchical manner within the PBM framework.

The topic of geometric complexity present in certain biological shapes is addressed next (Chapters 5 and 6). Certain biological shapes are inherently complex and highly variable, inhibiting correspondence based methods from producing a faithful representation of the average shape. In the PBM framework, use of Euclidean distances leads to incorrect particle system interactions while a position-only representation leads to incorrect correspondences around sharp features across shapes. The third paper extends the PBM framework to use efficiently computed geodesic distances and also adds an entropy term based on the surface normal. The fourth paper further replaces the position-only representation with a more robust distance-from-landmark feature in the PBM framework to obtain isometry invariant correspondences.

Finally, the above methods are applied to two applications from the field of orthopaedics. The first application uses correspondences across an ensemble of human femurs to characterize morphological shape differences due to femoroacetabular impingement. The second application involves an investigation of the short bone phenotype apparent in mouse models of multiple osteochondromas. Metaphyseal volume deviations are correlated with deviations in length to quantify the effect of cancer toward the apparent shortening of long bones (femur, tibia-fibula) in mouse models.

*Aai, Baba... I made it-again!*

# CONTENTS

<b>ABSTRACT</b> .....	<b>iii</b>
<b>ACKNOWLEDGMENTS</b> .....	<b>ix</b>
<b>CHAPTERS</b>	
<b>1. INTRODUCTION</b> .....	<b>1</b>
1.1 Statistical Shape Analysis .....	1
1.1.1 Morphometrics .....	1
1.1.2 Computationally Derived Methods .....	4
1.2 Motivation and Research Contributions .....	8
1.2.1 Shape Regression .....	9
1.2.2 Longitudinal Analysis .....	9
1.2.3 Nonregular Shapes .....	10
1.2.4 Applications to Orthopedics .....	11
1.3 Software .....	12
1.4 Document Organization .....	12
1.5 References .....	14
<b>2. TECHNICAL BACKGROUND</b> .....	<b>20</b>
2.1 Particle Based Modeling (PBM) Framework .....	20
2.1.1 Surface Representation and Correspondences .....	21
2.1.2 Surface Entropy .....	23
2.1.3 Ensemble Entropy .....	24
2.1.4 Cost Function .....	25
2.1.5 ShapeWorks Pipeline .....	26
2.2 Fast Iterative Method (FIM) .....	26
2.2.1 Solution of Eikonal Equation .....	26
2.2.2 Local Solver .....	27
2.2.3 Algorithm for CPU .....	29
2.3 References .....	31
<b>3. PARTICLE BASED SHAPE REGRESSION OF OPEN SURFACES WITH APPLICATIONS TO DEVELOPMENTAL NEUROIMAGING</b> .....	<b>32</b>
3.1 Introduction .....	33
3.2 Methodology .....	34
3.2.1 Correspondence Optimization .....	34
3.2.2 Correspondence with Regression Against Explanatory Variables .....	35
3.2.3 Correspondences on Open Surfaces .....	36
3.2.4 Permutation Test of Significance .....	36
3.3 Results and Discussion .....	37
3.3.1 Synthetic Data (Tori) .....	38

3.3.2	Head Shape Regression .....	38
3.4	Conclusion .....	39
3.5	References .....	40
<b>4.</b>	<b>MIXED-EFFECTS SHAPE MODELS FOR ESTIMATING LONGITUDINAL CHANGES IN ANATOMY .....</b>	<b>41</b>
4.1	Introduction .....	42
4.2	Background .....	43
4.2.1	Correspondence Optimization .....	43
4.2.2	The Laird and Ware Linear Mixed-Effects Model .....	44
4.3	Methodology .....	45
4.3.1	Correspondence with Linear Mixed-Effects Modeling of Shapes .....	46
4.3.2	Estimation of Parameters .....	46
4.3.3	Permutation Test for Significance of Random-Effects .....	47
4.3.4	Permutation Test for Group Discrimination .....	48
4.4	Results and Discussion .....	49
4.4.1	Synthetic Tori .....	49
4.4.2	Mixed-Effects Model for Brain Structures .....	50
4.5	Conclusion and Future Work .....	52
4.6	References .....	53
<b>5.</b>	<b>GEOMETRIC CORRESPONDENCE FOR ENSEMBLES OF NONREGULAR SHAPES .....</b>	<b>54</b>
5.1	Introduction .....	55
5.2	Background .....	56
5.2.1	Correspondence Optimization .....	57
5.2.2	Fast Geodesic Distance Computation .....	57
5.3	Methodology .....	58
5.3.1	Particle Position Optimization using Geodesic Distances .....	58
5.3.2	Correspondence Optimization with Surface Normals .....	59
5.4	Results and Discussion .....	60
5.4.1	Synthetic Data .....	60
5.4.2	Application to Group Comparison .....	60
5.5	Conclusion and Future Work .....	62
5.6	References .....	62
<b>6.</b>	<b>GEODESIC DISTANCES TO LANDMARKS FOR DENSE CORRESPONDENCE ON ENSEMBLES OF COMPLEX SHAPES ..</b>	<b>63</b>
6.1	Introduction .....	64
6.2	Technical Background .....	65
6.2.1	Correspondence Optimization .....	66
6.2.2	Fast Geodesic Distance Computation .....	66
6.3	Methodology .....	66
6.3.1	Proof-of-Concept Experiment .....	67
6.4	Results and Discussion .....	68
6.4.1	Validation on Cortical Surfaces .....	68
6.4.2	Application to AF .....	70
6.5	References .....	71

<b>7. APPLICATIONS</b>	<b>72</b>
7.1 Applications to Orthopedics	72
7.1.1 Cam Type Femoroacetabular Impingement (CAM-FAI)	72
7.1.2 Mouse Model of Multiple Osteochondroma (MO)	77
7.2 Applications in Cardiology	85
7.2.1 Ischemia	85
7.2.2 Atrial Fibrillation	87
7.3 Preliminary Studies	90
7.3.1 Huntington’s Disease	90
7.3.2 Acetabular Cartilage in FAI	91
7.4 References	94
<b>8. SUMMARY</b>	<b>98</b>
8.1 Research Contributions	98
8.2 Practical Considerations and Shortcomings	98
8.2.1 Preprocessing	99
8.2.2 Initialization	99
8.2.3 Optimization	100
8.3 Challenges and Future Work	101
8.3.1 Outlier Shapes	101
8.3.2 Missing Features	102
8.3.3 Growth Models	102
8.4 References	104

## ACKNOWLEDGMENTS

*“The more you are in this business, the more humbled by it you become.”*

*- Meryl Streep*

Meryl Streep may have said this about showbiz, but this quote rings true for me at the end of my tenure at the Scientific Computing and Imaging (SCI) institute.

First and foremost, a humble “Thank you” to my advisor, Ross Whitaker. Working with him, learning from him, was not only an educational but also a fun experience!

Sincere thanks to Guido Gerig, P. Thomas Fletcher, Martin Styner, and Suresh Venkatasubramanian for serving on my committee and for their valuable feedback and discussions. Also, many thanks to everyone at the SCI institute for cultivating an excellent research environment.

Last, and most definitely not the least, thanks to my family and friends for their unconditional, ubiquitous support from *PhDo?* to *PhDone!*

# CHAPTER 1

## INTRODUCTION

Statistical shape analysis is an important research tool in many fields such as medicine and biology. In general, researchers wish to characterize shape variability and compute statistics to test clinically relevant hypotheses. The focus of this work is the development of a general and robust system for shape modeling and analysis that researchers can easily use for multiple applications. This chapter lists the contributions of this dissertation and motivates them in the context of the current shape analysis research.

### 1.1 Statistical Shape Analysis

Shape analysis involves automatic computation of models from populations of shapes, and the associated statistical testing framework. In biomedical applications, researchers use this framework to characterize variability within shape populations and quantify differences between them. Each research problem requires unique analyses that statistical shape models provide. In neurological studies, statistical shape analysis has facilitated analysis of developmental processes, such as pediatric neurodevelopment and longitudinal studies of disease progression [1–3]. The study of how abnormalities in different structures of the brain influence the connections between them is also of importance in studies of disorders like autism [4]. In the orthopedics community, statistical shape analysis has been popular to study bone shapes in presence of pathology and for comparing normative and pathological populations, especially the knee and pelvic joints [5, 6]. Shape models have also been used for surface reconstruction for femur and pelvis shapes from sparse images [7, 8]. In a review, Klingenberg [9] notes that shape analysis has also been used extensively in studies of anthropology, paleontology, and evolution theory, apart from biomedical applications. Many of these studies use traditional morphometric techniques, relying on global measures such as length, angles, and areas [9].

#### 1.1.1 Morphometrics

Morphometrics is the study of shape variation and its covariation with other variables [10, 11]. It represents a confluence of quantitative descriptions of morphological shape

with statistical analyses describing patterns of variation within and among groups [12].

### 1.1.1.1 Traditional Morphometrics

Early methods, also called traditional morphometrics [13] or multivariate morphometrics [14], apply statistical analysis and tools like the correlation coefficient [15], analysis of variance (ANOVA) [16], and principal component analysis (PCA) [17, 18] to collections of morphological measurements. The most popular measurements in traditional morphometry are linear distances, though angles, areas, and ratios [19] have also been used. An example from ornithology is shown in Fig. 1.1, where traditional measurements are useful indicators of growth.

However, many studies have also investigated allometry, trying to separate overall size of a structure and its shape [20–22]. Since linear distance is usually highly correlated with size, a considerable effort has been put into extracting *size-free* measurements and using them to elucidate shape variation [23, 24]. Different size correction methods yield

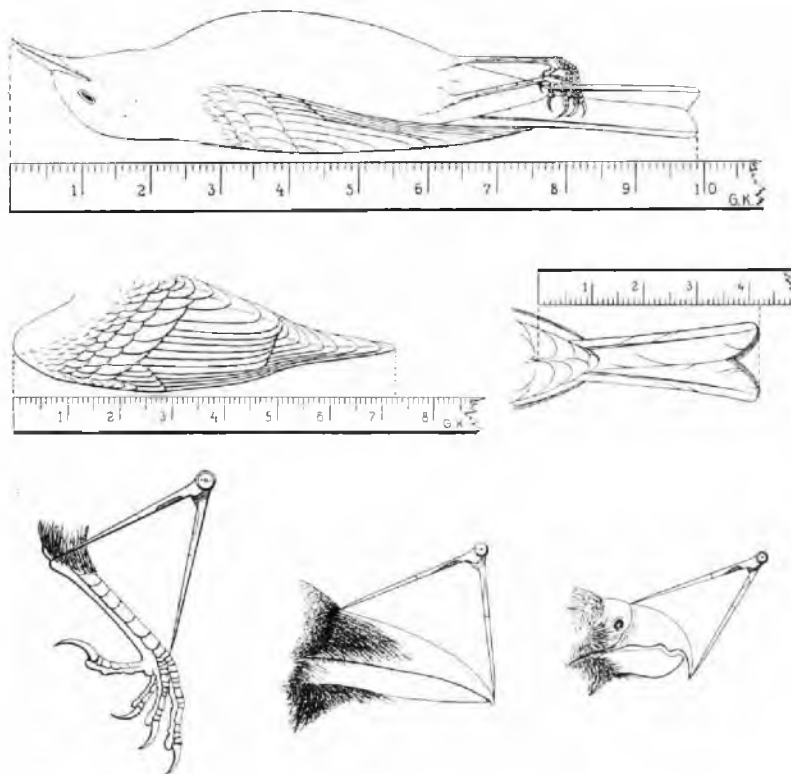


**Figure 1.1.** Standard measurements of birds.

Reprinted with permission from Wikimedia Commons.

Available at: <https://commons.wikimedia.org/wiki/File:BirdMorphometrics.jpg>.

different results, and this presents a problem since the separation of size from shape is an important consideration for allometric studies. Homology of commonly used distance measures (e.g., maximal width) is also difficult to assess, as not all distances are measured between homologous points. These measures do not lend themselves easily for interpretation or visualization of shape variability [12, 25]. Thus, while traditional morphometrics possess a nice combination of multivariate statistics and quantitative morphological measurements, they have limited statistical power.

### 1.1.1.2 Geometric Morphometrics

A series of advances exploring alternate methods of quantifying and analyzing morphology, with particular interest in capturing the geometry of morphological shape, began to address the difficulties of traditional morphometrics. This was the *geometric morphometric revolution* described by Rohlf and Marcus [26]. Methods in geometric morphometrics employ a shape representation based on homologous landmarks, which is mathematically more systematic as compared to traditional methods and is also invariant to size. Landmarks are explicitly defined coordinates of homologous points in two or three dimensions. They lie on the surface and are picked by an expert with domain knowledge. For example, Fig. 1.2(a) shows an example from an anthropology study where anatomically significant landmarks have been picked on a cichlid fish [12]. Landmarks represent the underlying geometry better than traditional morphometrics measurements, which do not provide much information about shape homologies and may be corrupted by intra- and interobserver errors.

The most widely used framework for landmark-based shape analysis was proposed by David Kendall, who formulated a rigorous mathematical definition of shape based on homologous landmarks, invariant to size and orientation [27–29]. In parallel, researchers developed the mathematical tools required to align and normalize landmark data with



**Figure 1.2.** An example of geometric morphometry and its limitations: (a) Landmarks recorded on body of cichlid fish, (b) Landmarks of 412 specimens before and after GPA  
 Reprinted with permission from Taylor & Francis, D. Adams, F. J. Rohlf, and D. Slice, Geometric morphometrics: Ten years of progress following the “revolution, *Ital. J. Zool.*, vol. 71, no. 1, pp. 516, 2004.

respect to size and orientation. Most notable among these methods were Bookstein’s two-point registration and thin plate spline (TPS) warping method [25, 30] and the generalized procrustes analysis (GPA) method pioneered by Goodall [31–33]. GPA removes variation in location, orientation, and size and aligns shapes in an arbitrary (yet common) coordinate system. This alignment results in points that can be projected into the tangent space of Kendall’s shape space [28]. Conventional statistical analyses can be carried out in the linear tangent space [11, 12]. Results of these statistical analyses can be visualized directly in terms of the landmark configurations since the geometry of shapes is preserved throughout the analysis. Shape differences can be visualized by interpolating the coordinate transformations that warp one landmark configuration to another, analogous to D’Arcy Thompson’s transformation grids, which were interpolated using TPS [34].

While the landmark-based methods described above work well for small samples and simple shapes, they are limited by the need for manual landmarking. Manual landmarks are prone to observer error and difficult to reproduce. They may also miss subtle variations and fail to provide a complete analysis of shape variability. Fig. 1.2(b) shows landmarks from 412 cichlid specimens before and after alignment using GPA. While geometric morphometrics captures the overall shape variability, it is difficult to capture details of the cichlid shape with a just a few manually placed landmarks. Advances in three dimensional imaging modalities like magnetic resonance imaging and computed tomography has led to increased use of computationally derived models, which have distinct advantages over manual landmarking methods.

### 1.1.2 Computationally Derived Methods

Computationally derived models provide a much more detailed representation of shape geometry and are able to capture more subtle shape variations. Visualization of shape variability and statistical results are also improved since a more detailed representation of the geometry is created and preserved during the analysis process. Computationally derived methods are unsupervised, making them faster and more efficient. These methods are also less susceptible to observer error and bias, and thus results are easy to reproduce. With the advent of noninvasive imaging, computationally derived shape models are an important tool for the study of anatomy in the presence of pathology and longitudinal studies of development and disease progression. Two categories of computationally driven shape models are popularly used. The first group, registration-based methods, considers shape to be embedded in image intensity values and uses nonlinear alignment to map these images to a template image or atlas. The second group, with which this dissertation

is concerned, builds upon geometric morphometrics to sample shapes systematically and obtain an arbitrarily dense set of correspondences for statistical analysis. The models in this category are known as point distribution models [35], point-based models [36], or simply, correspondence models.

### 1.1.2.1 Registration-Based Methods

Registration-based methods nonlinearly align image volumes to a template and consider the population variability to be captured by the registration parameters. An early example of shape modeling using registration-based methods is the work of Bajcsy, which applied TPS methods to model brain structures [37]. Wright and Ashburner introduced a more general framework based on registration for the study of brain structures. This framework includes *voxel-based morphometry* and *deformation-based morphometry*, which capture anatomical differences at the mesoscopic scale and can also be used to capture global anatomical differences via deformations [38, 39]. Several other researchers have also contributed to shape modeling based on voxel and tensor-based methods, which are reviewed by Ashburner in [40]. These methods align a population of images to a template and then use distributions of transformed intensity values, transformed tensor values, or the transformations themselves over a localized region to compute statistics. Diffeomorphic registration forms another class of registration-based shape analysis methods. Miller et al. first proposed diffeomorphic image registration using geodesic fluid flow models and linear statistics in the space of initial momenta [41–43]. These methods have been used to study the brain structure [42] and have also been applied for analysis of cardiac pathology [44]. Davis and Joshi note that diffeomorphic flows are invertible and further develop the approach by estimating an unbiased anatomical atlas for regression analysis [45, 46].

### 1.1.2.2 Correspondence Methods

Correspondence methods are automated extensions of landmark-based methods and work by randomly sampling shapes in a sufficiently dense manner, capturing detailed geometric variability in the shapes. Landmark models have two main working assumptions. The first assumption is that the chosen homologous points represent anatomically significant positions on the shape and are linked by some biological process [11]. The second is that landmarks capture all variability in the underlying shapes relevant to the biological problem being solved. These assumptions require landmark-based methods to be supervised and carefully formulated by domain experts. Correspondence methods avoid both these a priori assumptions and attempt to learn the variability present in the underlying shapes. Statis-

tical analysis for correspondence models can then be performed using the same techniques and approximations used for earlier landmark-based methods.

The problem of automatically finding correspondence points across all shapes is ill-posed since potentially an infinite number of possible sets of correspondences can be picked for any given shape population. Regularization via geometric constraints is usually applied to ensure a faithful representation of the underlying geometries. Several researchers have proposed methods that use purely geometric regularization, considering only one shape at a time. This type of regularization works by constructing a set of shape parameterizations then sampling surface point locations in a consistent fashion to choose correspondences. An early example of purely geometric regularization is the use of Fourier descriptors used to parameterize two-dimensional contours [47, 48]. Nain et al [49] have proposed similar approaches based on spherical wavelets. Medial representations of shape have also been used to construct nonlinear shape models for neurobiological studies [1, 50]. Another method that constructs nonlinear models is the sliding landmark method, which builds correspondences via minimization of the bending energy of a TPS transformation between correspondences on individual shapes and an atlas [51, 52].

One of the most popular approaches using purely geometric regularization is based on spherical harmonic descriptions of shape segmentations (SPHARM), by Brechbühler et al. [1, 53]. The SPHARM description is computed from surface meshes using an area preserving, distortion minimizing spherical parameterization. Correspondences are then established by aligning the first order ellipsoid from the SPHARM coefficients. An icosahedron subdivision scheme is used to create triangulated surfaces (SPHARM-PDM), which are then aligned using GPA for statistical analysis. Thus, this method generates a parameterization of each sample shape individually, without any knowledge of other shapes in the population. This poses a significant problem for populations with a large variability in the shapes. For example, consider the box-bump dataset described in [54] and displayed in Fig. 1.3(top), where a bump is randomly placed on a rectangular contour of constant dimensions. Since SPHARM-PDM models each shape individually, the method does not recognize the fact that the bump is a single feature with varying position. This happens because the focus is on area preservation and minimum distortion during SPHARM-PDM creation, and shape similarity is not optimized in a systematic manner, resulting in an incorrect model, as shown in Fig. 1.3(bottom). Styner et al. [55] also reiterate this limitation in a recent review of correspondence methods for local shape analysis. A combination of purely geometric regularization with a consideration of population statistics like total variation or information

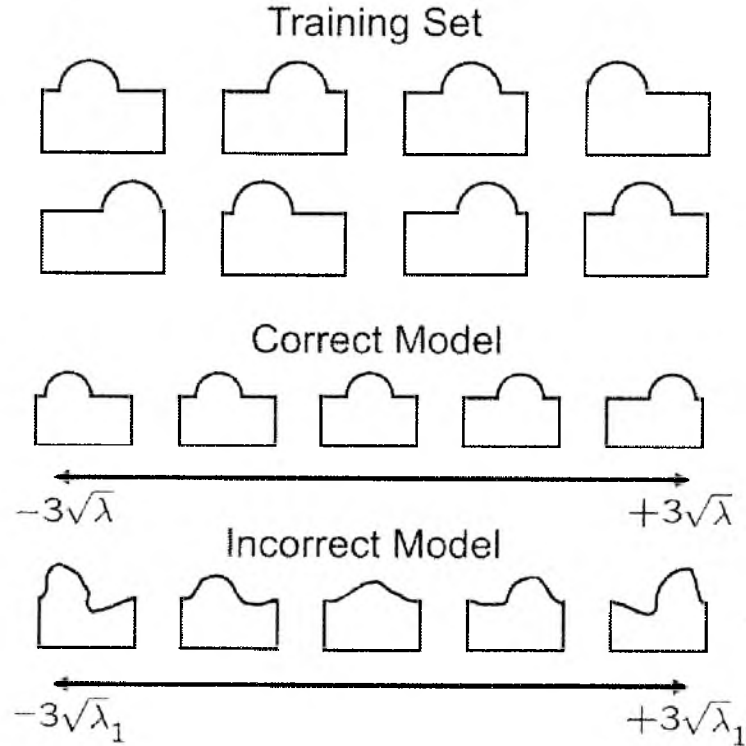


**Figure 1.3.** Top: A training set of synthetic box bump shapes. Middle: The model built using the correct correspondence, which has just one mode of variation. Bottom: The first mode of a model built using an incorrect correspondence. For both models, examples generated by varying the first mode within the range  $\pm 3\sqrt{\lambda_1}$  are shown.

Statistical models of shape - optimisation and evaluation, Objective functions, 2008, 70, R. H. Davies, C. J. Twining, and C. J. Taylor, With permission from Springer.

content can be used to avoid this problem and obtain a model similar to Fig. 1.3(middle).

The idea of automatically placing correspondences by minimizing information content across shape populations was first proposed by Kotcheff and Taylor [56]. Their objective function is the determinant of the covariance matrix, which is optimized via a genetic algorithm to obtain improved correspondences. It should be noted that this is similar to minimizing the total variance of the model. Davies et al. [57] propose a similar objective function based on the minimum description length (MDL) to obtain a piecewise linear reparameterization using a hierarchical minimization scheme. This approach works on the assumption that the best description of the population is given by the simplest possible description, one that encodes the data and model parameters using the shortest length. Thus, the MDL model is optimized to find the minimal cost of transmitting model parameters based on the correspondences. An extension of the MDL method to three dimensions

is given in [58]. This extension requires a spherical parameterization as an input and creates octahedral subdivisions to establish correspondences. These correspondences are manipulated in the optimization iterations by using Cauchy kernels for smoothed updates. An important problem is how to ensure that the resulting correspondences still represent valid shapes from the original population. Many methods have been proposed to regularize the MDL formulation and avoid this problem, but they introduce additional parameters and make the optimization more complex. Several extensions have been proposed [59, 60], but MDL continues to be prohibitive for surfaces, which do not exhibit a spherical topology. In spite of these difficulties, MDL models are effective for a large class of shapes and result in improved correspondences when compared to methods using purely geometric regularization, as shown in [55]. This work also notes that MDL performance is virtually the same as that of minimizing sample covariance or  $\min \log |\Sigma + \alpha I|$  [61].

Cates et al. explore this property further in the particle-based modeling (PBM) framework [36], in which shapes are modeled as nonparametric, dynamic particle systems that do not rely on a specific topology. Particle positions are directly optimized, without the need for intermediate parameterization, and an extension to open surfaces is also implemented [62]. This framework explicitly constructs valid shape representations during optimization by optimizing an entropy measure on their distributions. The PBM framework is compared to the MDL method using a set of box bump shapes similar to the one described earlier. The result of this experiment, which used 24 shapes and is described in [36] shows that the first mode of variation for the PBM framework remains faithful to the original population when varied within the range of  $\pm 3$  standard deviations to produce shapes similar to Fig. 1.3 (middle). Further mathematical details of the PBM framework are provided in Chapter 2. This dissertation extends and builds upon the PBM framework by adding new criteria for correspondence optimization, thus making the framework applicable to a broader class of shapes.

## 1.2 Motivation and Research Contributions

Shape analysis methods reviewed in the previous section have been successfully used in many biomedical applications. However, further improvements are required to make these techniques more readily available to biologists and clinicians working with a broader class of problems. This dissertation aims to build a robust shape analysis framework that biologists can easily apply to analyze populations of increasingly complex shapes. The framework also needs to be flexible to let clinicians leverage growing amounts of longitudinal

data to study shape trends of normative development and compare them with trends of disease progression. To achieve this, this work builds upon the PBM framework by adding new correspondence optimization methods and also provides statistical methods relevant to specific biological problems. This section further motivates and describes the research contributions of this work.

### 1.2.1 Shape Regression

Shape regression is an essential technology to relate anatomical changes with an underlying biological parameter, such as age. One clinical example is the study of brain development during childhood and adolescence. While there is a rich selection of studies that describe growth patterns based on volumetric measurements, there has been very little work on modeling early head and brain growth over time. Such a study of the influence of development on shape, via shape regression, can result in aggregate models of growth with variability and be of great use in developmental analyses for pediatric neurodevelopment. Shape regression not only provides basic insights into the evolution of shape as driven by the underlying biological parameter, but also has the potential to allow comparison of individual trends against normative models. The biggest bottleneck in obtaining such models is the difficulty in precise characterization of shape variability due to underlying model parameters and a systematic, unbiased way to test for correlations in the high dimensional setting of imaging applications.

The first contribution of this work, presented in Chapter 3, is a method to include shape regression within the PBM framework and also provide a method to test model significance via a specifically designed nonparametric permutation test. This work was done with Dr. Joshua Cates at the Scientific Computing and Imaging (SCI) Institute, University of Utah.

### 1.2.2 Longitudinal Analysis

Longitudinal studies provide a rich picture of anatomical changes occurring during normative development or disease progression by collecting imaging data at multiple time points for each individual. Linear mixed-effects (LME) models [63] are a popular choice for longitudinal analysis of univariate data. However, these models find little to no application in the high dimensional setting of most biomedical applications where the biggest bottleneck is the estimation of a large number of model parameters. The recent use of mixed-effects models on a small number of manually selected landmarks [64] to model facial shape development is encouraging and can be adapted to obtain dense correspondences.

The second contribution of this work, presented in Chapter 4, is an LME model for

shapes. The parameters of the model are estimated in a hierarchical fashion within the PBM framework. The estimation process is interleaved with the correspondence optimization step to yield correspondences based on the LME model. The significance of the model is tested using a specifically designed permutation test. This work was done with Abhishek Singh at the SCI Institute, University of Utah. Further, this extension is applied to test for differences between low and high-risk groups in an autism study. This work was done with Prasanna Muralidharan at the SCI Institute, University of Utah.

### 1.2.3 Nonregular Shapes

Medical or biological shapes are typically derived from the interfaces between organs or tissue types and present a significant challenge in the form of sharp features or regions with high curvature. Around such features, particle interactions in ambient space, coupled with the use of Euclidean distance, may result in incorrect correspondences. More specifically, points in different tangent spaces may interact and violate surface constraints, or seemingly nearby points may interact even though they sample completely different features on the shape. Nonregular shapes also pose a challenge in establishing correspondences *across* shapes. This is due to the fact that most correspondence methods rely solely on point positions. In such cases, the best alternative is to move away from sole reliance on particle position as a feature and consider the direction as well. Oguz et al. [65] propose a generalized entropy framework where *functions* of positions are considered in the correspondence optimization framework, rather than the point positions themselves. However, it must be noted that it is not always convenient to evaluate such *functions* for any given population.

This work extends the PBM framework to include geodesic distances for computing intrashape particle interactions, which results in a more sensitive representation of the underlying shape geometry. Geodesic distances are efficiently computed using the *fast iterative method*, described in detail in Chapter 2, on an intermediate triangle mesh shape representation. A new entropy term based on surface normals is also introduced to improve correspondences near sharp features across shapes. These methods, presented in Chapter 5, are applied to a study to quantify shape differences between cardiac left ventricle walls from controls and patients with ischemia.

Geometric complexity of certain biological shapes (e.g., cortical surface) further exposes problems due to sole reliance on particle position to establish correspondence. In such cases, due to the highly curved nature of the surface, even a strong degree of adaptivity may not produce a dense sampling such that nearby particles can be assumed to lie on the local tangent planes, unless a very high number of particles are used. The use of such high

number of particles incurs a high computational cost and may still allow interaction between geodesically distant particles on highly folded surfaces. Widely used software packages such as FreeSurfer [66] and BrainVoyager [67] use cortex *inflation*—a process of removing cortical folds and then, typically, mapping to a sphere—to overcome the complexity in matching cortical surfaces. Correspondence based on point positions is sensitive not only to geometric complexity, but also to anatomical variability in shapes where a failure to match common features across shapes can lead to inconsistent correspondences. It is also desirable to have isometry invariant correspondences for a robust analysis of populations of highly nonregular shapes. The success of distance-to-landmark type features to achieve an isometry invariant matching between two shapes [68–70] demonstrates that collections of such distances are rich, nearly complete descriptions of shapes and might be useful to obtain dense, isometry-invariant correspondences for shape populations.

The next contribution of this dissertation, presented in Chapter 6, is the use of geodesic distances to landmarks to provide improved, isometry-invariant correspondences on complex shapes like the human cerebral cortex.

#### 1.2.4 Applications to Orthopedics

Statistical shape models have long been popular in the orthopedics community to study bone shapes in presence of pathology and for comparison of populations, especially the knee and pelvic joints [5, 6]. Shape models have also been used for surface reconstruction for femur and pelvis shapes from sparse images [7, 8]. Nonparametric correspondence methods, like the ones presented in this dissertation, allow comparison of complex 3D morphology without any assumptions about the ideal geometry associated with the bone under study. In cooperation with clinical collaborators, this dissertation attempts to validate the methods and apply them to explore specific clinical questions in the field of orthopedics, as described in Chapter 7.

Cam femoroacetabular impingement (CAM-FAI) is characterized by a malformed femoral head that may cause shearing between the femur and acetabulum, leading to joint damage and early hip osteoarthritis. Two-dimensional radiographic measurements are commonly used to diagnose FAI, but provide only a planar view of the femoral head and often assume the ideal femur shape to be spherical. Furthermore, most radiographic measures do not provide quantitative information that translates well for preoperative planning (i.e., they cannot specify the location and extent of a lesion, nor the amount of bone that should be debrided). The shape analysis methods from this dissertation can be used to objectively compare complex femur morphology without the need to assume ideal geometry.

The first application describes a study to quantify 3D variation and morphological differences between control and CAM type femurs. This work was done in collaboration with Dr. Andrew Anderson and Dr. Michael Harris from the Department of orthopedics, University of Utah.

Multiple osteochondromas (MO) is a heritable disorder of connective tissue characterized by multiple lesions on the metaphyses of long bones. Individuals with MO variably demonstrate reduced linear growth of the long bones, which lead to dramatic deformities and pose one of the many clinical challenges in the treatment/surgical planning process. One hypothesis relates to a possible steal phenomenon, where the peripheral spread of the cancer steals the longitudinal growth potential of the affected bone.

The second application uses shape correspondences to study MO in mouse models. This work was done in collaboration with Dr. Kevin Jones from the Huntsman Cancer Institute, University of Utah School of Medicine.

### 1.3 Software

The ShapeWorks software [71] implements the PBM pipeline as a collection of command line executables. The core library manages particle system representations of shapes and implements the original entropy-based correspondence optimization method [36]. There are additional libraries constructed using the Insight toolkit (ITK) [72] for numerical optimizations and a graphical user interface for visualization of results, built using the Visualization toolkit (VTK) [73] and QT [74]. The work in this dissertation includes extensions to the ShapeWorks core library to improve correspondences for highly nonregular shapes and incorporates simple linear regression and linear mixed effects shape models to study shape change over time. These methods are incorporated as templated C++ classes and are invoked via specific settings in the ShapeWorks parameter file. The updated ShapeWorks software is freely available on the SCI Institute software page [71]. Additional tools are also made available for geodesic distance computation, landmark annotation, and computing distance to landmark features. Statistical analysis and permutation tests are implemented in the R environment [75].

### 1.4 Document Organization

This dissertation is presented as a hybrid collection of reprints of published papers and observations from collaborative clinical projects. The chapters are organized as follows:

Chapter 2 provides technical background for the PBM framework and gives details of an efficient method used to compute geodesic distances.

Chapter 3 extends the PBM framework to include linear shape regression and develops methodology for testing model significance.

Chapter 4 describes the addition of the linear mixed-effects shape model into the PBM framework for longitudinal analysis.

Chapters 5 and 6 describe the general methodology and implementation to improve geometric correspondences for populations of nonregular surfaces via the substitution of Euclidean distance measures with their geodesic counterparts (first contribution in Chapter 5), the use of an entropy term based on surface normals (second contribution in Chapter 5) and the extension of correspondence optimization beyond ‘particle position’ via distance features from anatomically significant landmarks (Chapter 6).

Chapter 7 describes work with clinical collaborators to apply and validate the particle correspondence framework while addressing specific biomedical problems.

Chapter 8 provides a summary of the research contributions of this dissertation and also lists some limitations and directions for future work.

## 1.5 References

- [1] M. Styner, J. A. Lieberman, D. Pantazis, and G. Gerig, “Boundary and medial shape analysis of the hippocampus in schizophrenia,” *Med. Image. Anal.*, vol. 8, no. 3, pp. 197–203, Sep 2004.
- [2] S. Pizer, J.-Y. Jeong, C. Lu, K. Muller, and S. Joshi, “Estimating the statistics of multi-object anatomic geometry using inter-object relationships,” in *Deep structure, singularities, and computer vision*. Springer Berlin Heidelberg, 2005, pp. 60–71.
- [3] M. Styner, I. Oguz, S. Xu, C. Brechbuhler, D. Pantazis, J. J. Levitt, M. E. Shenton, and G. Gerig, “Framework for the Statistical Shape Analysis of Brain Structures using SPHARM-PDM,” *Insight J.*, no. 1071, pp. 242–250, 2006.
- [4] R. P. Hobson, “Handbook of autism and pervasive developmental disorders,” *Applied Cognitive Psychology*, vol. 2, no. 4, pp. 293–293, 1988.
- [5] T. L. Bredbenner, T. D. Eliason, R. S. Potter, R. L. Mason, L. M. Havill, and D. P. Nicolella, “Statistical shape modeling describes variation in tibia and femur surface geometry between control and incidence groups from the osteoarthritis initiative database,” *J. Biomech.*, vol. 43, no. 9, pp. 1780 – 1786, 2010.
- [6] C. K. Fitzpatrick, M. A. Baldwin, P. J. Laz, D. P. FitzPatrick, A. L. Lerner, and P. J. Rullkoetter, “Development of a statistical shape model of the patellofemoral joint for investigating relationships between shape and function,” *J. Biomech.*, vol. 44, no. 13, pp. 2446 – 2452, 2011.
- [7] S. Meller and W. A. Kalender, “Building a statistical shape model of the pelvis,” *Int. Congr. Ser.*, vol. 1268, no. 0, pp. 561 – 566, 2004.
- [8] G. Zheng, X. Dong, K. T. Rajamani, X. Zhang, M. Styner, R. U. Thoranaghatte, L.-P. Nolte, and M. Á. G. Ballester, “Accurate and robust reconstruction of a surface model of the proximal femur from sparse-point data and a dense-point distribution model for surgical navigation,” *IEEE Trans. Bio-Med. Eng.*, vol. 54, no. 12, pp. 2109–2122, 2007.
- [9] C. P. Klingenberg, “Morphometrics and the role of the phenotype in studies of the evolution of developmental mechanisms,” *Gene*, vol. 287, no. 1-2, pp. 3–10, apr 2002.
- [10] F. L. Bookstein, *Morphometric tools for landmark data: geometry and biology*. Cambridge University Press, Jun. 1997.
- [11] I. Dryden and K. Mardia, *Statistical shape analysis*. Wiley, 1998.
- [12] D. Adams, F. J. Rohlf, and D. Slice, “Geometric morphometrics: ten years of progress following the ‘revolution’,” *Ital. J. Zool.*, vol. 71, no. 1, pp. 5–16, 2004.
- [13] L. Marcus, “Traditional morphometrics,” in *Proc. Michigan Morphometrics Workshop*, vol. 2, 1990, pp. 77–122.
- [14] R. A. Reyment, “Multivariate morphometrics and analysis of shape,” *Math. Geosci.*, vol. 17, no. 6, pp. 591–609, 1985.

- [15] K. Pearson, "Note on regression and inheritance in the case of two parents," *Proc. R. Soc. Lond.*, vol. 58, no. 1, pp. 240–242, 1895.
- [16] R. A. Fisher, "The logic of inductive inference," *J. R. Stat. Soc. Ser. A. Stat. Soc.*, vol. 98, pp. 35–54, 1935.
- [17] K. Pearson, "On lines and planes of closest fit to systems of points in space," *Philos. Mag.*, vol. 2, no. 6, pp. 559–572, 1901.
- [18] H. Hotelling, "Analysis of a complex of statistical variables into principal components," *J. Educ. Psych.*, vol. 24, 1933.
- [19] H. Baur and C. Leuenberger, "Analysis of ratios in multivariate morphometry," *Syst. Biol.*, vol. 60, no. 6, pp. 813–825, Dec 2011.
- [20] J. Huxley, "Terminology of relative growth," *Nature*, vol. 137, pp. 780–781, May 1936.
- [21] P. Jolicoeur, "The multivariate generalization of the allometry equation," *Biometrics*, vol. 19, no. 3, pp. 497–499, Sep. 1963.
- [22] J. Gayon, "History of the concept of allometry," *Am. Zool.*, vol. 40, no. 5, pp. 748–758, Nov. 2000.
- [23] K. M. Somers, "Multivariate allometry and removal of size with principal components analysis," *Syst. Biol.*, vol. 35, no. 3, pp. 359–368, Sep. 1986.
- [24] W. L. Jungers, A. B. Falsetti, and C. E. Wall, "Shape, relative size, and size-adjustments in morphometrics," *Am. J. Phys. Anthropol.*, vol. 38, no. 2, pp. 137–161, 1995.
- [25] F. L. Bookstein, "Biometrics, biomathematics and the morphometric synthesis," *Bull. Math. Biol.*, vol. 58, no. 2, pp. 313–365, Mar. 1996.
- [26] F. James Rohlf and L. F. Marcus, "A revolution morphometrics," *Trends Ecol. Evol.*, vol. 8, no. 4, pp. 129–132, Apr. 1993.
- [27] D. G. Kendall, "The diffusion of shape," *Adv. Appl. Probab.*, vol. 9, no. 3, pp. 428–430, Sep. 1977.
- [28] ———, "Shape manifolds, procrustean metrics, and complex projective spaces," *Bull. London Math. Soc.*, vol. 16, no. 2, pp. 81–121, 1984.
- [29] D. Kendall, D. Barden, T. Carne, and H. Le, *Shape and Shape Theory*, 2009.
- [30] F. L. Bookstein, "Principal warps: thin-plate splines and the decomposition of deformations," *IEEE Trans. Pattern Anal. Mach. Intell.*, vol. 11, no. 6, pp. 567–585, 1989.
- [31] J. R. Hurley and R. B. Cattell, "The procrustes program: producing direct rotation to test a hypothesized factor structure," *Behav. Sci.*, vol. 7, no. 2, pp. 258–262, Apr. 1962.

- [32] C. Goodall, "Procrustes methods in the statistical analysis of shape." *J. R. Stat. Soc. Series. B. Stat. Methodol.*, vol. 53, pp. 285–339, 1991.
- [33] J. T. Kent, "The complex Bingham distribution and shape analysis," *J. R. Stat. Soc. Series. B. Stat. Methodol.*, vol. 56, no. 2, pp. 285–299, 1994.
- [34] D. W. Thompson, *On growth and form*. Cambridge University Press, 1942.
- [35] T. F. Cootes, C. J. Taylor, D. H. Cooper, and J. Graham, "Active shape models - their training and application," *CVIU*, vol. 61, no. 1, pp. 38–59, 1995.
- [36] J. Cates, P. T. Fletcher, M. Styner, M. Shenton, and R. Whitaker, "Shape modeling and analysis with entropy-based particle systems," in *Proc. IPMI*, 2007, pp. 333–345.
- [37] R. Bajcsy and S. Kovačič, "Multiresolution elastic matching," *Comput. Vision Graph. Image Process.*, vol. 46, no. 1, pp. 1–21, Apr. 1989.
- [38] I. C. Wright, P. K. McGuire, J. B. Poline, J. M. Travere, R. M. Murray, C. D. Frith, R. S. Frackowiak, and K. J. Friston, "A voxel-based method for the statistical analysis of gray and white matter density applied to schizophrenia," *Neuroimage*, vol. 2, no. 4, pp. 244–252, Dec 1995.
- [39] J. Ashburner, C. Hutton, R. Frackowiak, I. Johnsrude, C. Price, and K. Friston, "Identifying global anatomical differences: deformation-based morphometry," *Hum. Brain Mapp.*, vol. 6, no. 5-6, pp. 348–357, 1998.
- [40] J. Ashburner and K. J. Friston, "Voxel-based morphometry - the methods," *Neuroimage*, vol. 11, pp. 805–821, 2000.
- [41] M. Vaillant, M. Miller, L. Younes, and C. Ceritoglu, "Initial value diffeomorphic landmark matching and its application shape statistics," in *Proc. IEEE SSP*, 2003, pp. 306–.
- [42] M. Vaillant, M. I. Miller, L. Younes, and A. Trouve, "Statistics on diffeomorphisms via tangent space representations," *Neuroimage*, vol. 23 Suppl 1, pp. S161–169, 2004.
- [43] M. F. Beg, M. I. Miller, A. Trouvé, and L. Younes, "Computing large deformation metric mappings via geodesic flows of diffeomorphisms," *Int. J. Comput. Vision*, vol. 61, no. 2, pp. 139–157, Feb. 2005.
- [44] P. A. Helm, L. Younes, M. F. Beg, D. B. Ennis, C. Leclercq, O. P. Faris, E. McVeigh, D. Kass, M. I. Miller, and R. L. Winslow, "Evidence of structural remodeling in the dyssynchronous failing heart," *Circ. Res.*, vol. 98, no. 1, pp. 125–132, Jan 2006.
- [45] B. C. Davis, P. T. Fletcher, E. Bullitt, and S. Joshi, "Population shape regression from random design data," *Int. J. Comput. Vision*, vol. 90, no. 2, pp. 255–266, Nov. 2010.
- [46] S. Joshi, B. Davis, B. M. Jomier, and G. G. B, "Unbiased diffeomorphic atlas construction for computational anatomy," *Neuroimage*, vol. 23, pp. 151–160, 2004.

- [47] E. Persoon and K.-S. Fu, "Shape discrimination using fourier descriptors," *IEEE Trans. Syst., Man, Cybern.*, vol. 7, no. 3, pp. 170–179, 1977.
- [48] F. P. Kuhl and C. R. Giardina, "Elliptic fourier features of a closed contour," *CGIP*, vol. 18, no. 3, pp. 236 – 258, Mar. 1982.
- [49] D. Nain, M. Styner, M. Niethammer, J. J. Levitt, M. E. Shenton, G. Gerig, A. Bobick, and A. Tannenbaum, "Statistical shape analysis of brain structures using spherical wavelets," *Proc. ISBI*, vol. 4, pp. 209–212, Apr. 2007.
- [50] K. Gorczowski, M. Styner, J.-Y. Jeong, J. Marron, J. Piven, H. Hazlett, S. Pizer, and G. Gerig, "Statistical shape analysis of multi-object complexes," in *Proc. CVPR*, Jun. 2007, pp. 1–8.
- [51] P. Dalai, B. Munsell, S. Wang, J. Tang, K. Oliver, H. Ninomiya, X. Zhou, and H. Fujita, "A fast 3D correspondence method for statistical shape modeling," in *Proc. CVPR*, Jun. 2007, pp. 1–8.
- [52] B. C. Munsell, P. Dalal, and S. Wang, "Evaluating shape correspondence for statistical shape analysis: a benchmark study," *IEEE Trans. Pattern Anal. Mach. Intell.*, vol. 30, no. 11, pp. 2023–2039, Nov. 2008.
- [53] C. Brechbühler, G. Gerig, and O. Kübler, "Parametrization of closed surfaces for 3-D shape description," *CVIU*, vol. 61, pp. 154–170, 1995.
- [54] R. H. Davies, C. J. Twining, and C. J. Taylor, *Statistical models of shape - optimisation and evaluation*. Springer, 2008.
- [55] M. Styner, S. Xu, M. El-Sayed, and G. Gerig, "Correspondence evaluation in local shape analysis and structural subdivision," in *Proc. ISBI*, Apr. 2007, pp. 1192–1195.
- [56] A. Kotcheff and C. Taylor, "Automatic construction of eigenshape models by direct optimization," *Med. Image Anal.*, vol. 2, pp. 303–314, 1998.
- [57] R. H. Davies, C. J. Twining, T. F. Cootes, J. C. Waterton, and C. J. Taylor, "A minimum description length approach to statistical shape modeling." *IEEE Trans. Med. Imag.*, vol. 21, no. 5, pp. 525–537, 2002.
- [58] —, "3D statistical shape models using direct optimisation of description length," in *Proc. ECCV*, 2002, pp. 3–20.
- [59] T. Heimann, I. Wolf, T. Williams, and H. peter Meinzer, "3D active shape models using gradient descent optimization of description length," in *in Proc. IPMI*. Springer, 2005, pp. 566–577.
- [60] C. Twining, R. Davies, and C. Taylor, "Non-parametric surface-based regularisation for building statistical shape models," in *Proc. IPMI*, 2007, vol. 4584, pp. 738–750.
- [61] M. Styner, J. Lieberman, and G. Gerig, "Boundary and medial shape analysis of the hippocampus in schizophrenia," in *Proc. MICCAI*, 2003, pp. 464–471.

- [62] M. Datar, J. E. Cates, P. T. Fletcher, S. Gouttard, G. Gerig, and R. T. Whitaker, "Particle based shape regression of open surfaces with applications to developmental neuroimaging," in *Proc. MICCAI (1)*, 2009, pp. 167–174.
- [63] N. Laird and J. H. Ware, "Random-effects models for longitudinal data," *Biometrics*, vol. 38, no. 4, pp. 963–974, 1982.
- [64] S. J. E. Barry and A. W. Bowman, "Linear mixed models for longitudinal shape data with applications to facial modeling," *Biostatistics*, vol. 9, no. 3, pp. 555–565, 2008.
- [65] I. Oguz, J. Cates, P. T. Fletcher, Z. Warnock, R. Whitaker, D. Cool, S. Aylward, and M. Styner, "Cortical correspondence using entropy-based particle systems and local features," in *Proc. ISBI*, 2008, pp. 1637–1640.
- [66] B. Fischl, M. I. Sereno, R. B. H. Tootell, and A. M. Dale, "High-resolution intersubject averaging and a coordinate system for the cortical surface," *Hum. Brain Mapp.*, vol. 8, pp. 272–284, 1999.
- [67] R. Goebel, F. Esposito, and E. Formisano, "Analysis of functional image analysis contest (FIAC) data with brainvoyager QX: from single-subject to cortically aligned group general linear model analysis and self-organizing group independent component analysis," *Hum. Brain Mapp.*, vol. 27, no. 5, pp. 392–401, 2006.
- [68] A. M. Bronstein, M. M. Bronstein, and R. Kimmel, "Generalized multidimensional scaling: a framework for isometry-invariant partial surface matching," *PNAS*, vol. 103, no. 5, pp. 1168–1172, Jan. 2006.
- [69] F. Mémoli and G. Sapiro, "A theoretical and computational framework for isometry invariant recognition of point cloud data," *Found. Comput. Math.*, vol. 5, no. 3, pp. 313–347, Jul. 2005.
- [70] A. M. Bronstein, M. M. Bronstein, R. Kimmel, M. Mahmoudi, and G. Sapiro, "A gromov-hausdorff framework with diffusion geometry for topologically-robust non-rigid shape matching," *Int. J. Comput. Vision*, vol. 89, no. 2-3, pp. 266–286, Sep. 2010.
- [71] J. Cates, M. Datar, P. T. Fletcher, and R. Whitaker, *ShapeWorks: Particle-based Shape Correspondence and Visualization Software*, Scientific Computing and Imaging Institute, University of Utah, Salt Lake City, USA, 2011. [Online]. Available: <http://www.sci.utah.edu/software/shapeworks.html>
- [72] L. Ibanez, W. Schroeder, L. Ng, and J. Cates, *The ITK Software Guide*, Insight Consortium, <http://www.itk.org/ItkSoftwareGuide.pdf>, 2003.
- [73] W. J. Schroeder, L. S. Avila, and W. Hoffman, "Visualizing with VTK: a tutorial," *IEEE Comput. Graph. Appl.*, vol. 20, no. 5, pp. 20–27, Sep. 2000. [Online]. Available: <http://dx.doi.org/10.1109/38.865875>
- [74] J. Blanchette and M. Summerfield, *C++ GUI programming with Qt 4*. Upper Saddle River, NJ, USA: Prentice Hall PTR, 2006.

- [75] Team, R Core, *R: a language and environment for statistical computing*, R Foundation for Statistical Computing, Vienna, Austria, 2008, ISBN 3-900051-07-0. [Online]. Available: <http://www.R-project.org>

## CHAPTER 2

### TECHNICAL BACKGROUND

This dissertation builds upon the PBM framework proposed by Cates et al. [1] and applies it to a wider class of biological shapes. The PBM framework is extended to include models of shape change over time. This work also adds new features, based on geodesic distances, to improve sensitivity of the correspondences in presence of geometric complexity and high variability in certain shape classes. These new features involve computation of geodesic distances between pairs of dynamic correspondences and also between correspondences and predefined landmarks. Computing such a large number of geodesic distances is prohibitive without the use of fast, parallel algorithms for solving partial differential equations (PDEs). The meshFIM algorithm, given by Fu et al. [2], performs fast computation of geodesic distances between vertices on a triangle mesh and has proved immensely useful in key aspects of this work dealing with correspondences for nonregular surfaces.

This chapter provides a detailed technical background of the two components mentioned above. The first half describes the PBM framework and establishes relevant mathematical notation for the next four chapters. It also gives an overview of the shape analysis pipeline used in this work. The second half of this chapter discusses details of the meshFIM algorithm for fast geodesic distance computation and concludes with a description of the preprocessing steps required to obtain geodesic distances for the methods in this dissertation.

#### 2.1 Particle Based Modeling (PBM) Framework

In accordance with the principal of parsimony in model selection, the particle-based correspondence optimization method [1, 3] seeks to maximize geometric accuracy and statistical simplicity of the shape model. The general strategy of this method is to represent correspondences as point sets that are distributed across an ensemble of similar shapes by gradient descent optimization of an energy function. Point sets are modeled nonparametrically as dynamic *particle systems*, a terminology from the computer graphics literature (e.g., [4]), in a method that operates with few free parameters. A complete description of

the particle distribution model is beyond the scope of this dissertation and the reader is referred to [5]. Below is an overview of the mathematical framework and the major steps in the PBM pipeline.

### 2.1.1 Surface Representation and Correspondences

The PBM framework mathematically defines a surface as a smooth manifold of co-dimension one, embedded in a Euclidean vector space. The surface may be open or closed, based on whether the manifold has a boundary or not. A closed surface is a manifold with no boundary, containing a single connected component. Examples of closed surfaces studied in this dissertation include brain structures like the left, right hemispheres and the cerebellum. An open surface is a manifold with a boundary, defined in biological studies as a region of interest within a larger structure. An example of an open surface studied in this work is the head shape enclosing the brain structures and bounded by a cutting plane. Fig. 2.1 shows two views of the brain structures and head shape as examples of closed and open surfaces, respectively. The following discussion assumes closed surfaces. Open surfaces are discussed in Chapter 3.

The surface representation first proposed in [6] is employed and numerical approaches by Meyer et al. [4] are adapted to create a particle system representation for each shape in the population. These particle systems are then allowed to interact to obtain optimal correspondences across shapes in the population. Particle system representations avoid problems of parametric representations and are not limited to specific topologies. Individual particles also do not have fixed neighbors, unlike vertices on a mesh, and can freely move past one another in the optimization process to form an optimal model.

Given a sample of  $N$  surface representations from a population of surfaces, embedded

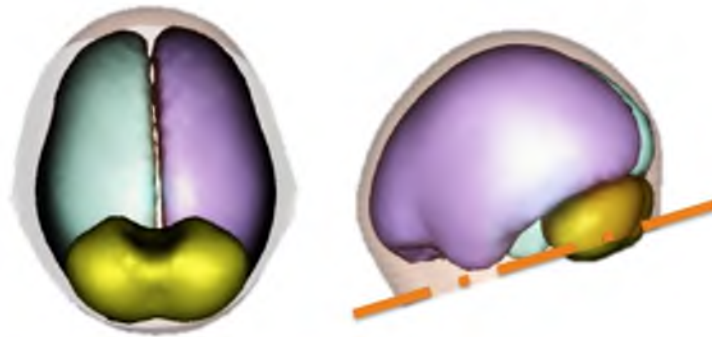


**Figure 2.1.** Two views of closed surfaces: left hemisphere (violet), right hemisphere (green), cerebellum (yellow), and open surface: head shape (transparent orange), with the cutting plane used to define the head shape boundary

in a  $d$ -dimensional Cartesian space, the correspondence model is defined as follows. The shape variation is modeled using a set of  $M$   $d$ -dimensional points ( $x_i$ ) on each of the  $N$  surfaces. Each of these points is called a *correspondence*. Following the convention in [7], the set of  $M$  points is called a *configuration*, and the set of all possible configurations is the *configuration space*. An example of a shape configuration is shown at the left of Fig. 2.2. The  $M \times d$  matrix of Cartesian coordinates in a configuration is the configuration matrix,  $\mathbf{C}$ , shown to the right of Fig. 2.2. Correspondence between shapes is established by the ordering of points in the  $N$  configurations and the rows of the matrix  $\mathbf{C}$ . The geometric variation in the shapes is then described by the variation in the rows of  $\mathbf{C}$ .

Concatenating the correspondence positions for each configuration into a vector makes it possible to map the configuration into a single point  $X$  in a  $dM$  dimensional space, called *shape space*. The set of shapes forms a distribution in shape space, whose statistical properties can be estimated. A cartoon depiction of the mapping of a configuration from the hand shapes to a point in the high dimensional shape space is shown on the left of Fig. 2.3. The middle graph shows a hypothetical distribution of hand shapes in the shape space. Even though the graph is depicted to be two dimensional, the real shape space is  $dM$  dimensional. Fig. 2.3 also illustrates a cartoon depiction of the basic correspondence optimization strategy from the initial distribution in shape space to an optimized distribution with less variance. In this strategy, movement of individual points on a configuration results in a corresponding

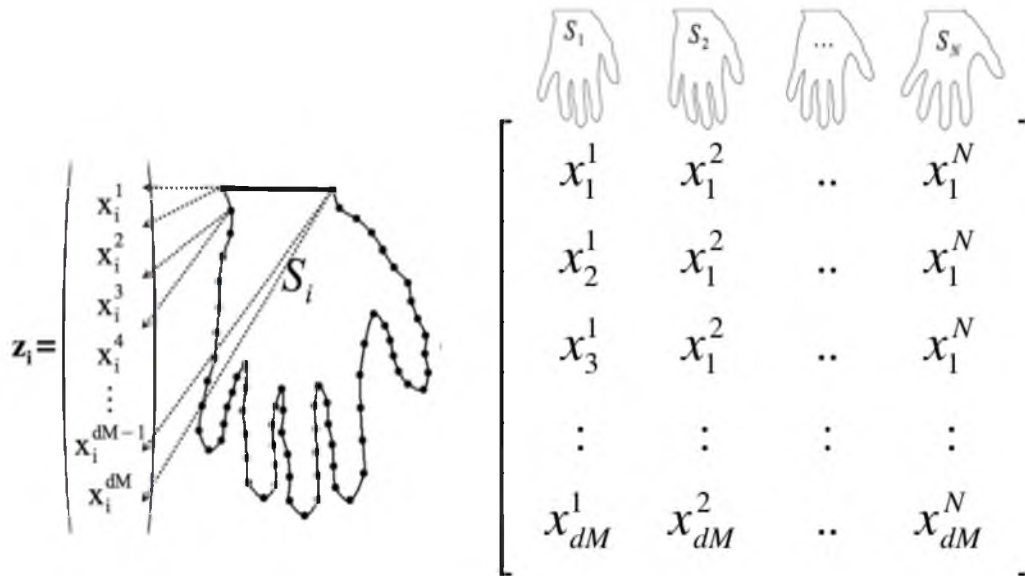


**Figure 2.2.** An example of a shape configuration (left) and the configuration matrix (right) for a set of hand shapes

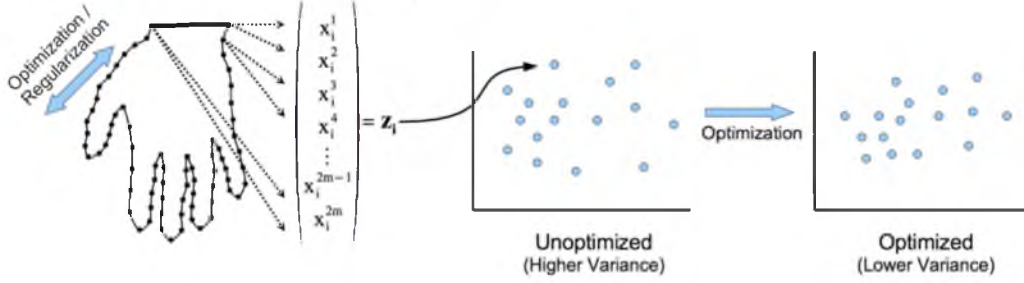


**Figure 2.3.** An illustration of the correspondence optimization in shape space

movement of the configuration in shape space.

### 2.1.2 Surface Entropy

Let a surface be defined as a smooth, closed manifold of codimension one, which is a subset of  $\mathfrak{R}^d$  (e.g.,  $d = 3$  for volumes). This surface  $\mathcal{S} \subset \mathfrak{R}^d$  is sampled using a discrete set of  $N$  points that are considered random variables  $\mathbf{Z} = (\mathbf{X}_1, \mathbf{X}_2, \dots, \mathbf{X}_N)^T$ ,  $\mathbf{X} \in \mathfrak{R}^d$  drawn from a probability density function (PDF),  $p(\mathbf{X})$ . A realization of this PDF is denoted with lower case, to obtain  $\mathbf{z} = (\mathbf{x}_1, \mathbf{x}_2, \dots, \mathbf{x}_N)^T$ , where  $\mathbf{z} \in \mathcal{S}^N$ . The probability of a realization  $\mathbf{x}$  is  $p(\mathbf{X} = \mathbf{x})$ , which is simply denoted as  $p(\mathbf{x})$ . The amount of information contained in such a random sampling is, in the limit, the differential entropy of the PDF, which is

$$H[\mathbf{X}] = - \int_{\mathcal{S}} p(\mathbf{x}) \log p(\mathbf{x}) d\mathbf{x} = -E\{\log p(\mathbf{X})\} \quad (2.1)$$

where  $E\{\cdot\}$  is the expectation.

Approximating the expectation by the sample mean gives

$$H[\mathbf{X}] \approx -\frac{1}{M} \sum_i \log p(\mathbf{x}_i) \quad (2.2)$$

The PBM algorithm manipulates particle positions using a gradient descent optimization on a cost function  $C(x_1, \dots, \mathbf{x}_M) \approx H(X)$ , which is an approximation of negative entropy. The resulting optimization problem uses a Gauss-Seidel update with forward differences. Each particle therefore moves with a time step and positional update  $\mathbf{x}_i \leftarrow \mathbf{x}_i - \gamma \frac{\partial C}{\partial \mathbf{x}_i}$ . The partial gradient of  $C$  for particle  $i$  evaluates to,

$$\frac{\partial C}{\partial \mathbf{x}_i} = \frac{1}{M} \sum_{j=1}^M \frac{\frac{\partial}{\partial \mathbf{x}_i} p(\mathbf{x}_j)}{p(\mathbf{x}_j)} \quad (2.3)$$

To estimate  $p(\mathbf{x}_i)$ , a nonparametric Parzen window estimation based on particle configurations is used. The probability of the particle position is given by the mixture of multivariate Gaussian kernels,

$$p(\mathbf{x}, \sigma) \approx \frac{1}{M} \sum_{j=1}^M G(\mathbf{x} - \mathbf{x}_j, \sigma) \quad (2.4)$$

where  $G(\mathbf{x} - \mathbf{x}_j, \sigma)$  is a  $d$ -dimensional, isotropic Gaussian with standard deviation  $\sigma$ . To simplify the computation, the PBM formulation instead considers  $p$  to be fixed for a given particle update: for  $j \neq i$ , the estimation of the density function at  $j$  is allowed to lag behind the update of particle position  $i$ . The final partial derivative of  $p$  with respect to position is computed then to be

$$\frac{\partial C}{\partial \mathbf{x}_i} \approx \frac{1}{M} \sum_{j=1}^M \frac{G(\mathbf{x}_i - \mathbf{x}_j, \sigma_i)(\mathbf{x}_i - \mathbf{x}_j)}{\sigma_i^2 p(\mathbf{x}_i, \sigma_i)} \quad (2.5)$$

$$= \frac{1}{M} \sum_{j=1}^M w_{ij}(\mathbf{x}_i - \mathbf{x}_j) \quad (2.6)$$

where  $w_{ij}$  are Gaussian weights based on interparticle distance and  $\sum_j w_{ij} = 1$ . To minimize  $C$ , the particles must move away from each other. Thus, particles move under a repulsive force and are constrained to lie on the surface. The reader is referred to [5] for the full mathematical derivation of this gradient.

The minimization described above gives a uniform sampling of a surface. An adaptive sampling scheme is desired for some applications, where higher order shape information is more effective. Sampling high curvature regions more densely also ensures a reliable degree of regularity in the tangent planes between adjacent particles in these regions. Such an adaptive sampling can be obtained by modifying the Parzen windowing in Eqn. 2.4 as shown below.

$$\tilde{p}(\mathbf{x}_i) \approx \frac{1}{M} \sum_{j=1, j \neq i}^M G\left(\frac{\mathbf{x}_i - \mathbf{x}_j}{k_j}, \sigma_i\right) \quad (2.7)$$

where  $k_j$  is a scaling term proportional to the curvature magnitude computed at each neighbor particle  $j$ . This scaling effectively warps space in response to local curvature and computes a uniform sampling based on maximum entropy in the warped space. This results in an adaptive sampling in the unwarped space, with a more dense packing of points in regions of high curvature. The scaling term given by Meyer et al. [4] is used. The reader is directed to [5] for further details of the scaling term and computation of the modified gradient.

### 2.1.3 Ensemble Entropy

An ensemble comprised of  $M$  surfaces,  $\mathcal{E} = \mathbf{z}^1, \dots, \mathbf{z}^M$  can be described by a  $Nd \times M$  matrix of particle positions  $\mathbf{P} = (\mathbf{x}_j^k)$ , where  $k = 1, \dots, M$  and  $j = 1, \dots, N$ . Let  $\mathbf{z}^k \in \mathfrak{R}^{dN}$

be an instance of a random variable  $\mathbf{Z}$ , then, modeling  $p(\mathbf{Z})$  parametrically as a Gaussian with covariance  $\mathbf{\Sigma}$  gives the entropy  $H(\mathbf{Z}) \approx \frac{1}{2} \log |\mathbf{\Sigma}| = \frac{1}{2} \sum_{j=1}^{dN} \log \lambda_j$ , where  $\lambda_j$  are the eigenvalues of  $\mathbf{\Sigma}$ . The covariance is estimated from the data, letting  $\mathbf{Y}$  denote the matrix of (centered) points for the ensemble, which gives  $\mathbf{\Sigma} = (1/(dNM - 1))\mathbf{Y}\mathbf{Y}^T$ .

Because  $dN > M$ , covariance computation is performed on the  $M$  dimensional dual space. As detailed in [5], the covariances  $|\mathbf{\Sigma}|$  and  $|\mathbf{\Sigma}^T|$  are equivalent up to a constant regularizing factor  $\alpha$ , thus giving the final cost function associated with ensemble entropy:

$$G(\mathbf{P}) = \frac{1}{2} \log |\mathbf{\Sigma}^T| = \frac{1}{2} \log \left| \frac{1}{dNM - 1} \mathbf{Y}^T \mathbf{Y} + \alpha \mathbf{I} \right| \quad (2.8)$$

The computation of the gradient computation of the ensemble entropy, a strategy similar to the gradient computation for the surface entropy is applied, and the estimation of the mean of the distribution  $\mathbf{Z}$  is allowed to lag behind the updates given by  $\frac{\partial G}{\partial \mathbf{P}}$ . This simplifies the gradient computation by allowing the assumption that  $\frac{\partial G}{\partial \mathbf{P}} \approx \frac{\partial G}{\partial \mathbf{Y}}$ . This approximation becomes more accurate as the number of shape samples is increased, and changes in individual particle positions have increasingly less of an effect on the sample mean. The matrix of partial derivatives of  $G$  with respect to  $\mathbf{Y}$ , including the regularization, is given by [5],

$$\frac{\partial G}{\partial \mathbf{P}} \approx \mathbf{Y}(\mathbf{Y}^T \mathbf{Y} + \alpha \mathbf{I})^{-1} \quad (2.9)$$

The regularization  $\alpha$  thus accounts for a diminishing determinant, and the negative gradient of  $G$  gives a vector of updates for the entire system and is recomputed once per system update.

#### 2.1.4 Cost Function

The final energy function is a combination of the surface entropy (Eqn. 2.2) and the ensemble entropy (Eqn. 2.8), given by

$$Q = H(\mathbf{Z}) - \sum_{k=1}^M H(\mathbf{X}^k) \quad (2.10)$$

Correspondence positions are optimized by gradient descent on the energy function  $Q$ , which balances the negative entropy of the distribution of particles in configuration space with the positive entropy of the distribution of the configurations in shape space.

The correspondence points are updated using a combination of the negative gradient from the ensemble entropy and the gradient of the surface entropy. The update for correspondence point  $j$  on shape  $k$  is given by

$$\mathbf{x}_j^k \leftarrow \mathbf{x}_j^k + \gamma \left[ -\frac{\partial G}{\partial \mathbf{x}_j^k} + \frac{\partial C}{\partial \mathbf{x}_j^k} \right] \quad (2.11)$$

The reader is referred to [5] for further details on the various parameter settings.

### 2.1.5 ShapeWorks Pipeline

Any set of implicit surfaces can be used as an input to the PBM framework. The shapes are preprocessed to remove antialiasing artifacts using the  $r$ -tightening algorithm [8]. This is followed by distance transform computation. Any suitably accurate distance transform can be used as the implicit surface required for the PBM framework. The final preprocessing step involves a Gaussian blurring of the distance transforms to remove high frequency artifacts that may be caused by numerical approximations.

The correspondences are initialized using a hierarchical splitting strategy. The initialization starts with a single particle on each shape, which is split to place a new particle nearby. This two-particle-per-shape system is allowed to relax until it reaches a steady state. This splitting followed by optimization continues till a user-defined number of correspondences are obtained. The generated models increase in detail with every split.

Once the user-defined number of particles have been initialized, GPA [9] is applied at regular intervals in the optimization process to remove any residual nonshape information from the model.

## 2.2 Fast Iterative Method (FIM)

The distance between each point  $a$  on the surface and every other point, can be conceived as the solution to the eikonal equation  $|\nabla u| = 1$  (e.g., [10–12]), using the boundary condition  $u(a) = 0$ . The fast iterative method (FIM) [12] is extremely efficient on SIMD architectures, but works only for regular grids. An intermediate representation based on unstructured triangular meshes is used to describe surfaces used in this dissertation. An extension of the FIM for triangular meshes, meshFIM, given by Fu et al. [2] is used for fast, efficient geodesic distance computation.

### 2.2.1 Solution of Eikonal Equation

Geodesic distance can be conceived as the numerical solution of the Eikonal equation, a special case of nonlinear Hamilton-Jacobi partial differential equations (PDEs), defined on a two-dimensional manifold with a scalar speed function

$$\begin{cases} H(\mathbf{x}, \nabla\phi) = |\nabla_{\mathfrak{S}}\phi(\mathbf{x})|^2 - \frac{1}{f^2(\mathbf{x})} = 0 & \forall \mathbf{x} \in \mathfrak{S} \subset \mathfrak{R}^3 \\ \phi(\mathbf{x}) = B(\mathbf{x}) & \forall \mathbf{x} \in \Omega \subset \mathfrak{S} \end{cases} \quad (2.12)$$

where  $\mathfrak{S}$  is a smooth two-dimensional manifold in  $\mathfrak{R}^3$ ,  $\nabla_{\mathfrak{S}}$  is the gradient operator in the tangent plane to the manifold,  $\phi(\mathbf{x})$  is the travel time or distance from the source,  $f(\mathbf{x})$  is

a positive speed function defined on  $\xi$ , and  $\Omega$  is a set of smooth boundary conditions. The solution is approximated on triangulation of  $\xi$ , denoted  $\xi_T$ , and is represented point-wise on the set of vertices  $V$  in  $S_T$ . This solution can be interpolated across triangles in a linear fashion.

### 2.2.2 Local Solver

In Eqn. 2.12, tessellation  $\xi_T$  is available for the manifold  $\xi$ , and the numerical solution of the equation  $\phi(\mathbf{x})$  is defined on the vertices of  $\xi_T$ . The solution at each vertex, or the travel time, is computed from the current value at the vertex and its *one-ring* neighbors, using a linear approximation on each triangle face. An example tessellation and one-ring of vertex  $v_1$  is shown in Fig. 2.4. At each vertex  $v_i$ , The approximate solution  $\phi_i \approx \phi(\mathbf{x}_i)$ , is set to be the minimum among the  $n$  values associated with each triangle in the one-ring.

Considering a triangle  $T_{1,2,3}$  in Fig. 2.5, an upwind scheme that complies with the causality property is used to compute the solution  $\phi_3$ , from values  $\phi_1$  and  $\phi_2$ . Locally, the characteristics are perpendicular to the gradient of  $\phi$  and the travel time to  $v_1$  must be determined by time associated with a line segment lying in the triangle  $T_{1,2,3}$ . If the difference in travel time between  $v_1$  to  $v_2$  is  $\phi_{1,2} = \phi_1 - \phi_2$  and vertices  $v_1$  and  $v_2$  are

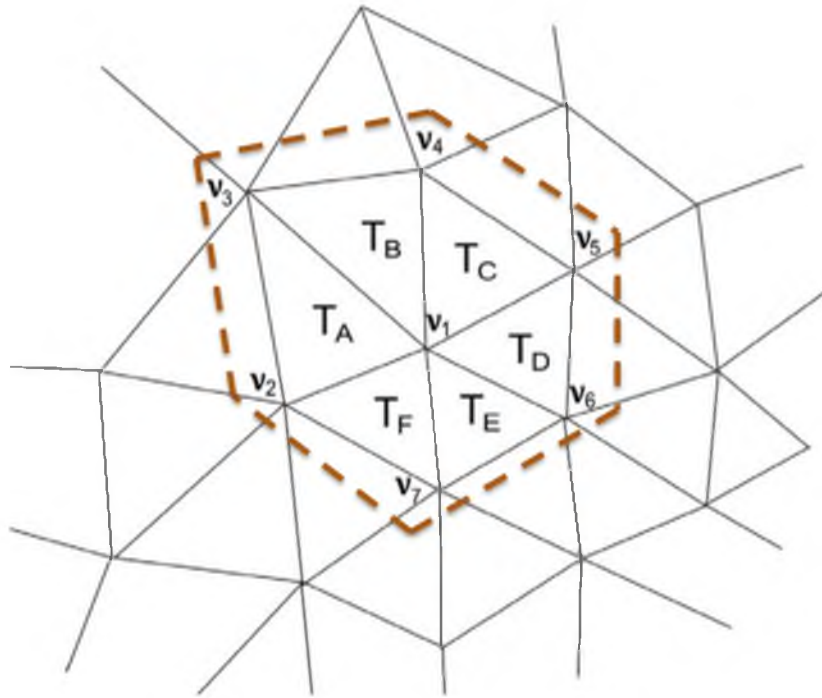


**Figure 2.4.** An example tessellation with the one-ring highlighted for vertex  $v_1$  (modified from [2])

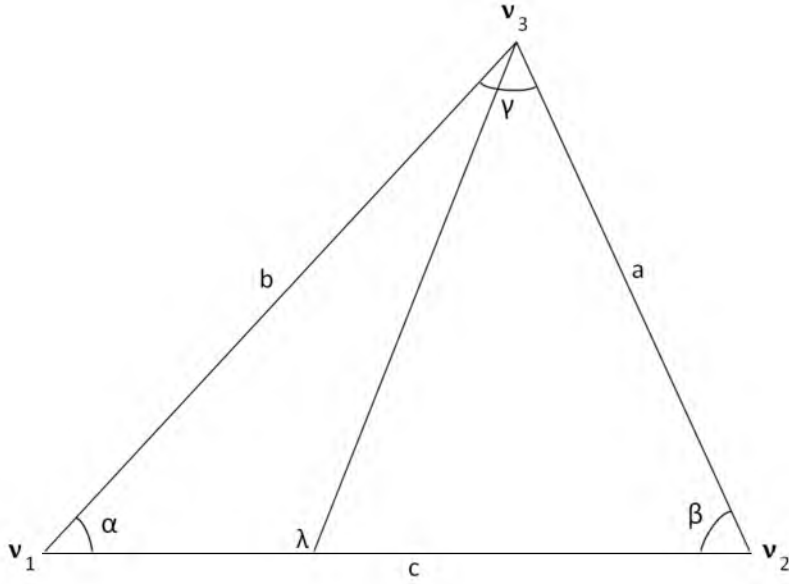


**Figure 2.5.** Triangle representation for upwind update at vertex  $v_3$

upwind of  $v_3$ , there is a characteristic passing through  $v_3$  that intersects edge  $\mathbf{e}_{1,2}$  at position  $\mathbf{x}_\lambda = \mathbf{x}_1 + \lambda \mathbf{e}_{1,2}$ , where  $\lambda$  is unknown and  $\lambda \in [0, 1]$  in order for the characteristic to intersect the edge. The line segment that describes the characteristic across  $T_{1,2,3}$  is

$$\mathbf{e}_{\lambda,3} = \mathbf{e}_{1,3} - \mathbf{e}_{1,\lambda} = \mathbf{e}_{1,3} - \lambda \mathbf{e}_{1,2} \quad (2.13)$$

Thus the travel time from  $\mathbf{x}_\lambda$  to  $\mathbf{x}_3$  can be computed as  $\phi_{\lambda,3} = f|\mathbf{e}_{\lambda,3}| = f|\mathbf{e}_{1,3} - \lambda \mathbf{e}_{1,2}|$ .

Using linear approximation,

$$\phi_\lambda = \phi(\mathbf{x}_\lambda) = \phi_1 + \lambda \phi_{1,2} \quad (2.14)$$

The solution at  $v_3$  is the solution at  $\mathbf{x}_\lambda$  plus the travel time from  $\mathbf{x}_\lambda$  to the vertex  $v_3$

$$\phi_3 = \phi_\lambda + \phi_{\lambda,3} = \lambda \phi_{1,2} + \phi_1 + f|\mathbf{e}_{1,3} - \lambda \mathbf{e}_{1,2}| \quad (2.15)$$

$\lambda$  must minimize  $\phi_3$  since the characteristic direction is the same as the gradient of the solution. Setting the derivative of Eqn. 2.15 with respect to  $\lambda$  to zero, results in the quadratic equation

$$p\lambda^2 + q\lambda + r = 0 \quad (2.16)$$

where

$$\begin{cases} p = c^2(f^2 c^2 - \phi_{1,2}^2) \\ q = -2bc(f^2 c^2 - \phi_{1,2}^2) \cos \alpha \\ r = f^2 c^2 b^2 \cos^2 \alpha - \phi_{1,2}^2 b^2. \end{cases} \quad (2.17)$$

The discriminant  $\Delta$  is defined as

$$\Delta = 4b^2c^2(f^2c^2 - \phi_{1,2}^2)\phi_{1,2}^2 \sin^2 \alpha$$

and there are three possible cases in the solution. When  $(f^2c^2 - \phi_{1,2}^2) \geq 0$ , the real root of Eqn. 2.16 exists, and solutions can be found on the line segment  $e_{1,2}$  under some conditions. Otherwise, the vertices  $v_1$  and  $v_2$  are not upwind of  $v_3$ . Further details about the implementation and the special case of obtuse triangles are elaborated in [2].

### 2.2.3 Algorithm for CPU

Fig. 2.6 shows the CPU meshFIM algorithm based on asynchronous updates based on the upwind scheme.

meshFIM( $V, B, L$ )

---

**comment:** 1. Initialization ( $V$ : all vertices,  $L$ : active list,  $B$ : seed vertices)

**for each**  $v \in V$

**do** {  
     **if**  $v \in B$   
         **then**  $\Phi_v \leftarrow 0$   
     **else**  $\Phi_v \leftarrow \infty$

**for each**  $v \in V$

**do** {  
     **if** any 1-ring vertex of  $v \in B$   
         **then** add  $v$  to  $L$

**comment:** 2. Update vertices in  $L$

**while**  $L$  is not empty

**do** {  
     **for each**  $v \in V$   
         **do** {  
              $p \leftarrow \Phi_v$   
              $q \leftarrow \text{Update}(v)$   
             **if**  $|p - q| < \epsilon$   
                 **then** {  
                     **for each** adjacent neighbor  $v_{nb}$  of  $v$   
                         **if**  $v_{nb}$  is not in  $L$   
                             **do** {  
                                  $p \leftarrow \Phi_{v_{nb}}$   
                                  $q \leftarrow \text{Update}(v_{nb})$   
                                 **if**  $p > q$   
                                     **then** {  
    $\Phi_{v_{nb}} \leftarrow q$   
   add  $v_{nb}$  to  $L$

remove  $v$  from  $L$

---

**Figure 2.6.** CPU algorithm for meshFIM updates, adapted from [2]

Vertices are updated one at a time. After each vertex is updated, its value is consistent of its upwind neighbors, and each update is immediately transferred to the solution to be used by subsequent updates.

The algorithm maintains a list of active vertices, and sequentially updates values using the upwind scheme described above, at vertices in the list until the last element is reached. Thereafter, the list simply loops back to the beginning. This process continues until the active list is empty. Once a vertex is updated, its value is consistent with the upwind neighbors, and each update is immediately transferred to the solution to be used by subsequent updates.

A vertex is kept on the active list until the difference between the old and new value falls below a predefined tolerance  $\epsilon$ . Once the tolerance level is reached, this vertex is called  *$\epsilon$ -converged* and removed from the active list along with all of its potentially downwind neighbors. These downwind neighbors are updated one final time before removal and are added back to the list if they are not  *$\epsilon$ -converged*. The reader is referred to [2] for further analysis and extensions of the meshFIM algorithm.

The CPU version of the meshFIM algorithm described above is used to compute geodesic distances in this work. These distances are precomputed between all vertices of an intermediate triangle mesh representation for all shapes in the population, and the values are interpolated on the implicit surface using a double-interpolation scheme detailed in Chapter 5.

## 2.3 References

- [1] J. Cates, P. T. Fletcher, M. Styner, M. Shenton, and R. Whitaker, “Shape modeling and analysis with entropy-based particle systems,” in *Proc. IPMI*, 2007, pp. 333–345.
- [2] Z. Fu, W.-K. Jeong, Y. Pan, R. M. Kirby, and R. T. Whitaker, “A fast iterative method for solving the eikonal equation on triangulated surfaces,” *SIAM J. Sci. Comput.*, vol. 33, no. 5, pp. 2468–2488, Oct. 2011. [Online]. Available: <http://dx.doi.org/10.1137/100788951>
- [3] J. Cates, P. Fletcher, and R. Whitaker, “Entropy-based particle systems for shape correspondence,” in *Proc. MICCAI MFCA Workshop*, 2006, pp. 90–99.
- [4] M. D. Meyer, P. Georgel, and R. T. Whitaker, “Robust particle systems for curvature dependent sampling of implicit surfaces,” in *Proc. IEEE SMI*, June 2005, pp. 124–133.
- [5] J. Cates, “Shape modeling and analysis with entropy-based particle systems,” Ph.D. dissertation, University of Utah, 2010.
- [6] A. P. Witkin and P. S. Heckbert, “Using particles to sample and control implicit surfaces,” in *Proc. SIGGRAPH*, 1994, pp. 269–277.
- [7] I. Dryden and K. Mardia, *Statistical shape analysis*. Wiley, 1998.
- [8] J. Williams and J. Rossignac, “Tightening: curvature-limiting morphological simplification,” in *Proc. SPM*, 2005, pp. 107–112.
- [9] C. Goodall, “Procrustes methods in the statistical analysis of shape.” *J. R. Stat. Soc. Series. B. Stat. Methodol.*, vol. 53, pp. 285–339, 1991.
- [10] J. A. Sethian, “A fast marching level set method for monotonically advancing fronts,” in *PNAS*, 1995, pp. 1591–1595.
- [11] J. Qian, Y. Zhang, and H. Zhao, “Fast sweeping methods for eikonal equations on triangular meshes,” *SIAM J. Numer. Anal.*, vol. 45, no. 1, pp. 83–107, 2007.
- [12] W. Jeong and R. Whitaker, “A fast iterative method for eikonal equations,” *SIAM J. Sci. Comput.*, vol. 30, no. 5, pp. 2512–2534, 2008.

**CHAPTER 3**

**PARTICLE BASED SHAPE REGRESSION  
OF OPEN SURFACES WITH  
APPLICATIONS TO  
DEVELOPMENTAL  
NEUROIMAGING**

This chapter is a reprint of Proc. MICCAI, Particle based shape regression of open surfaces with applications to developmental neuroimaging, vol. 2, 2009, pp. 167-174, M Datar, J Cates, PT Fletcher, S Gouttard, G Gerig, RT Whitaker, with permission of Springer

# Particle Based Shape Regression of Open Surfaces with Applications to Developmental Neuroimaging

Manasi Datar, Joshua Cates, P. Thomas Fletcher, Sylvain Gouttard,  
Guido Gerig, and Ross Whitaker

Scientific Computing and Imaging Institute  
University of Utah  
Salt Lake City, Utah

**Abstract.** Shape regression promises to be an important tool to study the relationship between anatomy and underlying clinical or biological parameters, such as age. In this paper we propose a new method to building shape models that incorporates regression analysis in the process of optimizing correspondences on a set of open surfaces. The statistical significance of the dependence is evaluated using permutation tests designed to estimate the likelihood of achieving the observed statistics under numerous rearrangements of the shape parameters with respect to the explanatory variable. We demonstrate the method on synthetic data and provide a new results on clinical MRI data related to early development of the human head.

## 1 Introduction

Technologies for shape representation and statistical shape analysis are important for several problems in medical imaging including image segmentation, quantitative analysis of anatomy, and group comparisons. A widely used approach to evaluating shapes is assign correspondences or landmarks to shapes (curves, or surfaces) and to compare the positions or configurations of these landmarks. This approach has benefitted in recent years from methods for the automatic placement of landmarks in a way that captures the statistical properties of an ensemble of images [1,2,3]. Finding correspondences that minimize description length [2] or entropy [1] has been shown to generate shape models that systematically capture the underlying variability of the population and conform, qualitatively, to the underlying anatomy. This paper extends the method of Cates et al. [1], which uses an variational formulation of ensemble entropy to position dense collections of landmarks, or *particles*.

On the clinical front, quantitative magnetic resonance imaging has significantly advanced our understanding of brain development during childhood and adolescence. Courchesne et al. [4] describe differences in growth patterns in autism compared to controls. However, these studies do not include children below the age of 4 years. Data measured in infants from birth to 4 years are mostly *volumetric measurements*, such as intracranial volume and volumes of

brain lobes and subcortical structures [5]. Whereas this selection of previous work demonstrates very active research towards determining brain growth at early stage of development, there is little data on modelling head and brain growth across a continuum of time and almost no work on the study of how development influences shape.

In developmental analyses, such as paediatric neurodevelopment, *shape regression* gives aggregate models of growth, with variability. Thus shape analysis promises to give not only basic insights into the process of development, but also allow comparisons of individuals against normative models. Of course, precise characterizations of these relationships will require shape models that can tease apart those aspects of shape variability that are explained by the underlying variables and those that are not. Likewise, in order to understand the statistical significance of such relationships we will need a systematic, unbiased method for testing these correlations. These are the topics addressed in this paper.

## 2 Methodology

This section gives a brief overview of the particle-system correspondence optimization method, which is first described in [1]. The general strategy of this method is to represent correspondences as point sets that are distributed across an ensemble of similar shapes by a gradient descent optimization of an objective function that quantifies the entropy of the system. Our proposed extension to this method incorporates a linear regression model into the correspondence optimization. We also present a new methodology for correspondence optimization on open surfaces where surface boundaries are defined by arbitrary geometric constraints—which is important for studying paediatric head shape.

### Correspondence Optimization

We define a surface as a smooth, closed manifold of codimension one, which is a subset of  $\mathbb{R}^d$  (e.g.,  $d = 3$  for volumes). We sample a surface  $\mathcal{S} \subset \mathbb{R}^d$  using a discrete set of  $N$  points that are considered random variables  $\mathbf{Z} = (\mathbf{X}_1, \mathbf{X}_2, \dots, \mathbf{X}_N)^T$ ,  $\mathbf{X} \in \mathbb{R}^d$  drawn from a probability density function (PDF),  $p(\mathbf{X})$ . We denote a realization of this PDF with lower case, and thus we have  $\mathbf{z} = (\mathbf{x}_1, \mathbf{x}_2, \dots, \mathbf{x}_N)^T$ , where  $\mathbf{z} \in \mathcal{S}^N$ . The probability of a realization  $\mathbf{x}$  is  $p(\mathbf{X} = \mathbf{x})$ , which we denote simply as  $p(\mathbf{x})$ .

The amount of information contained in such a random sampling is, in the limit, the differential entropy of the PDF, which is

$$H[\mathbf{X}] = - \int_{\mathcal{S}} p(\mathbf{x}) \log p(\mathbf{x}) dx = -E\{\log p(\mathbf{X})\}, \quad (1)$$

where  $E\{\cdot\}$  is the expectation. Approximating the expectation by the sample mean, we have  $H[\mathbf{X}] \approx -\frac{1}{Nd} \sum_i \log p(\mathbf{x}_i)$ . To estimate  $p(\mathbf{x}_i)$ , we use a non-parametric Parzen windowing estimation, modified to scale density estimation in proportion to local curvature magnitude. The kernel width  $\sigma$  is chosen adaptively at each  $\mathbf{x}_i$  to maximize the likelihood of that position. We refer to the positions  $\mathbf{x}$  as *particles*, and a set of particles as a *particle system*.

Now consider an ensemble  $\mathcal{E}$ , which is a collection of  $M$  surfaces, each with their own set of particles, i.e.,  $\mathcal{E} = \mathbf{z}^1, \dots, \mathbf{z}^M$ . The ordering of the particles on each shape implies a correspondence among shapes, and thus we have a matrix of particle positions  $P = \mathbf{x}_j^k$ , with particle positions along the rows and shapes across the columns. We model  $\mathbf{z}^k \in \mathbb{R}^{N^d}$  as an instance of a random variable  $\mathbf{Z}$ , and minimize a combined ensemble and shape cost function

$$Q = H(\mathbf{Z}) - \sum_k H(P^k), \quad (2)$$

which favors a compact ensemble representation balanced against a uniform distribution of particles on each surface. Given the low number of samples relative to the dimensionality of the space, we use a parametric approach described in [1] for density estimation in the space of shapes. The entropy cost function  $Q$  is minimized using a gradient descent strategy to manipulate particle positions (and, thus, also correspondence positions). The surface constraint is specified by the zero set of a scalar function  $F(x)$ . This optimization strategy balances entropy of individual surface samplings with the entropy of the shape model, maximizing the former for geometric accuracy (a good sampling) and minimizing the latter to produce a compact model.

Any set of implicitly defined surfaces is appropriate as input to this framework. For this paper, we use binary segmentations, which contain an implicit shape surface at the interface of the labeled pixels and the background. To remove aliasing artifacts in these segmentations, we use the  $r$ -tightening algorithm given by Williams et al. [6]. Correspondence optimizations are initialized with the splitting strategy described in [1], starting with a single particle on each object. We use a Procrustes algorithm, applied at regular intervals during the optimization, to align shapes with respect to rotation and translation, and to normalize with respect to scale.

**Correspondence with Regression Against Explanatory Variables.** With the assumption of a Gaussian distribution in the space of shapes, we can introduce a generative statistical model

$$\mathbf{z} = \mu + \epsilon, \epsilon \sim \mathcal{N}(\mathbf{0}, \Sigma) \quad (3)$$

for particle correspondence positions, where  $\mu$  is the vector of mean correspondences, and  $\epsilon$  is normally-distributed error. Replacing  $\mu$  in this model with a function of an explanatory variable  $t$  gives the more general, *regression* model

$$\mathbf{z} = f(t) + \hat{\epsilon}, \hat{\epsilon} \sim \mathcal{N}(\mathbf{0}, \hat{\Sigma}). \quad (4)$$

The optimization described in the previous section minimizes the entropy associated with  $\epsilon$ , which is the difference from the mean. In this paper, we propose to optimize correspondences under the regression model in Eqn. 4 by instead minimizing entropy associated with  $\hat{\epsilon}$ , the residual from the model. Considering particle correspondence to be a linear function of  $t$ , given as  $f(t) = \mathbf{a} + \mathbf{b}t$ , we

need an estimate of parameters  $\mathbf{a}$  and  $\mathbf{b}$  to compute  $\hat{\epsilon}$ . We estimate these with a least-squares fit to the correspondence data,

$$\arg \min_{\mathbf{a}, \mathbf{b}} E(\mathbf{a}, \mathbf{b}) = \frac{1}{2} \sum_k [(\mathbf{a} + \mathbf{b}t_k) - \mathbf{z}_k]^T \Sigma^{-1} [(\mathbf{a} + \mathbf{b}t_k) - \mathbf{z}_k]. \quad (5)$$

Setting  $\frac{\delta E}{\delta \mathbf{a}} = \frac{\delta E}{\delta \mathbf{b}} = 0$  and solving for  $\mathbf{a}$  and  $\mathbf{b}$ , we have  $\mathbf{a} = \frac{1}{n} (\sum_k \mathbf{z}_k - \sum_k \mathbf{b}t_k)$ , and  $\mathbf{b} = (\sum_k t_k \mathbf{z}_k - \sum_k \mathbf{z}_k \sum_k t_k) / (\sum_k t_k^2 - (\sum_k t_k)^2)$ .

The proposed regression model optimization algorithm then proceeds as follows. Correspondences are first optimized under the nonregression model (Eqn 3) to minimize the entropy associated with the total error  $\epsilon$ , and to establish an initial estimate for  $\mathbf{a}$  and  $\mathbf{b}$ . We then follow the same optimization procedure as described in Section. 2, but replace the covariance of the model with the covariance of the underlying residual relative to the generative model. We interleave the two estimation problems, and thus the parameters  $\mathbf{a}$  and  $\mathbf{b}$  are re-estimated after each iteration of the gradient descent on the particle positions.

**Correspondences on Open Surfaces.** To compute correspondence positions on a set of *open* surfaces, we propose an extension to the sampling method reviewed in Section. 2. The proposed method is to define the boundary as the intersection of the surface  $\mathcal{S}$  with a set of geometric primitives, such as cutting planes and spheres. Our goal is to formulate the interactions with these boundaries so that the positions of these constraints has as little influence as possible on the statistical shape model.

For each geometric primitive, we construct a *virtual* particle distribution that consists of all of the closest points on its surface to the particles  $\mathbf{x}_i$  on  $\mathcal{S}$ . During the gradient descent optimization, particles  $\mathbf{x}_i$  interact with the virtual particles, and are therefore effectively repelled from the geometric primitives, and thus from the open surface boundary. The virtual distributions are updated after each iteration as the particles on  $\mathcal{S}$  redistribute under the optimization. Because the virtual particles are allowed to factor into the Parzen windowing kernel size estimation, particles  $\mathbf{x}_i$  maintain a distance from the boundary proportional to their density on the surface  $\mathcal{S}$ . In this way, features near the boundary may be sampled, but particles are never allowed to lie on the actual boundary itself. One such configuration is shown in Figure. 1



**Fig. 1.** Particle system with geometric primitives defining the boundary

**Permutation Test of Significance.** Analysis of variance (ANOVA) is the standard parametric test for testing if the explanatory variables have a significant effect in a linear regression. The test statistic used is

$$T = \frac{R^2/(m-1)}{(1-R^2)/(n-m)}, \quad (6)$$

where  $R^2$  is Pearson's coefficient of regression, generally defined as  $R^2 = 1 - \frac{SS_{err}}{SS_{tot}}$ , where  $SS_{err}$  is the sum-squared residual error, and  $SS_{tot}$  represents total variance in the data. In general,  $R^2$  can be related to the unexplained variance of the generated model, and is used to measure the *goodness-of-fit* for the regression model. When the residuals of the linear model are iid Gaussian, the statistic  $T$  follows an  $F$  distribution with  $m - 1$  and  $n - m$  degrees of freedom under the null hypothesis.

In this case where the outcome variables are correspondence-optimized shape parameters, the underlying assumptions of the parametric  $F$ -test may not hold. Furthermore, optimization with knowledge of the underlying parameter could lead to optimistic estimates of significance, because we are explicitly minimizing the residual. To overcome this, we propose a nonparametric permutation test for significance. Permutation tests for regression work by permuting the values of the explanatory variables. This allows us to compute a distribution of our test statistic under the null hypothesis that the explanatory variable has no relationship to the dependent variable. Given data  $(z_i, t_i)$ , we generate the  $k$ th permuted data set as  $(z_i, t_{\pi_k(i)})$ , where  $\pi_k$  is a permutation of  $1, \dots, n$ . For each permutation we compute a test statistic  $T_k$  using (6). Then comparing our unpermuted test statistic  $T$  to the distribution of  $T_k$ , we can compute the  $p$ -value as the percentage of  $T_k$  that are greater than  $T$ . Notice, that for the case of regression-optimized correspondences, described in Section 2, we perform a the correspondence optimization on *each* permutation separately, and thus *the results of our permutation test are not biased by the correspondence method*.

### 3 Results and Discussion

This section details experiments designed to illustrate and validate the proposed method. First, we present an experiment with synthetically generated tori to illustrate the applicability of the method and validation based on permutation tests. Next, we present an application to the study of early growth of head shapes extracted from structural MRI data.

To illustrate and validate the proposed methods, we performed two experiments on sets of 40 synthetically generated tori, parameterized by the small radius  $r$  and the large radius  $R$ . The values for the shape parameters were chosen as independent functions of a uniformly distributed explanatory variable  $t$ . The definition of  $R^2$ , used to compute the test statistic as explained in Section. 2, is extended to include the two independent variables for this experiment:

$$R^2 = 1 - \frac{(SS_{err})_r + (SS_{err})_R}{(SS_{tot})_r + (SS_{tot})_R}. \quad (7)$$

We examine sets of time-dependent shapes with  $p$ -values  $\{0.01, 0.1\}$  in order to examine the performance of the system with and without significance. To construct these example data sets, we use the value for the statistic  $T$  (look up from the  $F$ -distribution) to generate a target  $R^2$ . The values of  $r$  and  $R$  are chosen such that the  $R^2$  of the generated set is approximately equal to the

target  $R^2$  for that experiment. Along with explicit correspondences generated from the standard torus parametrization, we use the correspondence methods from Section. 2, optimization with and without an underlying regression model, to optimize correspondences using 256 particles on each shape. An analysis of the resulting models showed that all three sets of correspondences exhibited two pure modes of variation.

**Synthetic Data (Tori).** Here we present the results of the statistical analysis of the tori test data using permutation tests consisting of 1000 permutations of the explanatory variable  $t$ . For the correspondences we compute the test statistics using the two dominant modes from a PCA on the set of correspondences. The procedure described in Section. 2 is then applied to get the corresponding  $p$ -values. Table. 1 shows the results of the two permutation tests for the explicit correspondences, and correspondences generated using the proposed methods. A comparison of the parametric  $p$ -value with the  $p$ -values obtained by the permutation tests confirms that the proposed methods preserve the relationship between the explanatory variable and the dependent variables. The correspondence-based approaches, particularly with the regression model, show greater significance than the parametric case. This might be an inherent property of the statistic or it could be an artifact due to the limited number of example datasets and the limited number of permutations. Future work will include more datasets, more permutations, and a bootstrapping procedure to analyze variability of the  $p$ -values computed by the various methods.

**Table 1.** Results of permutation tests (1000 permutations)

$p$ -value (theory)	$p$ -value (parametric)	Correspondence Type		
		Explicit	Min. Entropy	Regression-based
0.01	0.011	0.011	0.007	0.004
0.1	0.095	0.095	0.067	0.066

**Head Shape Regression.** The proposed regression-based correspondence method is also used to study the growth of head shape from structural MRI data obtained from clinical studies spanning the age range from neonate to 5 year old. The 40 cases include 1.5T, T1-weighted MRI scans with resolutions of  $1mm \times 1mm \times 1mm$  and  $0.4mm \times 0.4mm \times 3.6mm$ . The scans are preprocessed and segmented to obtain the head surfaces, which are input to the optimization process. Manually placed landmarks on the bridge of the nose and the openings of the left and right ear canals define a cutting plane and a pair of spheres that we use as constraints, as in Section. 2, to repel the correspondences from the neck, face, and ears, in order to restrict the analysis to the cranium, which is most interesting from a neurological point of view. Figure. 1 shows the particle system distributed across one of the head shapes after optimizing 500 particles.

Head size, measured in volume or circumference is well known to correlate with age. This is confirmed by the linear regression plot (size versus  $\log$  of age) with  $p < 2 \times 10^{-16}$ , shown in Figure. 2. Next, the shapes were preprocessed

using methods mentioned in Section. 2 to remove the effects of size. Changes in head shape along the linear regression line (shape versus  $\log$  of age) are shown in Figure. 3. Note the relative lengthening of the head, and the narrowing at the temples with increasing age. These shape changes are consistent with clinical observations that neonatal brain growth proceeds more rapidly in the forebrain. These results tie head shape to age in the paediatric setting.

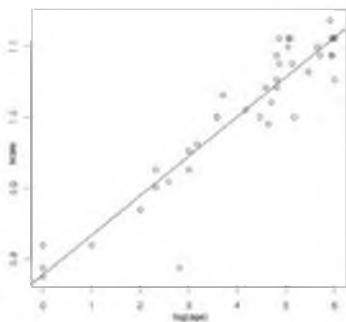


**Fig. 2.** Changes in head size with age

tori (256 particles) and 40 minutes for the head shapes (500 particles). The permutation tests (1000 permutations) were run as parallel processes on a 16-processor machine.

The permutation tests for both the proposed methods for this example showed that none of 1000 permutations gave a better correlation than the input data. While this  $p = 0$  result is not conclusive, it does give strong evidence for significance. Future work will include more permutations to more accurately evaluate the significance.

The experiments were run on a 2GHz processor with run times of approximately 15 minutes for the

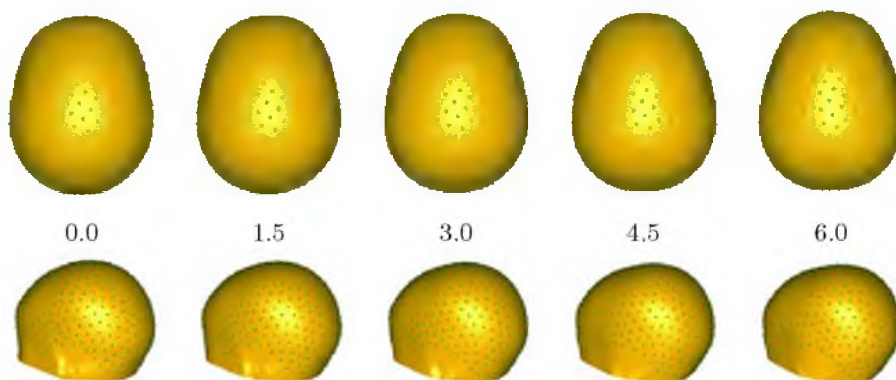


**Fig. 3.** Overview of head shape regression: Changes in head shape with age

## 4 Conclusion

This paper describes a method for *shape regression* that accounts for explanatory variables in the placement of correspondences and allows for open surfaces with arbitrary geometric constraints, and presents a mechanism for hypothesis testing of the role of underlying variables in shape. Results from a study of head shape growth indicate that the proposed method can be applied to quantitative characterization of the relationship between age and head shape in young

children. Such analysis will generate data beyond the currently established standard of head circumference measurements as an index of growth. Moreover, it will generate normative data as a continuous growth model of shape, which can be useful in building optimal MRI head coils for young infants. The continuous shape model could also find use in population studies where two groups are compared with respect to growth trajectory rather than differences at individual time points.

**Acknowledgments.** This work was supported by the NIH/NCRR Center for Integrative Biomedical Computing, P41-RR12553-10 and the NIH/NCBC National Alliance for Medical Image Computing, U54-EB005149. We also acknowledge support from the NIMH Silvio Conte Center for Neuroscience of Mental Disorders MH064065 and the BRP grant R01 NS055754-01-02.

## References

1. Cates, J.E., Fletcher, P.T., Styner, M.A., Shenton, M.E., Whitaker, R.T.: Shape modeling and analysis with entropy-based particle systems. In: Karssemeijer, N., Lelieveldt, B. (eds.) IPMI 2007. LNCS, vol. 4584, pp. 333–345. Springer, Heidelberg (2007)
2. Davies, R., Twining, C., Allen, P., Cootes, T., Taylor, C.: Shape discrimination in the hippocampus using an MDL model. In: Information Processing in Medical Imaging, pp. 38–50 (2003)
3. Gerig, G., Styner, M., Jones, D., Weinberger, D., Leiberman, J.: Shape analysis of brain ventricles using spharm. In: MMBIA, pp. 171–178. IEEE Press, Los Alamitos (2001)
4. Courchesne, E., Karns, C.M., Davis, H.R., Ziccardi, R., Carper, R.A., Tigue, Z.D., Chisum, H.J., Moses, P., Pierce, K.: Unusual brain growth patterns in early life in patients with autistic disorder: An MRI study. *Neurology* 57
5. Knickmeyer, R.C., Gouttard, S., Kang, C., Evans, D., Wilber, K., Smith, K.J., Hamer, R.M., Lin, W., Gerig, G., Gilmore, J.H.: A structural MRI study of human brain development from birth to two years. *J. Neurosci.* 28(47), 12176–12182 (2008)
6. Williams, J., Rossignac, J.: Tightening: curvature-limiting morphological simplification. In: Proc. Ninth ACM Symposium on Solid and Physical Modeling, pp. 107–112 (2005)

**CHAPTER 4**

**MIXED-EFFECTS SHAPE MODELS FOR  
ESTIMATING LONGITUDINAL  
CHANGES IN ANATOMY**

This chapter is a reprint of Proc. STIA, MICCAI, Mixed-Effects Shape Models for Estimating Longitudinal Changes in Anatomy, 2012, pp. 76-87, M Datar, P Muralidharan, A Kumar, S Gouttard, J Piven for the IBIS Network, G Gerig, RT Whitaker, PT Fletcher, with permission of Springer

# Mixed-Effects Shape Models for Estimating Longitudinal Changes in Anatomy

Manasi Datar<sup>1</sup>, Prasanna Muralidharan<sup>1</sup>, Abhishek Kumar<sup>2</sup>,  
Sylvain Gouttard<sup>1</sup>, Joseph Piven<sup>3,\*</sup>, Guido Gerig<sup>1</sup>,  
Ross Whitaker<sup>1</sup>, and P. Thomas Fletcher<sup>1</sup>

<sup>1</sup> Scientific Computing and Imaging Institute, University of Utah

<sup>2</sup> Department of Computer Science, University of Maryland

<sup>3</sup> Carolina Institute for Developmental Disabilities, University of North Carolina

**Abstract.** In this paper, we propose a new method for longitudinal shape analysis that fits a linear mixed-effects model, while simultaneously optimizing correspondences on a set of anatomical shapes. Shape changes are modeled in a hierarchical fashion, with the global population trend as a fixed effect and individual trends as random effects. The statistical significance of the estimated trends are evaluated using specifically designed permutation tests. We also develop a permutation test based on the Hotelling  $T^2$  statistic to compare the average shapes trends between two populations. We demonstrate the benefits of our method on a synthetic example of longitudinal tori and data from a developmental neuroimaging study.

## 1 Introduction

Longitudinal imaging studies involve the collection of imaging data at multiple time points for each participant. Such studies have the potential to provide a rich picture of the anatomical changes occurring during development, disease progression or recovery. Tracking each individual in a longitudinal study gives a model of change with a clarity that cannot be achieved in a cross-sectional study. Further, a more accurate model is possible if each individual in a longitudinal study acts as their own control, that is, factors that vary between individuals remain constant within the same individual. This control over nuisance factors reduces the variance in measurements and results in higher statistical power to quantify change.

---

\* The IBIS Network. Clinical Sites: University of North Carolina: J. Piven (IBIS Network PI), H.C. Hazlett, C. Chappell; University of Washington: S. Dager, A. Estes, D. Shaw; Washington University: K. Botteron, R. McKinstry, J. Constantino, J. Pruett; Childrens Hospital of Philadelphia: R. Schultz, S. Paterson; University of Alberta: L. Zwaigenbaum; Data Coordinating Center: Montreal Neurological Institute: A.C. Evans, D.L. Collins, G.B. Pike, P. Kostopoulos; Samir Das; Image Processing Core: University of Utah: G. Gerig; University of North Carolina: M. Styner; Statistical Analysis Core: University of North Carolina: H. Gu; Genetics Analysis Core: University of North Carolina: P. Sullivan, F. Wright.

Previous work on characterizing anatomical shape changes has focused primarily on the analysis of cross-sectional data. Approaches to the shape regression problem have been formulated for several shape representations or metrics, including diffeomorphic shape changes [1], medial shape representations [2], atlas appearance models [3], deformation tensors [4], and shape regression using particle-based representation in [5]. Work on longitudinal shape modeling includes the use of diffeomorphic mappings and parallel transport by Qiu et al. [6] to track changes in an individual and mapping the individual trends to a population atlas. Durrleman et al. [7] construct spatiotemporal image atlases from longitudinal data. Lorenzi et al. [8] use a hierarchical model on stationary velocity fields, in a framework that does not include a Riemannian metric on the manifold of diffeomorphisms. Fishbaugh et al. [9] estimate smooth growth trajectories as deformations defined through flows with regularized acceleration fields. Barry and Bowman [10] built mixed-effects models on a small number of manually selected landmarks to model the development of facial shape. [11] develop a manifold version of a mixed-effects model to analyze longitudinal data taking values on a Riemannian manifold.

Linear mixed-effects models, pioneered by Laird and Ware [12] have become a natural choice when modeling univariate longitudinal data. These models are hierarchical, characterizing each individual trend as a linear model, which in turn can be modeled as a perturbation of the overall population trend. While these models are powerful for analyzing univariate or low-dimensional multivariate data, little has been done in the high-dimensional setting, such as longitudinal data extracted from medical images. A major bottleneck is the difficulty of estimating the large number of parameters involved in covariances between random effects.

In this paper, we present a new method for characterizing longitudinal shape change that combines point correspondences across shapes with the statistical modeling of individual and population trends via the linear mixed-effects model. Our shape models are based on the particle correspondence framework introduced by Cates et al [13], wherein, particle positions on the object surfaces are optimized in a variational framework that seeks a balance between model simplicity and geometric accuracy of the surface representations.

## 2 Background

In the following section we provide a brief overview the particle-system correspondence optimization method as proposed in [13]. The general strategy of this method is to represent correspondences as point sets that are distributed across an ensemble of similar shapes by minimizing an objective function that quantifies the entropy of the system. We also review the linear mixed-effects model, described by Laird and Ware [12], and used as the underlying statistical descriptor of longitudinal changes in our system.

### 2.1 Correspondence Optimization

Let us define a surface as a smooth, closed manifold of codimension one, which is a subset of  $\mathbb{R}^d$  (e.g.,  $d = 3$  for volumes). We sample the surface  $\mathcal{S} \subset \mathbb{R}^d$

using a discrete set of  $N$  points that are considered as random variables  $\mathbf{S} = (\mathbf{Y}_1, \mathbf{Y}_2, \dots, \mathbf{Y}_N)^T$ ,  $\mathbf{Y} \in \mathbb{R}^d$  drawn from a probability density function (PDF),  $p(\mathbf{Y})$ . We denote a realization of this PDF with lower case, and thus we have  $\mathbf{s} = (\mathbf{y}_1, \mathbf{y}_2, \dots, \mathbf{y}_N)^T$ , where  $\mathbf{s} \in \mathcal{S}^N$ . We refer to the positions  $\mathbf{y}$  as *particles*, and a set of particles, a *particle system*.

The amount of information encoded in this random sampling is, in the limit, the differential entropy of the PDF, given by  $H[\mathbf{Y}] = -E\{\log p(\mathbf{Y})\}$ , where  $E\{\cdot\}$  is the expectation. Approximating the expectation by the sample mean, we have  $H[\mathbf{Y}] \approx -\frac{1}{Nd} \sum_i \log p(\mathbf{y}_i)$ . To determine the probability of a particle's position,  $p(\mathbf{y}_i)$ , [13] uses a nonparametric Parzen-window density estimation given by a mixture of multivariate, isotropic Gaussian kernels with standard deviation  $\sigma$  that determines the strength of particle interaction with  $N$  neighbouring particles within the defined window. An ensemble comprised of  $M$  surfaces,  $\mathcal{E} = \mathbf{s}^1, \dots, \mathbf{s}^M$  can be described by a  $Nd \times M$  matrix of particle positions  $P = (\mathbf{y}_j^k)$ , where  $k = 1, \dots, M$  and  $j = 1, \dots, N$ . Let  $\mathbf{s}^k \in \mathbb{R}^{Nd}$  be an instance of a random variable  $\mathbf{S}$ , then, the combined ensemble and shape cost function is defined by

$$Q = H(\mathbf{S}) - \sum_k H(P^k) \quad (1)$$

This cost function is composed of two interacting terms. The first term produces a compact distribution of samples in shape space, while the second term provides uniformly-distributed correspondence positions on the shape surfaces, to achieve a faithful shape representation. The optimization process of this cost function is defined via gradient descent as described in [13].

## 2.2 The Laird and Ware Linear Mixed-Effects Model

In a linear mixed-effects model, the response or observed variable  $y_i$  is assumed to have a set of parameters  $\alpha$ , fixed across individuals. In addition, each individual  $i$ , is assigned a set of random parameters  $b_i$  that model the deviation from the fixed effect  $\alpha$ . For  $i \in \{1, 2, \dots, m\}$ , the model reads as follows:

$$y_i = X_i\alpha + Z_i b_i + \epsilon_i, \quad (2)$$

where for the  $i^{\text{th}}$  individual,  $X_i$  and  $Z_i$  are known independent variables which influence  $y_i$  through fixed and random effects respectively.  $b_i$  are distributed as  $N(0, D)$ ,  $D$  being an arbitrary covariance matrix.  $\epsilon_i$  models the error from the observed data, and is distributed as  $N(0, \sigma^2 I_i)$ ,  $I_i$  being an identity matrix.

A simple case of the mixed-effects model occurs when we have a single independent variable (such as time or age) that is used for both fixed and random effects. In this case we have  $Z_i = X_i$  and (2) simply reduces to

$$y_i = X_i(\alpha + b_i) + \epsilon_i, \quad (3)$$

where for the  $i^{\text{th}}$  individual,  $\alpha$  and  $b_i$  are 2-vectors interpreted as slope-intercept pairs of the group and random effects of the individual, respectively.

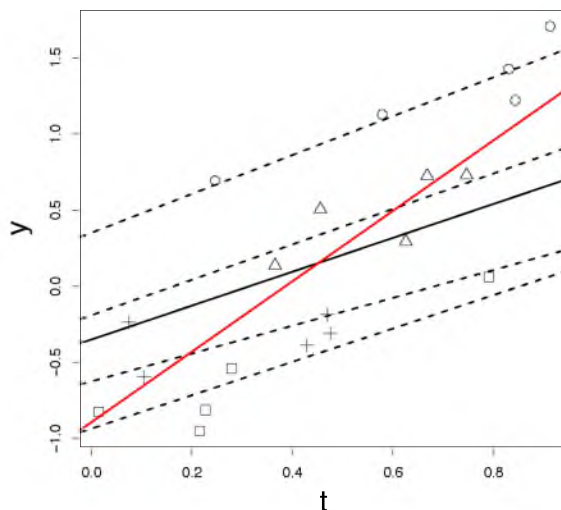


**Fig. 1.** Example of randomly-generated, synthetic longitudinal data. Data points for each “individual” are displayed with different symbols. The estimated mixed-effects model is shown with both the fixed effects, i.e., group trend (solid black line), and random effects, i.e., individual trends (dashed lines). The estimated linear regression model, which ignores correlations within individuals, is shown as a red line.

An example of synthetically generated data from the model (3) is shown in Fig. 1. This example illustrates the power of mixed-effects models and the importance of modeling correlations within each individual. Ignoring these correlations leaves us with a simple linear regression model. Fig. 1 shows the estimated linear regression model, which does not concur with the trends of the individuals. In contrast, the estimated  $\alpha$  from mixed-effects modeling optimally summarizes the overall group trend.

### 3 Methodology

The correspondence optimization framework described in Sec. 2.1 was extended to incorporate a linear regression based approach in [5]. However, this approach may not model longitudinal data correctly due to differences in relationships across individuals. To address this issue, we propose a method that incorporates the linear mixed-effects model described in Sec. 2.2 into the framework in Sec. 2.1. Parameters of the linear mixed-effects model are simultaneously estimated along with the correspondence optimization. The following section describes our approach and revisits the parameter estimation for the linear mixed-effects model given by [12].

### 3.1 Correspondence with Linear Mixed-Effects Modeling of Shapes

With the assumption of a Gaussian distribution in shape space, we can introduce a generative statistical model.

$$\mathbf{y} = \boldsymbol{\mu} + \boldsymbol{\epsilon}, \boldsymbol{\epsilon} \sim \mathcal{N}(\mathbf{0}, \boldsymbol{\Sigma}) \quad (4)$$

for correspondences, where  $\boldsymbol{\mu}$  is the vector of mean correspondences, and  $\boldsymbol{\epsilon}$  is normally-distributed error. Replacing  $\boldsymbol{\mu}$  in this model with a function of an explanatory variable  $x$  gives the more general, *regression* model

$$\mathbf{y} = f(x) + \hat{\boldsymbol{\epsilon}}, \hat{\boldsymbol{\epsilon}} \sim \mathcal{N}(\mathbf{0}, \hat{\boldsymbol{\Sigma}}). \quad (5)$$

We propose to optimize correspondences under the linear mixed-effects model described in Sec. 2.2 to facilitate the estimation of individual and population trends in longitudinal data. Using the same explanatory variable (age of the individual, in case of real data) for both fixed and random effects as in (3), we assume that correspondences for shapes belonging to individual  $i$  are generated by the following analogous statistical model:

$$Y_i = X_i \alpha + X_i b_i + \epsilon_i, \quad (6)$$

where  $X_i$  represents the explanatory variable (age; in the case of real data),  $Y_i$  is the matrix containing correspondences for *all* shapes in the population,  $\alpha$  represents the fixed-effects parameters (slope, intercept), while  $b_i$  represents the random-effects parameters (slope, intercept) for the individual  $i$  and  $\epsilon_i$  represents the error in correspondences.

The algorithm proceeds as follows. (a) Correspondences are first optimized under the nonregression model (4) to minimize the entropy associated with the total error  $\boldsymbol{\epsilon}$ , and are used to compute an initial estimate of the linear mixed-effects model parameters. (b) We then follow the optimization procedure as described in Sec. 2.1, with the replacement of the model covariance  $\boldsymbol{\Sigma}$  by the covariance  $\hat{\boldsymbol{\Sigma}}$  of the underlying residual relative to the regression model. (c) We interleave the two estimation problems, re-estimating the mixed-effects model parameters after each iteration of the gradient descent on the correspondences.

### 3.2 Estimation of Parameters

We denote the parameters in the covariance matrix  $D$  and  $\sigma^2$  by a vector  $\boldsymbol{\theta}$ . We compute maximum likelihood (ML) estimates for  $\alpha$  and  $\boldsymbol{\theta}$  and empirical Bayes estimates for  $b_i$ . If we were to be able to observe  $b_i$  and  $\epsilon_i$ , we could compute closed-form ML estimates of  $\alpha$  and  $\boldsymbol{\theta}$ , but this is not the case. Therefore, an expectation maximization (EM) algorithm is used to estimate  $\alpha$  and  $\boldsymbol{\theta}$ , treating  $b_i$  and  $\epsilon_i$  as hidden variables. The EM algorithm guarantees that the likelihood increases or stays constant at each iteration, but it can converge to a local maximum instead of the global one.

We model the response variable  $y_i$  in (2) as being marginally distributed as  $N(\alpha, \sigma^2 I_i + Z_i D Z_i^T)$ . Since we don't observe  $b_i$  and  $\epsilon_i$ , let us replace  $\sigma^2$  and  $D$  by their current estimates  $\hat{\sigma}^{2(j)}$  and  $\hat{D}^{(j)}$  at iteration  $j$  of the EM algorithm. Let

us also define  $r_i^{(j)} := y_i - X_i \hat{\alpha}^{(j)}$ , and  $N := \sum_{i=1}^m n_i$ . The ML estimate for  $\alpha$  is given by

$$\hat{\alpha}^{(j)} = \left( \sum_{i=1}^m X_i^T W_i^{(j)} X_i \right)^{-1} \sum_{i=1}^m X_i^T W_i^{(j)} y_i,$$

where  $W_i^{(j)} = \left( \hat{\sigma}^{2(j)} I_i + Z_i \hat{D}^{(j)} Z_i^T \right)^{-1}$ .

The random-effects,  $b_i$ , are estimated using empirical Bayes as

$$\hat{b}_i^{(j)} = E \left[ b_i | y_i, \hat{\alpha}^{(j)}, \hat{\theta}^{(j)} \right] = \hat{D}^{(j)} Z_i^T W_i^{(j)} r_i^{(j)}$$

The covariances  $\sigma^2$  and  $D$  are estimated by taking the expectation over hidden variables  $\epsilon_i$  and  $b_i$ , conditioned on  $y_i$  and the current estimates of  $\alpha$  and  $\theta$ . This step combines both the estimation and a maximization. The resulting estimate for the error variance is

$$\begin{aligned} \hat{\sigma}^{2(j+1)} &= \frac{1}{N} E \left\{ \sum_{i=1}^m \epsilon_i^T \epsilon_i | y_i, \hat{\alpha}^{(j)}, \hat{\theta}^{(j)} \right\} \\ &= \frac{1}{N} \sum_{i=1}^m \left[ \hat{e}_i^T \hat{e}_i + \text{tr} \text{Var} \left\{ \epsilon_i | y_i, \hat{\alpha}^{(j)}, \hat{\theta}^{(j)} \right\} \right] \\ &= \frac{1}{N} \sum_{i=1}^m \left[ \hat{e}_i^T \hat{e}_i + \hat{\sigma}^{2(j)} \text{tr} \left( I_i - \hat{\sigma}^{2(j)} W_i^{(j)} \right) \right], \end{aligned}$$

where  $\hat{e}_i = E[\epsilon_i | y_i, \hat{\alpha}^{(j)}, \hat{\theta}^{(j)}] = r_i^{(j)} - Z_i \hat{b}_i^{(j)}$ . Similarly, the estimate for covariance matrix  $D$  is given by

$$\begin{aligned} \hat{D}^{(j)} &= \frac{1}{m} E \left[ \sum_{i=1}^m b_i b_i^T | y_i, \hat{\alpha}^{(j)}, \hat{\theta}^{(j)} \right] \\ &= \frac{1}{m} \sum_{i=1}^m \hat{b}_i^{(j)} \hat{b}_i^{(j)T} + \hat{D}^{(j)} (I - Z_i W_i^{(j)} Z_i \hat{D}^{(j)}). \end{aligned}$$

We initialize the covariance matrix  $\hat{D}^{(0)}$  to the identity matrix and  $\hat{\sigma}^{2(0)}$  to 1 before starting the EM iterations.

### 3.3 Permutation Test for Significance of Random-Effects

In the case of longitudinal data, correlations may exist within shapes at different time-points for a given individual and break the independence assumption of the simple linear regression model. Another assumption that can be broken is *homoscedasticity*, i.e., the property that the variance of the residuals is constant across the independent parameter. When these assumptions are not met, simple

linear regression models give less reliable (i.e., higher variance) estimates of the  $\alpha$  parameters.

We use a nonparametric permutation test based on an estimate of the error variance  $V_\epsilon$  to confirm the significance of the random-effects introduced in the mixed-effects model. This permutation test works by permuting the assignment of shapes to individuals. The explanatory variable for the shape is not permuted - only “group memberships” are permuted. For every permutation, we can compute the squared norm of the residual vector for each shape, and use the average value as an estimate of  $V_\epsilon$  in fitting the linear mixed-effects model to this permuted ensemble of shapes. This allows us to compute a distribution of  $V_\epsilon$  of the model as a test statistic and test the null hypothesis that random-effects have no effect on the final parameter estimates of the model, and consequently lead to unaltered  $V_\epsilon$  values across permutations. Then comparing our unpermuted  $V_\epsilon$  to this distribution, we can compute a  $p$ -value to test the null hypothesis. We perform the correspondence optimization on *each* permutation separately, and thus *the results of our permutation test are not biased by the correspondence optimization method.*

### 3.4 Permutation Test for Group Discrimination

One of the major motivations of longitudinal data analysis is to test if changes observed in one group differ from those found in another. For instance, one might ask if the brain anatomy of Alzheimer’s patients deteriorates faster than those of healthily aging subjects. In this section, we develop a permutation test on the Hotelling  $T^2$  statistic to test the statistical significance of group-parameter differences between two groups of longitudinal data.

Recall the Hotelling  $T^2$  statistic is a test statistic often used in a multivariate test of the difference between sample means,  $\bar{p}, \bar{q}$ , of two groups of data  $\{p_1, \dots, p_m\}$  and  $\{q_1, \dots, q_n\}$ , with all  $p_i, q_i \in \mathbb{R}^d$ . The idea is to compare the difference between the two means, relative to the pooled sample covariance:

$$W = \frac{\sum_i (p_i - \bar{p})(p_i - \bar{p})^T + \sum_i (q_i - \bar{q})(q_i - \bar{q})^T}{m + n - 2}.$$

The  $T^2$  statistic can be thought of as a squared Mahalanobis distance between the means, using this pooled covariance,  $W$ . The sample  $T^2$  statistic is given by

$$t^2 = \frac{mn}{m+n} (\bar{p} - \bar{q})^T W^{-1} (\bar{p} - \bar{q}) \quad (7)$$

The permutation test procedure is as follows: (a) compute the  $t^2$  statistic, (b) randomly permute (swap) data points between the  $p$  and  $q$  groups, computing a  $t_k^2$  statistic for the permuted groups, (c) repeat step 2 for  $k = 1, \dots, P$ , (d) compute the  $p$ -value:  $p = B/(P+1)$ , where  $B$  is the number of  $t_k^2 < t^2$ . The final  $p$ -value can be interpreted as the probability of finding a larger group difference by random chance under the null hypothesis (that there is no difference between the means).

Consider the specific problem of comparing the mean trends in two different groups  $G$  and  $H$ . Let  $Y_{ij}^{(G)}$  and  $Y_{ij}^{(H)}$  be two sets of longitudinal data and the resulting parameter estimates for the two groups to be  $(\hat{\alpha}_1^G, \hat{\alpha}_2^G)$  and  $(\hat{\alpha}_1^H, \hat{\alpha}_2^H)$ . It is often most interesting to separate the tests of the slope parameter  $\alpha_1$  and the intercept parameter  $\alpha_2$ . For example, in testing the differences in anatomical changes between a healthy and disease group, it is important to distinguish if the shape differences are present at baseline (intercept) or if they develop over time (slope). To make this distinction, we can separate the above Hotelling  $T^2$  test into these two components. We will thus look at the two separated statistics,  $t_{\alpha_1}^2$  and  $t_{\alpha_2}^2$  given by (7).

## 4 Results and Discussion

We validate the proposed method through experiments on synthetic longitudinal tori, and test the significance of our estimated parameters via a nonparametric permutation test. We present applications of the method in longitudinal studies of early development of brain shapes from a neuroimaging study.

### 4.1 Synthetic Tori

*Test of model significance.* We generated longitudinal tori comprising of 11 “individuals”, at 3 different time points. The two radii of the tori within a group are generated according to the mixed-effects model in (6).

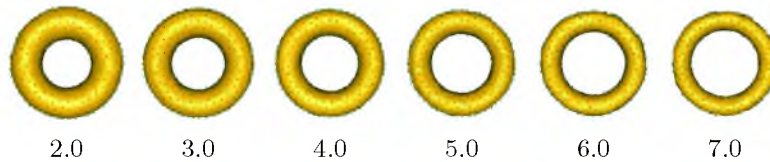


**Fig. 2.** Visualizing fixed effects on the synthetic data

For each individual  $i$ ,  $X_i \sim \mathcal{U}(2, 10)$  drawn independently, random-effects  $b_i \sim \mathcal{N}(0, 0.4)$ , and errors  $\epsilon_i \sim \mathcal{N}(0, 0.3)$ . The slope-intercept pair for the fixed-effects are given as:  $(\alpha_{1R}, \alpha_{2R}) = (2, 30)$  and  $(\alpha_{1r}, \alpha_{2r}) = (-1, 15)$ , where  $R, r$  are the outer and inner radii respectively. The particle correspondence positions and model parameters can then be estimated as prescribed in Section 3. Figure 2 shows the change in shape obtained using the fixed-effects of particle positions. The parameter  $R$ , increases whereas  $r$  decreases, which is consistent with the slope parameters used in the generative model.

We evaluate the significance of the  $b_i$  parameters using the nonparametric permutation test described in Sec. 3.3. Each of the 11 groups are assigned 3 random shapes from the total pool without repetition. We generate 500 such permutations and estimate  $V_\epsilon(P)$ , for each permutation  $P$ . Over these permutations,  $V_\epsilon(P)$

ranges from 2500 to 6500.  $V_\epsilon$  for unpermuted group memberships is 940. This implies a  $p$ -value  $\sim 0$ . If it was possible to explain the population by only using fixed-effects, the permutation of group memberships should not have affected  $V_\epsilon$  values significantly. This test shows that using random-effects gives significant reduction in  $V_\epsilon$  independent of the increase in the number of model parameters.

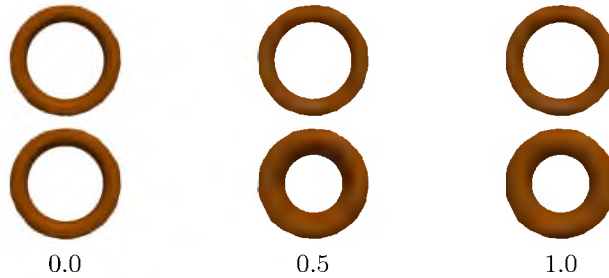


**Fig. 3.** Visualizing the trends in the two groups created to test group differences: constant trend (top), trend with increasing  $r$  (bottom)

*Test for group differences.* Here, we generate two groups of 11 “individuals” each, with 3 time-points per individual, with  $X_i$  for each individual at 0, 0.5, 1, random effects  $b_i \sim \mathcal{N}(0, 0.3)$ , and errors  $\epsilon_i \sim \mathcal{N}(0, 0.1)$ . For one of the groups, the fixed-effect slope is kept at zero, but for the other the  $r$  fixed-effect is given a slope 3. Figure 3 shows the tori generated using this configuration of parameters. When looking for group differences based on baseline intercepts, as expected, the permutation test prescribed in Section 3.4 did not yield a significant  $p$ -value. But when comparing groups based on the slope parameter, we obtained a  $p$ -value  $\sim 0$ , which confirms a stark difference in group trends.

## 4.2 Mixed-Effects Model for Brain Structures

*Test for model significance and trend variation.* In this experiment, we work with brain structures from a developmental neuroimaging study. We have 11 subjects scanned at approximately (6, 12, 24) months. The scans are preprocessed and segmented to obtain the brain structures (cerebellum, left and right hemispheres) which are input to the optimization process.

The fixed effects in Fig. 4 clearly show two changes happening in the infant brain. The first is an elongation of both hemispheres, which can be seen as a stretching of the frontal lobe and narrowing of the hemisphere shapes. The second effect is the growth near the top of the cerebellum. These trends are qualitatively consistent with the cross-sectional results found in [5].

The longitudinal model can tell us more, however, than a regression model of cross-sectional data. First, we know that these fixed effects are representative of the growth trend that individuals undergo on average, rather than a trend seen between multiple subjects. Second, and more interestingly, we can say something



**Fig. 4.** Visualizing the fixed-effects of brain structures (blue denotes expansion, and yellow denotes contraction)



**Fig. 5.** Visualizing the random-effects of brain structures (red denotes high variance regions)

about the variability of these trends in the population. Fig. 5 encodes the variance of the random slopes at each point and is indicative of regions where the variation in the growth trend across individuals is high (red regions in Fig. 5). An example inference is that the elongating frontal lobe and expanding cerebellum are relatively stable across the sample (i.e. the variance of these trends is low). We also evaluate the significance of the  $b_i$  using the nonparametric permutation test described in Sec. 3.3. Group memberships are permuted 500 times and  $V_\epsilon(P)$  is estimated for each permutation  $P$ . While  $V_\epsilon(P)$  ranges from 10000 to 17000 for the permuted sets, the value for the unpermuted set is 5400. This suggests a  $p$ -value  $\sim 0$  and implies that the random effects play a significant role in describing the early development of the brain.

*Test for differences in group trends.* We also evaluate our method using a longitudinal database from an Autism Center of Excellence, part of the Infant Brain Imaging Study (IBIS). The study consists of high-risk infants as well as controls, scanned at approximately (6, 12, 24) months. At 24 months, symptoms of autism spectrum disorder (ASD) were measured using the Autism Diagnostic Observation Schedule (ADOS). A positive ADOS score indicates the child has a high probability of later being diagnosed with autism. Finally, we have two groups: 15 high-risk subjects with positive ADOS (HR+) and 14 low-risk subjects with negative ADOS (LR-).

Fig. 6 visualizes the group trends for the HR+ and LR- groups and clarifies that the global trends are similar across both groups. There are localized

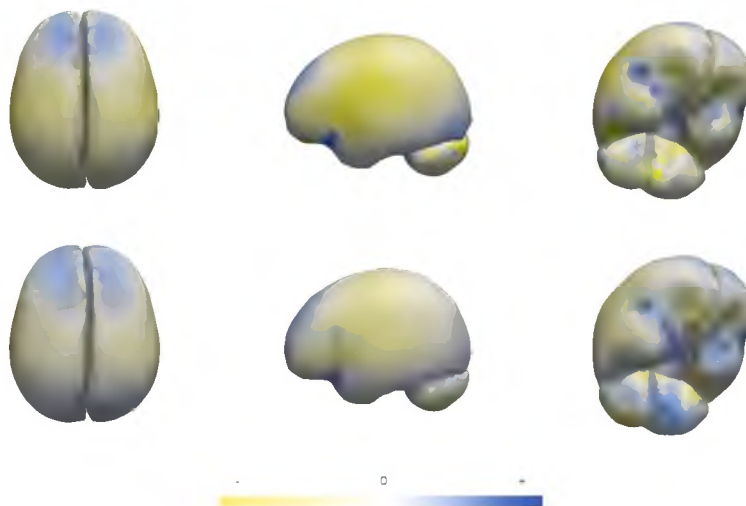


**Fig. 6.** Variation in group trends for the HR+ (top) and LR- (bottom) groups (yellow denotes contraction, blue denotes expansion)

differences near the frontal end of the hemispheres and also near the cerebellum, but these are not found to be significant by the permutation test for group differences. The  $t^2$  statistic for differences in group trends in cerebellum, left hemisphere and right hemisphere independently were 6.1039, 5.155 and 4.5693 respectively. The  $p$ -values were 0.112, 0.454 and 0.515 for the same.

## 5 Conclusion and Future Work

We presented a new mixed-effects shape model for analyzing longitudinal shape changes, which is based on a particle system representation and entropy minimization framework for point correspondences. We demonstrated the ability of the model to characterize both group-level and individual-level shape trends on synthetic data and developmental brain data. As for future work, the current work does not handle spatial correlations between points on a shape. We plan to investigate this issue, possibly using a pseudolikelihood estimation of the covariance matrix of the shape parameters, similar to [10]. Such an estimation could possibly take advantage of the entropy minimization, as this tends to decrease the dimensionality of the covariance matrix.

**Acknowledgements.** This work was supported by NSF CAREER Award 1054057, the NIH/NCRR Center for Integrative Biomedical Computing, P41-RR12553-10, and the NIH/NCBC National Alliance for Medical Image Computing, U54-EB005149. We also acknowledge support from the NIMH Silvio Conte Center for Neuroscience of Mental Disorders MH064065, BRP grant R01 NS055754-01-02 and the NIH grant RO1 HD055741 (ACE, project IBIS).

## References

1. Davis, B., Fletcher, P., Bullitt, E., Joshi, S.: Population shape regression from random design data. In: ICCV (2007)
2. Shi, X., Styner, M., Lieberman, J., Ibrahim, J.G., Lin, W., Zhu, H.: Intrinsic Regression Models for Manifold-Valued Data. In: Yang, G.-Z., Hawkes, D., Rueckert, D., Noble, A., Taylor, C. (eds.) MICCAI 2009, Part II. LNCS, vol. 5762, pp. 192–199. Springer, Heidelberg (2009)
3. Rohlfing, T., Sullivan, E.V., Pfefferbaum, A.: Regression Models of Atlas Appearance. In: Prince, J.L., Pham, D.L., Myers, K.J. (eds.) IPMI 2009. LNCS, vol. 5636, pp. 151–162. Springer, Heidelberg (2009)
4. Thompson, P.M., Giedd, J.N., Woods, R.P., MacDonald, D., Evans, A.C., Toga, A.W.: Growth patterns in the developing brain detected by using continuum mechanical tensor maps. *Nature* 404, 190–193
5. Datar, M., Cates, J., Fletcher, P.T., Gouttard, S., Gerig, G., Whitaker, R.: Particle Based Shape Regression of Open Surfaces with Applications to Developmental Neuroimaging. In: Yang, G.-Z., Hawkes, D., Rueckert, D., Noble, A., Taylor, C. (eds.) MICCAI 2009, Part II. LNCS, vol. 5762, pp. 167–174. Springer, Heidelberg (2009)
6. Qiu, A., Albert, M., Younes, L., Miller, M.I.: Time sequence diffeomorphic metric mapping and parallel transport track time-dependent shape changes. *NeuroImage* 45(1), S51–S60 (2009)
7. Durrleman, S., Pennec, X., Trouvé, A., Gerig, G., Ayache, N.: Spatiotemporal Atlas Estimation for Developmental Delay Detection in Longitudinal Datasets. In: Yang, G.-Z., Hawkes, D., Rueckert, D., Noble, A., Taylor, C. (eds.) MICCAI 2009, Part I. LNCS, vol. 5761, pp. 297–304. Springer, Heidelberg (2009)
8. Lorenzi, M., Ayache, N., Frisoni, G.B., Pennec, X., The Alzheimer’s Disease Neuroimaging Initiative: Mapping the Effects of  $A\beta_{1-42}$  Levels on the Longitudinal Changes in Healthy Aging: Hierarchical Modeling Based on Stationary Velocity Fields. In: Fichtinger, G., Martel, A., Peters, T. (eds.) MICCAI 2011, Part II. LNCS, vol. 6892, pp. 663–670. Springer, Heidelberg (2011)
9. Fishbaugh, J., Durrleman, S., Gerig, G.: Estimation of Smooth Growth Trajectories with Controlled Acceleration from Time Series Shape Data. In: Fichtinger, G., Martel, A., Peters, T. (eds.) MICCAI 2011, Part II. LNCS, vol. 6892, pp. 401–408. Springer, Heidelberg (2011)
10. Barry, S.J.E., Bowman, A.W.: Linear mixed models for longitudinal shape data with applications to facial modeling. *Biostatistics* 9(3), 555–565
11. Muralidharan, P., Fletcher, P.T.: Sasaki metrics for the analysis of longitudinal data on manifolds. In: IEEE Conference on Computer Vision and Pattern Recognition, CVPR (to appear, 2012)
12. Laird, N., Ware, J.H.: Random-effects models for longitudinal data. *Biometrics* 38(4), 963–974 (1982)
13. Cates, J.E., Fletcher, P.T., Styner, M.A., Shenton, M.E., Whitaker, R.T.: Shape Modeling and Analysis with Entropy-Based Particle Systems. In: Karssemeijer, N., Lelieveldt, B. (eds.) IPMI 2007. LNCS, vol. 4584, pp. 333–345. Springer, Heidelberg (2007)

**CHAPTER 5**

**GEOMETRIC CORRESPONDENCE FOR  
ENSEMBLES OF NONREGULAR  
SHAPES**

This chapter is a reprint of Proc. MICCAI, Geometric Correspondence for Ensembles of Nonregular Shapes, vol. 2, 2011, pp. 368-375, M Datar, Y Gur, B Paniagua, MA Styner, RT Whitaker, with permission of Springer

# Geometric Correspondence for Ensembles of Nonregular Shapes

Manasi Datar<sup>1</sup>, Yaniv Gur<sup>1</sup>, Beatriz Paniagua<sup>2</sup>,  
Martin Styner<sup>2</sup>, and Ross Whitaker<sup>1</sup>

<sup>1</sup> Scientific Computing and Imaging Institute, University of Utah, USA

<sup>2</sup> University of North Carolina at Chapel Hill, USA

**Abstract.** An ensemble of biological shapes can be represented and analyzed with a dense set of point correspondences. In previous work, optimal point placement was determined by optimizing an information theoretic criterion that depends on relative spatial locations on different shapes combined with pairwise Euclidean distances between nearby points on the same shape. These choices have prevented such methods from effectively characterizing shapes with complex geometry such as thin or highly curved features. This paper extends previous methods for automatic shape correspondence by taking into account the underlying geometry of individual shapes. This is done by replacing the Euclidean distance for intrashape pairwise particle interactions by the geodesic distance. A novel set of numerical techniques for fast distance computations on curved surfaces is used to extract these distances. In addition, we introduce an intershape penalty term that incorporates surface normal information to achieve better particle correspondences near sharp features. Finally, we demonstrate this new method on synthetic and biological datasets.

## 1 Introduction

A well established method for performing statistics on an ensemble of shapes is to compare configurations of corresponding landmarks placed on the individual shapes. In recent years, several methods have proposed an automatic placement of landmarks in a way that captures statistical properties of an ensemble [1,2]. The method of Cates et al [1] uses a formulation of ensemble entropy to deploy a dense set of landmarks, or *particles*, which assign correspondences between shapes within a population. The positions of the particles on the shape surfaces are optimized using a variational framework that tries to find a balance between model simplicity via minimum entropy, and geometric accuracy of the surface representation. However, medical or biological objects shapes are often composed of sharp features and regions of high curvature. In such cases, nearby particles in the ambient space may be separated by a large distance on the object's surface (see Fig. 1). Thus, the Euclidean distance measure cannot capture correctly the underlying local geometry and prevents the method from producing a faithful shape representation. This limitation reflects a failure of Euclidean distance



**Fig. 1.** Points near sharp features (left) are not able to achieve good distributions with Euclidean distance, because they do not lie in the same tangent space, which is necessary for movement that is constrained to the surfaces. Points may be nearby and interact (center) even though they sample very different parts of the surface. Points on nearby features (right) on different shapes (blue and green) can come into incorrect correspondence if the system considers only distance.

to account for the intrinsic distances between points on the surface, suggesting geodesic distance as a better choice. However, geodesic distances are generally not computable in closed form, and interparticle interactions are part of the inner loop of an interactive optimization process. Thus, the computational burden of geodesics are prohibitive. This paper makes several contributions that enable better modeling of ensembles composed of shapes with a complex geometric structure. First, we incorporate geodesic distance measures into the framework proposed by Cates, et al [1]. While accurate geodesic distance computation is unwieldy for implicit surfaces, very fast methods exist to compute geodesic distances between vertices of 3D mesh representations of shapes. Thus, we propose precomputing all pairwise distances on a somewhat fine 3D mesh of an input surface and interpolate, as required, in the process of optimizing intrashape particle interactions. To address mismatches of correspondences on highly curved features across different shapes, we introduce an intershape penalty that accounts for the behavior of normals on highly curved geometry. Hence, the second contribution of our paper is to integrate this intershape penalty term into the variational framework for model optimization given in [1] to improve particle correspondences near sharp features. As a final contribution we demonstrate the use of a correspondence-based method for the analysis of highly curved (or nonregular) shapes—the left ventricle myocardium of the human heart—which has, so far not feasible with point correspondences.

## 2 Background

In the following section we provide a brief overview the particle-system correspondence optimization method as proposed in [1]. The general strategy of this method is to represent correspondences as point sets that are distributed across an ensemble of similar shapes by minimizing an objective function that quantifies the entropy of the system. We also describe an efficient, fine-grained algorithm for solving the eikonal equation on triangular meshes, as proposed by Fu et al [3]

**Correspondence Optimization.** Let us define a surface as a smooth, closed manifold of codimension one, which is a subset of  $\mathbb{R}^d$  (e.g.,  $d = 3$  for volumes). We sample the surface  $\mathcal{S} \subset \mathbb{R}^d$  using a discrete set of  $N$  points that are considered as random variables  $\mathbf{Z} = (\mathbf{X}_1, \mathbf{X}_2, \dots, \mathbf{X}_N)^T$ ,  $\mathbf{X} \in \mathbb{R}^d$  drawn from a probability density function (PDF),  $p(\mathbf{X})$ . We denote a realization of this PDF with lower case, and thus we have  $\mathbf{z} = (\mathbf{x}_1, \mathbf{x}_2, \dots, \mathbf{x}_N)^T$ , where  $\mathbf{z} \in \mathcal{S}^N$ . We refer to the positions  $\mathbf{x}$  as *particles*, and to a set of particles as a *particle system*. The amount of information encoded in this random sampling is, in the limit, the differential entropy of the PDF, given by  $H[\mathbf{X}] = -E\{\log p(\mathbf{X})\}$ , where  $E\{\cdot\}$  is the expectation. Approximating the expectation by the sample mean, we have  $H[\mathbf{X}] \approx -\frac{1}{Nd} \sum_i \log p(\mathbf{x}_i)$ . To determine the probability of a particle's position,  $p(\mathbf{x}_i)$ , [1] uses a nonparametric Parzen-window density estimation given by a mixture of multivariate, isotropic Gaussian kernels with standard deviation  $\sigma$  that determines the strength of particles interaction with  $N$  neighbouring particles within the defined window. An ensemble comprised of  $M$  surfaces,  $\mathcal{E} = \mathbf{z}^1, \dots, \mathbf{z}^M$  can be described by a  $Nd \times M$  matrix of particle positions  $P = (\mathbf{x}_j^k)$ , where  $k = 1, \dots, M$  and  $j = 1, \dots, N$ . Let  $\mathbf{z}^k \in \mathbb{R}^{Nd}$  be an instance of a random variable  $\mathbf{Z}$ , then, the combined ensemble and shape cost function is defined by

$$Q = H(\mathbf{Z}) - \sum_k H(P^k) \quad (1)$$

This cost function is composed of two interacting terms. The first term produces a compact distribution of samples in shape space, while the second term provides uniformly-distributed correspondence positions on the shape surfaces, to achieve a faithful shape representation. The optimization process of this cost function is defined via gradient descent as described in [1].

**Fast Geodesic Distance Computation.** The use of Euclidean distance between particles in the Parzen-window density estimation in [1] requires that nearby particles interact in the local tangent plane of the surface. However, it is not the case for thin structures with high curvature, such as the one illustrated in Fig. 1 (left). To address this, we replace the Euclidean distance in the kernel by the *geodesic* interparticle distance. However, this modification demands a large number of pairwise geodesic distance computations. Such computations are not feasible without the recent developments in fast, parallel algorithms for solving hyperbolic partial differential equations (PDEs) as well as extremely fast SIMD hardware in the form of graphics processors (GPUs). The distance between each point  $a$  on the surface and every other point, is given by the solution to the eikonal equation  $|\nabla u| = 1$ , as discussed in [4], using the boundary condition  $u(a) = 0$ . The computation of distances to many thousands of points on large ensembles of shapes is feasible only if the eikonal equation can be solved in a small fraction of a second. The fast iterative method (FIM) [4] for regular grids is not worst-case optimal, but is extremely efficient on parallel, SIMD architectures, such as GPUs. Here, we use an extension of the FIM for triangular meshes [3]. This algorithm computes, for instance, distances between nodes on a mesh with thousands of vertices in less than 30 seconds on a GPU.

### 3 Methodology

The input to the shape correspondence system is a collection of implicitly defined surfaces. For this paper, the input surfaces are binary segmentations, and we use the preprocessing, initialization, and particle optimization pipeline described in [1]. Here we describe the integration of the geodesic distance for inter-particle interactions and the surface normal based penalty term for intershape correspondence into the framework described in Sec. 2.

**Particle Position Optimization using Geodesic Distances.** A triangulation of each input surface is generated using the algorithm described in [5]. An example triangulation is shown in Fig. 2(a) along with the corresponding synthetic shape. The numerical technique for fast distance computation on 3D triangulated surfaces described at the end of Sec. 2 is then used to precompute geodesic distances between each vertex and all other vertices within a prescribed distance,  $d_{\max}$ . The parameter  $d_{\max}$  is chosen to coincide with the limited range of influence of the Gaussian kernels that control the range of influence of each particle. This truncation results in a sparse, symmetric matrix of geodesic distances. The entries in this matrix are then converted into a fixed point format and stored using a List of Lists (LIL) representation for efficient memory usage and fast access. We call this matrix  $M_G$  such that  $D_G(v_1, v_2) = M_G[v_1, v_2]$ , where  $D_G(v_1, v_2)$  is the geodesic distance between vertices  $v_1, v_2$ . Geodesic distances between particle positions on the implicit surface can now be computed via a barycentric interpolation scheme described below.

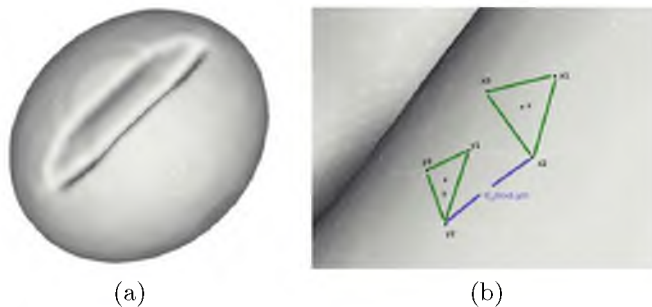


**Fig. 2.** (a) An example of a triangle mesh used for geodesic distance computations. (b) Configuration for two-layered interpolation of geodesic distance between arbitrary points:  $x$  and  $y$  are contained in triangles defined by vertices  $(x_1, x_2, x_3)$  and  $(y_1, y_2, y_3)$  respectively. The geodesic distances between vertices for all shapes are precomputed on a GPU.

To use this discrete set of distances between particles, which lie in the volume and are constrained to lie on the implicit surface, we interpolate the mesh-vertex distances to the faces of the triangles. This requires two layers of linear interpolation on the faces of the mesh. Let the barycentric coordinates of a point  $x$  in a triangle  $T_x$  defined by vertices  $(v_1, v_2, v_3)$  be given by  $(\alpha, \beta, \gamma)$  such that

the location of  $x$  can be given as  $x = \alpha v_1 + \beta v_2 + \gamma v_3$  where  $\alpha + \beta + \gamma = 1$ . Consequently, any function of  $x$  can be interpolated as  $f(x) = \alpha f(v_1) + \beta f(v_2) + \gamma f(v_3)$  provided its value is known at all vertices in the mesh. For the case of geodesic distances, the function  $f$  is the distance to another arbitrary point  $y$ , which can be evaluated on each vertex using this same interpolation scheme for the triangle  $T_x$  that contains  $y$ . To compute  $D_G(x, y)$  in a fast and efficient manner, we first determine the triangle faces on the mesh that contain points  $x$  and  $y$ , by projecting them onto the nearest face in the mesh. Let these triangles defined by vertices  $(x_1, x_2, x_3)$  and  $(y_1, y_2, y_3)$ , as shown in Fig. 2. Since the geodesic distance is a function defined between every pair of vertices in the mesh, we can approximate the geodesic distance between points  $x$  and  $y$  as

$$\begin{aligned} D_G(x, y) &\approx \alpha D_G(x_1, y) + \beta D_G(x_2, y) + \gamma D_G(x_3, y), \\ D_G(x_i, y) &\approx \alpha D_G(x_i, y_1) + \beta D_G(x_i, y_2) + \gamma D_G(x_i, y_3). \end{aligned} \quad (2)$$

Each  $D_G(x_i, y_i)$  is simply an entry in the matrix  $M_G$  as described above. Thus, using this two-layered interpolation scheme, we can approximate geodesic distances between particle positions on the implicit surface. The Gaussian forces of repulsion governing the motion of particles can then be computed as a function of these geodesic distances to improve sensitivity to the underlying geometry.

**Correspondence Optimization with Surface Normals.** The cost function described in Eq. 1 relies on particle positions to find a balance between a compact ensemble representation and a good distribution of particles on each surface. However, with an ensemble containing highly curved or convoluted surfaces, like those shown in Fig. 1, a reliance on only positional information may lead to incorrect correspondences. To address this shortcoming, we propose the addition of an intershape penalty term based on surface normals to disambiguate correspondences near highly curved features. Thus, we associate with each particle on each surface a pair of  $d$ -tuples  $(x_i, n_i) \in \mathbb{R}^d \times S^2$ , where  $S^2$  is the unit sphere.

We denote the total collection of  $N$  normals across  $M$  shapes as  $V$ . With the assumption that  $N > M$ . Assuming a Gaussian model with a covariance  $\Sigma$ , we can compute the entropy

$$H(V) \approx \frac{1}{2} \log |\Sigma| \approx \frac{1}{2} \log \left| \sum_i \sum_k \hat{n}_i^k \cdot (\hat{n}_i^k)^T \right| \quad (3)$$

For the  $i$ th particle on the  $k$ th shape,  $\hat{n}_i^k = d(n_i^k, \bar{n}_i)$ , where  $\bar{n}_i$  is the Fréchet mean defined in [6]. Since the normals are points on the Riemannian manifold  $\mathcal{M} \in S^2$ ,  $\hat{n}_i^k = \text{Log}_{\bar{n}_i}(n_i^k)$  [6]. In the tangent plane  $\mathcal{T}_{\bar{n}_i} \mathcal{M}$ , we have

$$\hat{n}_i^k = \text{Log}_{\bar{n}_i}(n_i^k) = \frac{P_t(n_i^k - \bar{n}_i) \arccos(n_i^k \cdot \bar{n}_i)}{1 - (n_i^k \cdot \bar{n}_i)^2} \quad (4)$$

where  $P_t$  is the idempotent projection matrix given by  $(I - \bar{n}_i \cdot (n_i^k)^T)$ . Since  $\Sigma$  will not have a full rank in practice, we implement a regularization similar to that

described in [1] to introduce a lower bound on the eigenvalues. The optimization problem in Eq. 1 can now be reformulated as

$$Q = H(\mathbf{Z}) - \sum_k H(P^k) + H(V) \quad (5)$$

The Riemannian distances are functions of normals;  $\hat{n}_i^k = f(n_i^k)$ , which in turn are a function of position;  $n_i^k = n(x_i^k)$ , the gradient descent on  $H(V)$  with respect to particle position  $x_i$  is given by the chain rule:

$$\frac{\partial H(V)}{\partial x_i^k} = \frac{\partial H(V)}{\partial \hat{n}_i^k} \cdot \frac{\partial f(n_i^k)}{\partial n_i^k} \cdot \frac{\partial n(x_i^k)}{\partial x_i^k} \quad (6)$$

This incremental update gets projected onto the tangent plane of the surface, as part of the algorithm described in Sec. 2, in order to maintain the constraint that particles remain on the surface. As with the geodesic distances, the curvature,  $\partial n_i^k / \partial x_i^k$ , is precomputed. Here we use the formulation of curvature for the level sets of the volume using finite differences (combined with a Gaussian kernel of standard deviation 1.0). The means of the normals are updated after each full iteration (one update for every particle on every shape).

## 4 Results and Discussion

This section details experiments designed to illustrate and validate the proposed method. First, we present an experiment with synthetically generated *coffee bean* shapes, that consist of an ellipsoid with a *slot* or indentation, creating a high-curvature feature that would confound the previous approaches. We also present an application to a study of group differences in the left ventricular myocardium.

### Synthetic Data

Computational solid geometry methods were used to compute the intersection of a small ellipsoid with axes  $a$ ,  $b$  and  $c$ , and a larger ellipsoid with axes  $A$ ,  $B$  and  $C$ , to create a *coffee bean* shape. The *slot* was then moved and scaled stochastically, to create a population of 10 *coffee bean* shapes. The position of the *slot* was chosen from a uniform distribution in the range  $[-B/3, B/3]$ , and its width was sampled from a Gaussian distribution of  $\mu = 8$  and  $\sigma = 2$ . Both, the method in [1] and the proposed method were applied to distribute 1024 correspondences across the ensemble. Both methods identified two dominant modes of variation, with significantly different amount of leakage into smaller modes. These modes are illustrated in Fig. 3 for both the methods, to 2 standard deviations. The proposed method lost 4% of the total variation into smaller modes, compared to 16% lost by the original method. Thus, the proposed method was able to characterize the variation in the population better than the original method, while remaining faithful to the original shape representation (as seen from the reconstructions in Fig. 3).

**Application to Group Comparison.** We applied the proposed methods to study group differences in the left ventricular myocardium of ischemic patients

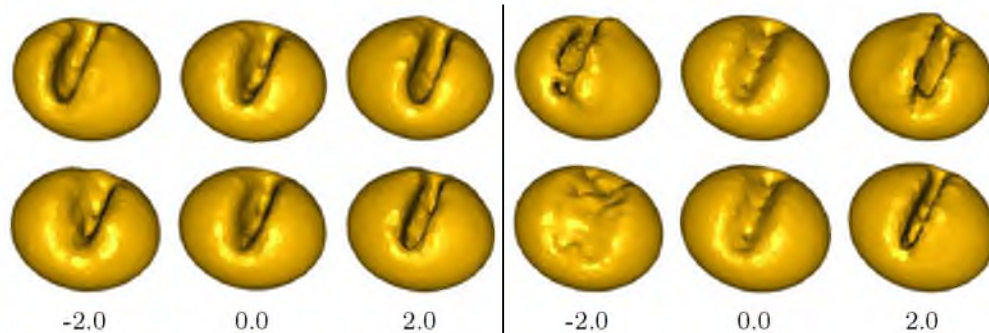


**Fig. 3.** Mean shape computed from the proposed method (left) and the original method (right), projected onto the first (top) and second (bottom) PCA modes, and  $\pm 2$  standard deviations

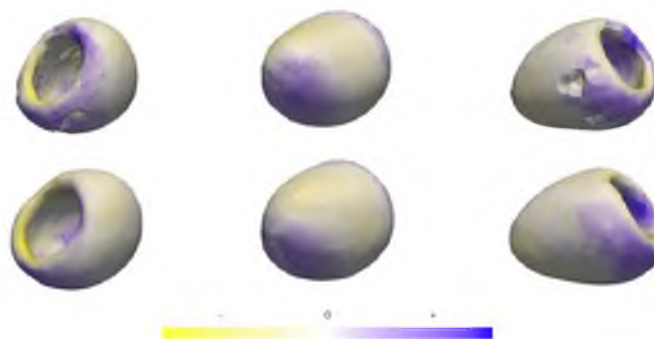


**Fig. 4.** Visualizing mean differences between normal and ischemic groups (blue denotes expansion and yellow denotes contraction) using [1] (top row) and the proposed method (bottom row)

and non-ischemic controls, using segmented volumes of the left ventricular myocardium at end diastole (ED) as inputs. The proposed method was used to initialize and optimize 1024 correspondences across the ensemble of 21 (12 patients, 9 controls) shapes. We then used *parallel analysis* to project the correspondences into a lower dimensional space determined by choosing an optimal number of basis vectors from principal component analysis (PCA). A standard, parametric Hotelling  $T^2$  test was used to test for group differences, with the null hypothesis that the two groups are drawn from the same distribution. In this case, the hypothesis test results in a highly significant *p-value* of 0.005, with 7 PCA modes chosen by *parallel analysis*.

Fig. 4 (bottom row) shows the differences between the mean shape surfaces for the normal and ischemic groups. To visualize the group differences driving statistical results, we use the linear discriminant vector, rotated from PCA space into the full dimensional shape space, and mapped onto the mean group shape surfaces to give an indication of the significant morphological differences between

groups. The above experiment was also conducted using the method described in [1]. The resulting group differences, visualized in Fig. 4 (top row), were also found to be statistically significant with a  $p$ -value of 0.005 using the Hotelling  $T^2$  test. However, the shape differences obtained using the proposed method are found to be more consistent with previously published results presented in [7], as compared to those obtained using [1].

## 5 Conclusion and Future Work

This paper extends the method given by [1] to improve particle distribution and correspondences across an ensemble of highly convoluted surfaces. The first contribution is the inclusion of geodesic distance to compute the intrashape particle interactions, which results in improved sensitivity of the particle distribution to the underlying surface geometry. The second contribution is the introduction of an intershape penalty term based on surface normals, to improve correspondence near sharp features. Results on synthetic and real data indicate that the proposed method provides a practical solution to compute correspondence models of ensembles of highly convoluted surfaces in an efficient and robust manner.

**Acknowledgements.** This work is supported by the NIH/NCRR Center for Integrative Biomedical Computing - 2P41 RR0112553-12, the NIH/NCBC National Alliance for Medical Image Computing - U54-EB005149 and NSF grant CCF-073222. We are also grateful to Dr. Raimond Winslow at The Center for Cardiovascular Bioinformatics and Modeling, John Hopkins University, for providing left ventricle data for the group comparison experiment.

## References

1. Cates, J., Fletcher, P.T., Styner, M., Shenton, M., Whitaker, R.: Shape modeling and analysis with entropy-based particle systems. In: Karssemeijer, N., Lelieveldt, B. (eds.) IPMI 2007. LNCS, vol. 4584, pp. 333–345. Springer, Heidelberg (2007)
2. Davies, R., Twining, C., Allen, P., Cootes, T., Taylor, C.: Shape discrimination in the hippocampus using an MDL model. In: Taylor, C.J., Noble, J.A. (eds.) IPMI 2003. LNCS, vol. 2732, pp. 38–50. Springer, Heidelberg (2003)
3. Fu, Z., Kirby, M., Whitaker, R.: A fast iterative method for solving the eikonal equation on triangulated meshes. *SIAM Journal on Scientific Computing* (2011) (to appear)
4. Jeong, W., Whitaker, R.: A fast iterative method for eikonal equations. *SIAM Journal on Scientific Computing* 30(5), 2512–2534 (2008)
5. Meyer, M.D., Georgel, P., Whitaker, R.T.: Robust particle systems for curvature dependent sampling of implicit surfaces. In: *Proceedings of the International Conference on Shape Modeling and Applications*, pp. 124–133 (June 2005)
6. Fletcher, P., Lu, C., Pizer, S., Joshi, S.: Principal geodesic analysis for the study of nonlinear statistics of shape. *IEEE Trans. Med. Imaging* 23(8), 995–1005 (2004)
7. Ardekani, S., Weiss, R., Lardo, A., George, R., Lima, J., Wu, K., Miller, M., Winslow, R., Younes, L.: Computational method for identifying and quantifying shape features of human left ventricular remodeling. *Ann. Biomed. Eng.* 37(6), 1043–1054 (2009)

## **CHAPTER 6**

# **GEODESIC DISTANCES TO LANDMARKS FOR DENSE CORRESPONDENCE ON ENSEMBLES OF COMPLEX SHAPES**

This chapter is a preprint of Proc. MICCAI, Geodesic distances to landmarks for dense correspondence on ensembles of complex shapes, vol. 2, 2013, pp. 19-26, M Datar, I Lyu, SH Kim, J Cates, M A Styner, RT Whitaker, with permission of Springer

# Geodesic Distances to Landmarks for Dense Correspondence on Ensembles of Complex Shapes

Manasi Datar<sup>1</sup>, Ilwoo Lyu<sup>2</sup>, SunHyung Kim<sup>3</sup>, Joshua Cates<sup>1,4</sup>,  
Martin Styner<sup>2,3</sup>, and Ross Whitaker<sup>1</sup>

<sup>1</sup> Scientific Computing and Imaging Institute, University of Utah

<sup>2</sup> Department of Computer Science, University of North Carolina at Chapel Hill

<sup>3</sup> Department of Psychiatry, University of North Carolina at Chapel Hill

<sup>4</sup> CARMA Center, University of Utah

**Abstract.** Establishing correspondence points across a set of biomedical shapes is an important technology for a variety of applications that rely on statistical analysis of individual subjects and populations. The inherent complexity (e.g. cortical surface shapes) and variability (e.g. cardiac chambers) evident in many biomedical shapes introduce significant challenges in finding a useful set of dense correspondences. Application specific strategies, such as registration of simplified (e.g. inflated or smoothed) surfaces or relying on manually placed landmarks, provide some improvement but suffer from limitations including increased computational complexity and ambiguity in landmark placement. This paper proposes a method for dense point correspondence on shape ensembles using geodesic distances to a priori landmarks as features. A novel set of numerical techniques for fast computation of geodesic distances to point sets is used to extract these features. The proposed method minimizes the ensemble entropy based on these features, resulting in isometry invariant correspondences in a very general, flexible framework.

## 1 Introduction

Establishing point correspondence between two or more shapes is a key algorithmic component in many medical image analysis applications. Various technical strategies—including registration, alignment to a template or matching features/measurements—have been used to study not only geometric changes in shape, but also image and model measurements relevant to specific applications. While many systems rely on alignment to a common template, the literature shows some advantages in building correspondences in an unbiased way by using an entire ensemble of subjects [1]. Automatic correspondence optimization has benefited from recent approaches like the spherical harmonics (SPHARM) description [2], which implicitly computes dense correspondences across shapes using a continuous one-to-one mapping of each shape to the unit sphere. The Minimum Description Length (MDL) method [3] also relies on spherical parameterization to compute correspondences but is computationally expensive and

thus rendered impractical. The point distribution model given by Cates et al [4] provides a flexible framework to establish dense point correspondences across shapes in a nonparametric fashion, without the constraint of a particular parameterization or topology.

The inherent complexity of certain classes of biomedical shapes presents significant challenges in the establishment of point correspondences. For instance, studies of degenerative conditions such as autism and Alzheimer’s disease benefit from the analysis of local cortical thickness measurements of the brain and rely on shape matching for valid comparison between subjects. Some of these techniques are initialized using manually delineated surface features (major sulci) to drive the matching procedure [5,6]. The many folds of the cortex can easily cause sulci to cross over each other and become aligned with the wrong features in the target or template. Widely used software packages such as FreeSurfer and BrainVoyager use cortex *inflation*—a process of removing cortical folds and then, typically, mapping to a sphere—to overcome the complexity in matching cortical surfaces. One of the goals of this work is to avoid this intermediate, inflated representation.

Correspondence based on point positions is sensitive not only to shape complexity, but also to anatomical variability in shapes. This can lead to inconsistent correspondences on surfaces where it is difficult to automatically match landmarks across a wide range of shapes. An example is the structural analysis of the left atrium (LA), which is of particular interest in atrial fibrillation (AF) studies. Recent advances in MRI have enhanced structural imaging of the LA but a high degree of variability in the LA anatomy presents a significant challenge in automatic identification of anatomically significant landmarks for quantitative analysis. The incorporation of a sparse set anatomically based landmark features, identified by either an expert or some automated process, can dramatically improve dense automatic correspondence in these scenarios.

The strategy in this paper is motivated by two observations. First is the relative success of alignment techniques, such as [5], that rely on nearly isometric, smooth mappings to simplified parameterizations in order to find appropriate deformations to templates. This suggests that positions on the surface rather than the ambient space are an important in anatomical alignment. The second observation is the success of landmark-distance-based features in recognizing shapes in computer vision applications [7,8,9]. Although these methods rely on combinatorial matching algorithms, which are not particularly well suited to the applications we address here, these works do demonstrate that collections of geodesic distances are rich, nearly complete, descriptions of shapes.

## 2 Technical Background

The proposed method (geodesic distance method) builds on the correspondence optimization method proposed in [4] as well as efficient parallel solvers for the eikonal equation on triangular meshes proposed by Fu et al [10]. Here we give a brief review of the results from these works that are relevant to our method.

**Correspondence Optimization.** We define a surface  $S \subset \mathbb{R}^d$  (e.g.,  $d = 3$  for volumes), as a smooth, closed manifold of codimension one. We sample  $S$  using a discrete set of  $N$  points that are considered as random variables  $\mathbf{Z} = (\mathbf{X}_1, \mathbf{X}_2, \dots, \mathbf{X}_N)^T$ ,  $\mathbf{X} \in \mathbb{R}^d$  drawn from a probability density function (PDF),  $p(\mathbf{X})$ . An ensemble comprised of  $M$  surfaces,  $\mathcal{E} = \mathbf{z}^1, \dots, \mathbf{z}^M$  can be described by a  $Nd \times M$  matrix of particle positions  $P = (\mathbf{x}_j^k)$ , where  $k = 1, \dots, M$  and  $j = 1, \dots, N$ . Let  $\mathbf{z}^k \in \mathbb{R}^{Nd}$  be an instance of a random variable  $\mathbf{Z}$ , then, modelling  $p(\mathbf{Z})$  parametrically as a Gaussian with covariance  $\Sigma$  gives the entropy  $H(\mathbf{Z}) \approx \frac{1}{2} \log |\Sigma| = \frac{1}{2} \sum_{j=1}^{Nd} \log \lambda_j$ , where  $\lambda_j$  are the eigenvalues of  $\Sigma$ . We estimate the covariance from the data, letting  $Y$  denote the matrix of (centered) points for the ensemble, which gives  $\Sigma = (1/(M-1))YY^T$ . Because  $N > M$ , we perform the computations on the dual space (dimension  $M$ ). Thus, we have the cost function  $G$  associated with the ensemble entropy:

$$\log |\Sigma| \approx G(P) = \log \left| \frac{1}{M-1} Y^T Y \right| \quad \text{and} \quad -\frac{\partial G}{\partial P} = Y(Y^T Y + \alpha I)^{-1}. \quad (1)$$

where  $|\cdot|$  is the matrix determinant. The combined ensemble and shape cost function is defined by  $Q = H(\mathbf{Z}) - \sum_k H(P^k)$ . The optimization process of this cost function is defined via gradient descent, by moving individual points on the surface, as described in [4].

**Fast Geodesic Distance Computation.** The proposed method requires the computation of geodesic distances to landmarks (points/curves) at all correspondence positions. Performing these calculations over large ensembles of shapes is prohibitive without the use of fast, parallel algorithms for solving the hyperbolic partial differential equations (PDE) as well as extremely fast graphics processing units (GPUs). One such method, the fast iterative method (FIM) [11] formulates the distance between each point  $a$  on the surface and every other point, as the solution to the eikonal equation  $|\nabla u| = 1$ , using the boundary condition  $u(a) = 0$ . An extension of FIM for triangular meshes [10] that performs fast computation of geodesic distances between vertices on a triangle mesh is used to compute geodesic distance features.

### 3 Methodology

Rather than use absolute particle positions, as in [4], we propose to leverage manually placed landmarks (points/curves) to guide correspondence optimization via geodesic distances to these landmarks. Consider a manifold  $\mathcal{M} \subset \mathbb{R}^d$  with a point  $x$  and a landmark  $l$ . We can define a mapping  $D: \mathcal{M} \rightarrow \mathbb{R}$ , where  $D(x, l)$  is the geodesic distance of point  $x$  to the landmark  $l$ . Given a triangulated surface to describe  $\mathcal{M}$  and a point set to describe landmark  $l$ , we can use the FIM method [10] to compute  $D(x, l)$  for all points  $x \in \mathcal{M}$  by setting appropriate boundary conditions on the eikonal equation. In practice, we compute these distances to all points on the mesh and interpolate these discrete samples onto the

22 M. Datar et al.

triangle faces, as in [12]. Given an ensemble of shapes, as described in Sec. 2 and a set of  $T$  landmarks (points/curves) for each shape, we can represent particle  $j$  on shape  $k$  as a vector of geodesic distances:  $\tilde{p}_j^k = (D(x_j^k, l_1^k), \dots, D(x_j^k, l_T^k))$  from  $T$  landmarks. Using the entropy minimization framework from Sec. 2, the ensemble entropy term in (1) can be modified to compute covariance of the geodesic distance features instead of particle positions, giving

$$G(\bar{P}) = \log \left| \frac{1}{M-1} \tilde{Y}^T \tilde{Y} \right| \quad (2)$$

where,  $\tilde{Y}$  is the matrix of geodesic distances to all landmarks at a correspondence point minus the mean geodesic distance to all landmarks for the same point across the ensemble. The derivative  $\partial G / \partial P$  is computed by the chain rule as

$$-\frac{\partial G}{\partial P} = J^T (\tilde{Y}^T \tilde{Y} + \alpha I)^{-1} \quad (3)$$

where  $J$  is the Jacobian matrix given by  $\partial D / \partial P$  and computed as a block diagonal matrix with diagonal blocks of  $T \times d$  submatrices of partial derivatives, computed numerically by projecting the correspondence points on to the surface. This gradient is used to update point correspondences in accordance with the optimization described in [4].

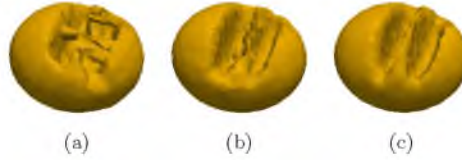


**Fig. 1.** Mean shapes from: (a) particle based automatic correspondence [4], (b) including fixed landmarks, and (c) and proposed method using geodesic distance features

**Proof-of-Concept Experiment.** Computational solid geometry methods were used to compute the intersection of a pair of ellipsoids with axes  $a$ ,  $b$  and  $c$ , with a larger ellipsoid with axes  $A$ ,  $B$  and  $C$ , to create a *coffee bean* shape with two *slots*—thus simulating an element of the cortical surface folds. The *slots* were then moved and scaled stochastically, to create a population of 10 *coffee bean* shapes. The position of the *slots* was chosen from a uniform distribution in the range  $[-B/3, B/3]$ , and the width was sampled from a Gaussian distribution of  $\mu = 8$  and  $\sigma = 2$ . The number of correspondences was set to 1024.

First, correspondences were distributed across the ensemble using the original formulation from [4]. The sole use of point positions, coupled with the complexity of the shape led to inconsistent correspondences, and the method failed to

compute a valid mean shape (Fig. 1(a)). Next, fixed landmarks were introduced (3 each in the two *slots* and 1 on the *ridge* between them) into the original formulation and the experiment was repeated. Fixed landmarks improved the consistency of correspondences, but position information alone is not isometry invariant, and thus resulted in a suboptimal mean shape (Fig. 1(b)). Finally, geodesic distances to these fixed landmarks were computed as described above and used to optimize correspondences in the proposed method. This resulted in isometry invariant, consistent correspondences, as evidenced by the mean shape (Fig. 1(c)).

#### 4 Results and Discussion

**Validation on Cortical Surfaces.** T1- and T2-weighted MRI scans were acquired for paediatric 2-year-old subjects as part of the Infant Brain Imaging Study (IBIS) network (<http://www.ibis-network.org>). Ten of these subjects were randomly selected for this study. A single subject was selected as template and an expert manually labelled 13 major curves on the template surface: superior temporal (STS), inferior temporal (ITS), medial-temporo-occipital (MTOS), central (CS), precentral (PreCS), postcentral (PostCS), inferior frontal (IFS) and superior frontal (SFS), intraparietal (IPS), cingulate (CingS), calcarine (CalcS), occipito-parietal (OPS), and sylvian (SylS) sulcus. Only left hemispheres were used. The input data was a set of segmented left hemispheres, with 13 sulcal curves each. 6 of these curves were selected as landmark curves (as shown in Table 1) and geodesic distances to these curves were used as features to optimize 6144 correspondences on each cortical surface. Sulcal depth was also used as an additional feature to guide the correspondence optimization. Two views



**Fig. 2.** Two views of the mean shape of the ensemble of left hemisphere cortical surfaces

of the mean shape computed from this model are shown in Fig. 2. Note that it is possible to identify all of the major sulci, including the ones not used in the optimization. Given the lack of ground truth for cortical surface data, we validate these results via analyses of surface measures (depth, thickness) and cross-validation based on the geodesic distance features. A cross-subject variance estimate of sulcal depth was computed over all correspondences across all

24 M. Datar et al.

shapes in the ensemble. The mean and std. deviation values of 1.39918 and 0.769351 were found to be consistent with the literature. Additionally, a cross-subject variance estimate of the cortical thickness was also performed, since the use of sulcal depth as a feature biases the previous test. The mean and std. deviation values of 0.494561 and 0.392878 were also found to be consistent with the literature [13].

Next, each set of curves was warped onto the mean space via thin plate spline warping and curve alignment was compared to the output of the CIVET pipeline, where major sulcal curves were initially mapped onto the common unit sphere by the surface registration method [14], and then further projected onto the template surface by a one-to-one mapping between the sphere and the template. Figure 3 shows a visual comparison of curve alignment from the geodesic distance

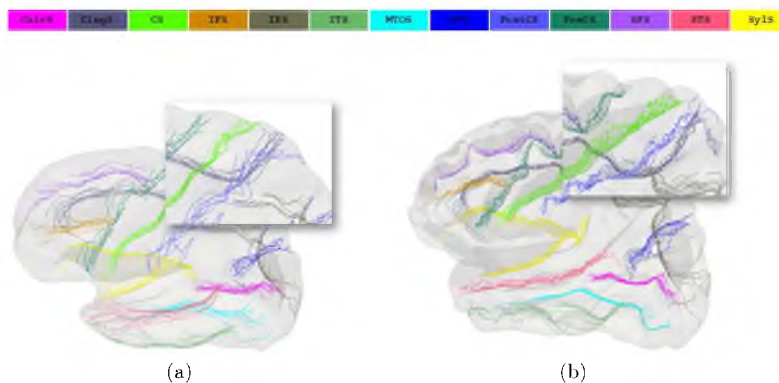


**Fig. 3.** Alignment of cortical curves in the mean space using the geodesic distance method (a) and the CIVET pipeline (b). Note that the two surface templates are different: mean template from geodesic distance method (a), MNI template (b).

method (a) with curve alignment from the CIVET pipeline (b). In general, alignment for curves used as features in the geodesic distance method was better than the CIVET result, while maintaining the smoothness of the curves. For unseen curves, CIVET alignment appears to be better, however this may be achieved at the cost of smoothness, as shown in the inset images for the CS curve. We also quantify sulcal curve alignment in Table 1, by looking at the average dissimilarity per curve, computed in a pair-wise manner using all points on the curve, over all pairs of shapes. Table 1 indicates that the geodesic distance method aligns 4 of the 6 curves used as features better than the CIVET pipeline. Moreover, the same is true for 6 of the remaining 7 unseen curves. These values indicate that the correspondences are consistent and isometry invariant, even for sulci that are not part of the landmark set. Thus the geodesic distance method provides a framework for further statistical analysis of the cortical surface without the need for inflation.

**Table 1.** Comparison of average dissimilarity per curve between proposed (top) and CIVET (bottom) methods, for curves used in correspondence optimization (left) and unseen curves (right)

	Curves used in optimization						Unseen curves						
	CingS	CS	IPS	STS	SFS	SylS	CalcS	IPS	ITS	MTOS	OPS	PostCS	PreCS
Proposed	3.42	2.18	7.19	6.79	4.67	3.75	2.31	4.63	8.43	5.00	3.69	6.61	5.24
CIVET	3.49	2.90	10.68	9.95	4.55	3.54	2.08	4.95	11.32	5.41	3.97	8.61	7.15

**Application to AF.** Thirteen shapes were retrospectively chosen from a database of patients who presented to the University of Utah for AF and underwent late-gadolinium enhancement (LGE) MRI to imaging. There were 6 patients with a pair of scans (pre- and post-ablation), and 1 singular post-ablation scan. The input data for the proposed model consisted of segmentations of the LA and attached LA appendage, created by experts using Corview ([www.corview.org](http://www.corview.org)). Landmark positions were manually identified using Corview for each of the pulmonary veins (left- and right-inferior and left- and right-superior) and the center of the mitral valve. As the most recognizable landmarks of LA, these structures are also the most appropriate features to drive correspondence across subjects. Using a feature vector of distances to each of these landmarks, 2560 correspondences were distributed on the LA shapes. Given the

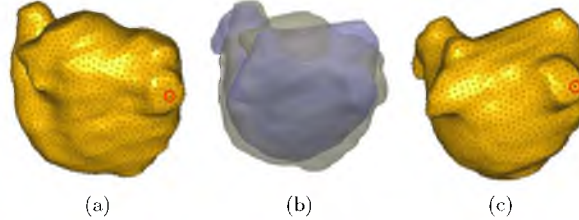


**Fig. 4.** Reconstructed median shapes for the pre-ablation (a) and post-ablation (c) groups, highlighting a particular correspondence. Overlay of the two median shapes, showing the high degree of variability (b).

variability of the LA, clustering the results into multiple means might be more interesting for specific applications. While such clustering is beyond the scope of this work, we can analyze the median shapes for each group, reconstructed using the correspondences. Figure 4 shows median shapes for the pre-ablation (a) and post-ablation (c) groups. A particular point is highlighted to display the proximity of the correspondences. An overlay of the group median shapes is shown in Fig. 4(b) to describe the variability present in the pre- and post-ablation groups. In future work, we hope to better model variability of important structures in the LA by adopting an anatomically-based coordinate system that explicitly incorporates their positional information.

**Acknowledgements.** The authors thank Joon-Kyung Seong (Dep Comp Sci, KAIST, South Korea) for use of his sulcal line extraction tool. This project was supported by grants from NIH-NCRR/NIH-NIGMS Center for Integrative Biomedical Computing-5P41RR012553/8P41GM103545, Roadmap Grant U54 EB005149-01 (NA-MIC), P30 HD03110, R01MH091645 and R01MH070890.

## References

1. Lorenzen, P.J., Davis, B.C., Joshi, S.: Unbiased atlas formation via large deformations metric mapping. In: Duncan, J.S., Gerig, G. (eds.) MICCAI 2005. LNCS, vol. 3750, pp. 411–418. Springer, Heidelberg (2005)
2. Styner, M., Oguz, I., Xu, S., Brechbühler, C., Pantazis, D., Levitt, J., Shenton, M., Gerig, G.: Framework for the statistical shape analysis of brain structures using SPHARM-PDM. *The Insight Journal* (2006)
3. Davies, R.H., Twining, C.J., Cootes, T.F., Waterton, J.C., Taylor, C.J.: 3D statistical shape models using direct optimisation of description length. In: Heyden, A., Sparr, G., Nielsen, M., Johansen, P. (eds.) ECCV 2002, Part III. LNCS, vol. 2352, pp. 3–20. Springer, Heidelberg (2002)
4. Cates, J., Fletcher, P.T., Styner, M., Shenton, M., Whitaker, R.: Shape modeling and analysis with entropy-based particle systems. In: Karssemeijer, N., Lelieveldt, B. (eds.) IPMI 2007. LNCS, vol. 4584, pp. 333–345. Springer, Heidelberg (2007)
5. Thompson, P.M., et al.: Mapping cortical change in alzheimers disease, brain development, and schizophrenia (2004)
6. Essen, D.C.V.: A population-average, landmark- and surface-based (pals) atlas of human cerebral cortex. *NeuroImage* 28(3), 635–662 (2005)
7. Bronstein, A.M., Bronstein, M.M., Kimmel, R.: Generalized multidimensional scaling: A framework for isometry-invariant partial surface matching. *Proceedings of the National Academy of Science*, 1168–1172 (2006)
8. Mémoli, F., Sapiro, G.: A theoretical and computational framework for isometry invariant recognition of point cloud data. *Foundations of Computational Mathematics* 5(3), 313–347 (2005)
9. Bronstein, A.M., Bronstein, M.M., Kimmel, R., Mahmoudi, M., Sapiro, G.: A gromov-hausdorff framework with diffusion geometry for topologically-robust non-rigid shape matching. *Int. J. Comput. Vision* 89(2-3), 266–286 (2010)
10. Fu, Z., Kirby, M., Whitaker, R.: A fast iterative method for solving the eikonal equation on triangulated meshes. *SIAM Journal on Scientific Computing* (2011)
11. Jeong, W., Whitaker, R.: A fast iterative method for eikonal equations. *SIAM Journal on Scientific Computing* 30(5), 2512–2534 (2008)
12. Datar, M., Gur, Y., Paniagua, B., Styner, M., Whitaker, R.: Geometric correspondence for ensembles of nonregular shapes. In: Fichtinger, G., Martel, A., Peters, T. (eds.) MICCAI 2011, Part II. LNCS, vol. 6892, pp. 368–375. Springer, Heidelberg (2011)
13. Lyu, I., et al.: Group-wise cortical correspondence via sulcal curve-constrained entropy minimization. In: Gee, J.C., Joshi, S., Pohl, K.M., Wells, W.M., Zöllei, L. (eds.) IPMI 2013. LNCS, vol. 7917, pp. 364–375. Springer, Heidelberg (2013)
14. Lyttelton, O., Boucher, M., Robbins, S., Evans, A.: An unbiased iterative group registration template for cortical surface analysis. *NeuroImage* 34(4), 1535–1544 (2007)

# CHAPTER 7

## APPLICATIONS

This chapter illustrates the application of techniques from this dissertation to understand driving biological problems in the fields of orthopedics, cardiology, and neuroscience. These studies address a variety of biomedical problems and provide a framework to test specific clinical hypotheses. These applications were made possible with help from various collaborators, who are acknowledged at relevant places in the following paragraphs.

### 7.1 Applications to Orthopedics

The relationship between form and function has been of increasing interest the orthopedics community. For example, Beck et al. [1] observe that an abnormally shaped femur may cause damage to the acetabular labrum due to shearing during hip flexion. Researchers have also extensively applied shape models to study bone shape in presence of pathology. Active shape models (ASM) have been used to study the correlation between proximal femur morphology and the rate of hip fracture in women [2], with the goal of developing a model-based paradigm to assess the risk of the occurrence of pathology in the event of a fracture. Further, statistical shape models have been used in the analyses of tibiofemoral and patellofemoral joints and image-based 3D reconstruction methods from femur or pelvis shapes [3–5]. However, most methods using 3D reconstructions assume an ideal geometry as a reference for the underlying bone shape (e.g., a perfectly spherical femoral head) [6]. Nonparametric correspondence methods, like the ones presented in this dissertation, allow comparison of complex 3D morphology without any assumptions about the associated geometry.

#### 7.1.1 Cam Type Femoroacetabular Impingement (CAM-FAI)

In collaboration with Dr. Andrew Anderson and Dr. Michael Harris from the Dept. of Orthopedics at the University of Utah, the shape analysis methods developed in this dissertation were applied to a study of femurs afflicted by femoroacetabular impingement (FAI). This work has been published in the Journal of Orthopedics [7].

FAI is caused by reduced clearance between the femoral head and acetabulum due to anatomic abnormalities of the femur (cam FAI), acetabulum (pincer FAI), or both (mixed FAI) [8]. Cam FAI is characterized by a malformed femoral head, as shown in the radiographs in Fig. 7.1. This condition may cause joint damage, leading to early hip osteoarthritis (OA) [9].

Two-dimensional radiographic measurements or a series of radial planes from CT or MR images are commonly used to diagnose cam FAI [10, 11]. While 2D measures provide initial diagnosis, they are largely unreliable [12], and there is no well-established normative range of measurements [13, 14]. Radiographic measures are also limited in their description of the variability in the femur shape in presence of FAI deformities and may lead to a high rate of misdiagnoses. 3D reconstruction of the femur from CT images provides a more comprehensive visualization of the entire femoral head and can be used to evaluate cam FAI. The statistical modeling methods presented in this dissertation were used to objectively compare femur morphology in the presence of deformities due to FAI, without any assumptions about the underlying geometry. Subsequent statistical analysis is expected to improve diagnosis of FAI and facilitate surgical planning. Further comparison with a healthy population may yield a quantitative measure of FAI severity, while analysis of shape variability may also find clinical use in the description of FAI deformities and their classification.



**Figure 7.1.** Radiographs showing healthy (left) and cam FAI (right) femurs. The circle indicates the anterolateral head-neck junction.

#### 7.1.1.1 Data

A cohort of cam FAI patients was retrospectively collected from the University of Utah and Intermountain Healthcare orthopedic centers. Subject selection and modeling received IRB approval from both institutions. Volumetric CT images of the pelvis and proximal femur were retrospectively acquired from 30 cam FAI patients (28 males, 2 females). CT scans for 79 possibly control femurs were retrospectively obtained (with IRB approval). Of these, 20 subjects received a CT arthrogram as part of a previous study [15]. These subjects had no history of hip pain and no radiographic evidence of OA. The remaining 59 femurs were from a database of cadavers that had been previously scanned [7].

The proximal femur to lesser trochanter of each femur was segmented and reconstructed from the CT image data using the Amira software (v5.4, Visage Imaging, San Diego, CA). Reconstructed surfaces were triangulated, and segmentation artifacts were removed by slightly smoothing surfaces using tools available in Amira. Reconstructions were cropped at the superior aspect of the lesser trochanter, considered to be the most inferior location where cam FAI deformities might extend. The cropped reconstructions were then aligned in Amira using a built-in iterative closest point algorithm to minimize the root mean square (RMS) distance between surfaces. Finally, surface reconstructions were converted to binary segmentations, which were input to the shape analysis pipeline.

Shape variation was also correlated with existing 2D and 3D measures of femoral anatomy using Pearson's correlation coefficient. A detailed correlation analysis is presented in [7].

#### 7.1.1.2 Shape Analysis

The input binary segmentations were further preprocessed to remove aliasing artifacts, and 2,048 particles were placed on each femur, using the method described in Chapter 5 and the constraint for open surfaces described in Chapter 3. The generalized Procrustes algorithm was applied regularly during optimization to align shapes with respect to rotation and translation and to normalize with respect to scale. Group labels were used to separate the particle configurations of controls and cam patients, and the mean shape for each group was constructed as the mean of the particle configurations from all shapes belonging to that group [7].

Parallel analysis [16, 17] determined that the first six modes captured significant variation and were used for further analysis. The six modes captured 83.8% of the cumulative variation among all femurs. PCA, run on the control and patient groups independently, showed similar areas of intragroup variation.

Qualitative and quantitative descriptions of variation captured by the first three modes are shown in Fig. 7.2. For both groups, variation in mode 1 was most substantial at the mediallylateral distance from tip of greater trochanter to center of the head and the distance between the proximal tip of the greater trochanter and the proximal lesser trochanter. For the patient group, mode 1 also captured variation in concavity at the head-neck junction. For both groups, mode 2 primarily described variation in the diameter of the neck. Finally, mode 3 captured variation in the curvature of the greater trochanter in both groups.

Classification of these areas of high variation may assist in resolving the persistent clinical problem of establishing rubrics that can reliably distinguish normal and pathological femurs, based on morphology alone.

The patient mean was locally larger than the control mean by up to 3.3 mm at the anterolateral head-neck junction. Sustained protrusions of 2.5–3.0 mm were distributed from the AP midline of the femoral neck and distally along the anterior neck. The differences between mean control and cam FAI femurs correspond well with previous findings related to cam type lesions and intraoperative observations related to soft-tissue damage. A Hotelling  $T^2$  test was used to test for group differences between the mean control and patient shapes, with the null hypothesis that the two groups were drawn from the same distribution. This test demonstrated significant differences between the patient and control mean shapes ( $p < 0.001$ ). Fig. 7.3 shows the morphological differences between the control and patient mean shapes.

### 7.1.1.3 Discussion

Statistical shape models were constructed to compare femoral head morphology between control and cam FAI femurs. Local shape differences between the mean shapes from the two groups were found to be consistent with the locations of the cam lesions and corresponding joint damage reported in literature [9]. Considerable variation was found in the shape and height of the greater trochanter among all femurs and between groups. There were also large variations among femurs in the distance between the greater trochanter and the center of the head (i.e., femoral offset) and the neck diameter, demonstrating the ability of the statistical model in providing a comprehensive picture of the variations in femoral shape and the spectrum of possible deformities.

A comparison of individual samples with the mean shapes can possibly be used to improve FAI diagnosis and treatment. As shown in Fig. 7.4, 3D reconstruction of a patient with cam FAI could be objectively compared to the mean control femur to produce a map

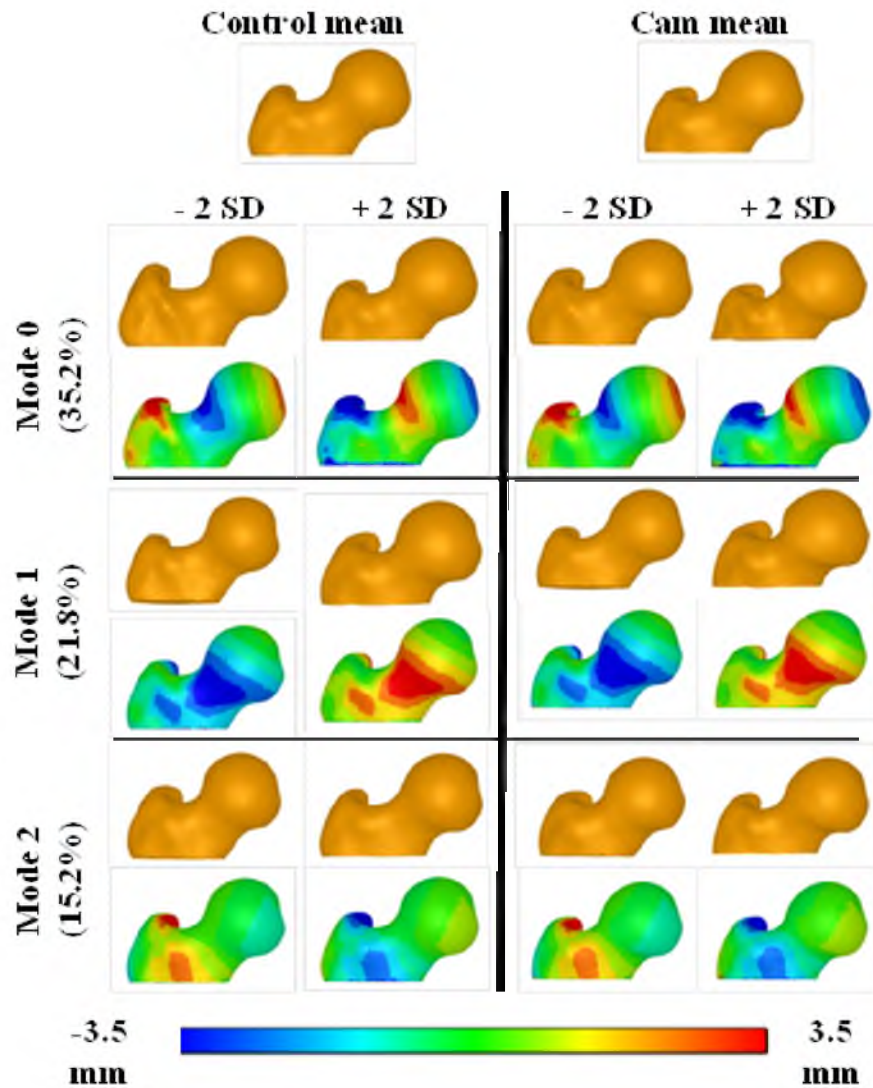


**Figure 7.2.** Shape variation captured in the first 3 modes. Shapes at  $\pm 2$  SD shown for each mode. Color plots indicate differences between various shapes and the means (shown).

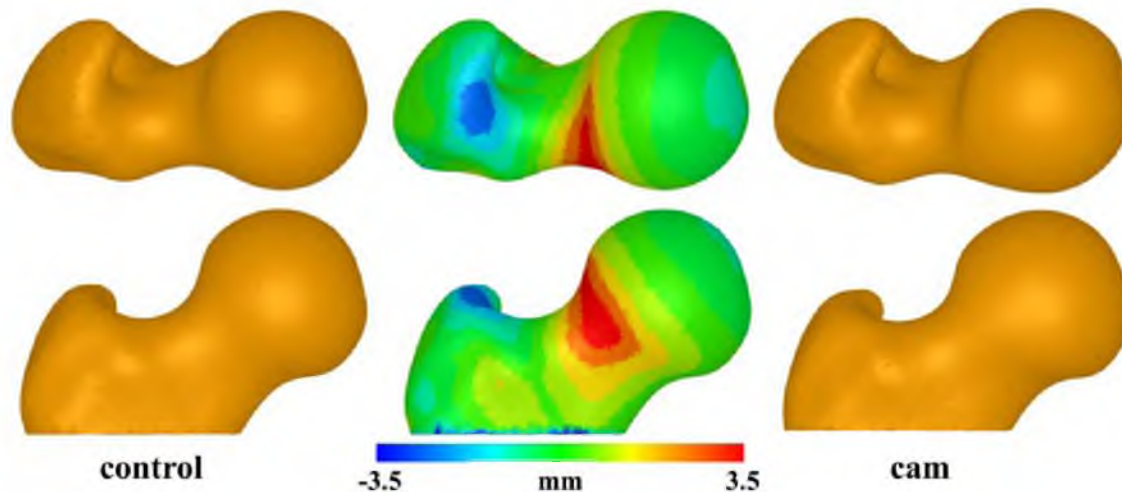


**Figure 7.3.** Mean control and cam femur shapes. Colors indicate difference between control (shown) and cam means. From M. D. Harris, M. Datar, R. T. Whitaker, E. R. Jurrus, C. L. Peters, and A. E. Anderson, Statistical shape modeling of cam femoroacetabular impingement, *J. Orthop. Res.*. Copyright © 2013 by John Wiley Sons, Inc. Reprinted by permission of John Wiley & Sons, Inc.

elucidating the magnitude and location of bone debridement required for correction, thus facilitating exact surgical planning.

Another persistent problem with diagnosing cam FAI is the establishment of rubrics that can reliably distinguish pathologic from normal femurs. A comparison of individual patient samples with the mean pathological shape can be used to assess disease severity and develop new, perhaps more reliable measurements of anatomy to diagnose FAI. Also, [7] presents a detailed discussion of other findings from this study. On a final note, shape variability captured by the significant modes may also be useful in identifying shape changes that are contributing factors to FAI, rather than a retrospective evaluation of patient population variation. Such information may help in the characterization of morphological differences between healthy and pathologic bones and aid classification of extreme/unusual cases.

### 7.1.2 Mouse Model of Multiple Osteochondroma (MO)

This project involved application of the proposed shape analysis methods to study the short bone phenotype associated with multiple osteochondroma (MO). The cancer was studied in mouse models created by Dr. Kevin Jones, from the Huntsman Cancer Institute, University of Utah School of Medicine. This work has been published in the *Journal of Orthopedics* [18].

MO is a heritable disorder characterized by the variably penetrant development of

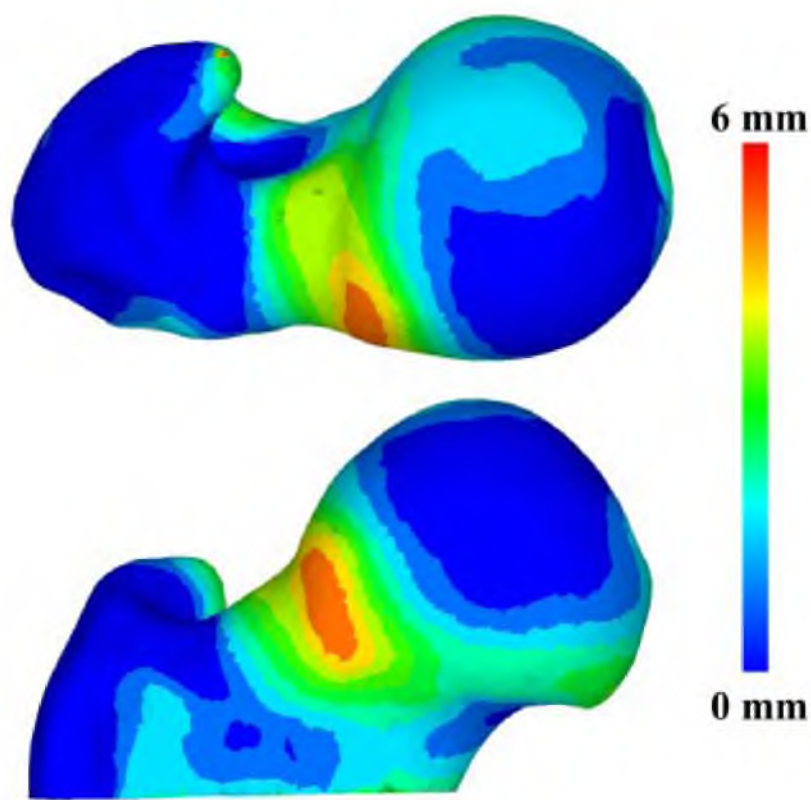


**Figure 7.4.** Color plot of a single cam FAI femur (shown) and the amount it deviated from the average control femur. These plots could be used as guide for planning surgical debridement to relieve FAI. From M. D. Harris, M. Datar, R. T. Whitaker, E. R. Jurrus, C. L. Peters, and A. E. Anderson, Statistical shape modeling of cam femoroacetabular impingement, *J. Orthop. Res.*. Copyright © 2013 by John Wiley Sons, Inc. Reprinted by permission of John Wiley & Sons, Inc.

multiple cartilage-capped bony excrescences on the metaphyses of long bones, called osteochondromas or extostoses [19, 20]. Individuals with MO demonstrate visible shortening of the long bones, resulting in reduced stature and pronounced deformities. This *short bone* phenomenon presents great clinical challenges, but is still little understood. Mouse models have suggested that haploinsufficiency cannot induce the short bone phenotype, in that mice inheriting loss of a single functional copy of *Ext1* or *Ext2* in the germline do not have discernibly shortened bones [21, 22]. However, this suggests the hypothesis that multiple osteochondromas might directly lead to a *steal phenomenon*, in which some physal chondrocytes are redirected to grow peripherally rather than contribute to longitudinal growth. Studying longitudinal growth variation in humans is very difficult since this variation is typically small (approximately 10% of length) as compared to the wide population variation in bone lengths. However, the mouse model, previously described in [23], provides a tight control group of littermates, and induction of osteochondromas can be timed at different points during growth to achieve an anticipated range of severity in osteochondroma formation at different ages.

#### 7.1.2.1 Mouse Model and Data

For these particular experiments, mice were induced to lose both functional copies of *Ext1* via the transgene Cre-recombinase, in a minority of chondrocytes by administration of doxycycline in the drinking water (4 mg/ml) for a duration of 8 days beginning during the first, second, or fourth week of life (with the approval of the IACUC). All mice were male and euthanized for imaging at 12 weeks age. Controls were littermates, lacking Cre-recombinase, having similarly received doxycycline. Shape analysis of subsequent CT scans can then be used to measure bone lengths as well as compute volumes of bones and localized deviations of volume by comparison with a mean shape from control littermates [18].

CT scans obtained at 46  $\mu$ m resolution were exported as DICMs and analyzed. Binary segmentations of the femora and tibiae, derived from the CT scans, were used as input to the statistical shape modeling process.

#### 7.1.2.2 Shape Analysis

The segmentations were preprocessed to remove aliasing artifacts, and 2,048 correspondences were initialized and optimized on each bone, using the strategy described in Chapter 5. The generalized Procrustes algorithm was applied at regular intervals during the optimization to align shapes with respect to rotation and translation and to normalize with respect to scale. Group labels were used to separate the point representation of controls

and mice with MO, and the mean shape for each group was constructed as the mean of the correspondences from all shapes belonging to that group.

Mice forming osteochondromas were noted to have shorter femora and tibiae, most consistently among those induced to lose both functional copies of *Ext1* at a young age. An analysis of the group mean shapes showed that bones from mice with osteochondromas were both shorter overall and wider in the metaphyses as shown in Fig. 7.5.

The femora and the tibiae were analyzed separately, starting with a few common steps. Principal component analysis (PCA) was used to reduce the dimensionality required to examine variation among the different bones. Parallel analysis was then performed to determine the number of principal component modes representing significant variations among the bones. This analysis determined that the first five modes were significant for the femora, while the first four modes should be used for further analysis of the tibiae.

Using the significantly contributing modes designated by parallel analysis, a standard parametric Hotelling  $T^2$ -test was used to test for group differences (control vs. doxycycline at 1, 2, or 4 weeks), with the null hypothesis that the two groups are drawn from the same distribution. For both the femora and the tibiae, the Hotelling  $T^2$ -test resulted in a significant difference in the group mean shapes ( $p < 0.01$ ). The group mean differences are visualized in Fig. 7.6 and show mean surface expansion/contraction for each of the three disease groups as compared to the mean control shape.

Comparing individual bones from induced mice to the control mean shape revealed that large metaphyseal shape deviations were only weakly correlated with shortening of the bones, as shown in Fig. 7.7.

After aligning femora at the knee and cropping distal femoral volumes to include only the metaphyses and discard the impact of volume deviation due to overall bone shortening, deviations of metaphyseal volumes from the mean of the control femora demonstrated no correlation with length as shown in Fig. 7.8.

While there is a severe reduction in length among some femora with large peripheral gains in metaphyseal volumes, others have abundant osteochondromas and metaphyseal volumetric expansion but minimal to no shortening.

### 7.1.2.3 Discussion

When induction of osteochondromagenesis was initiated early in skeletal development, femora and tibiae were approximately 10% shorter at the end of skeletal growth, but were not smaller in total volume, as the metaphyseal expansion in the form of osteochondromas compensated for and generally even slightly overcompensated for the loss of volume due to



**Figure 7.5.** Volumetric overlay of mean shape of murine femora and tibiae following induction of homozygous loss of *Ext1* in a minority of chondrocytes at variable ages during skeletal growth. Aligned here at the distal femur (upper) and proximal tibia (lower) to demonstrate the overhanging metaphyseal width in each osteochondroma forming group (left, doxycycline at 1 week; middle, doxycycline at 2 weeks; right, doxycycline at 4 weeks) and the overhanging length of the control group mean shape. From K. B. Jones, M. Datar, S. Ravichandran, H. Jin, E. Jurrus, R. Whitaker, and M. R. Capecchi, Toward an understanding of the short bone phenotype associated with multiple osteochondromas, *J. Orthop. Res.*, vol. 31, no. 4, pp. 651657. Copyright © 2013 by John Wiley Sons, Inc. Reprinted by permission of John Wiley & Sons, Inc.

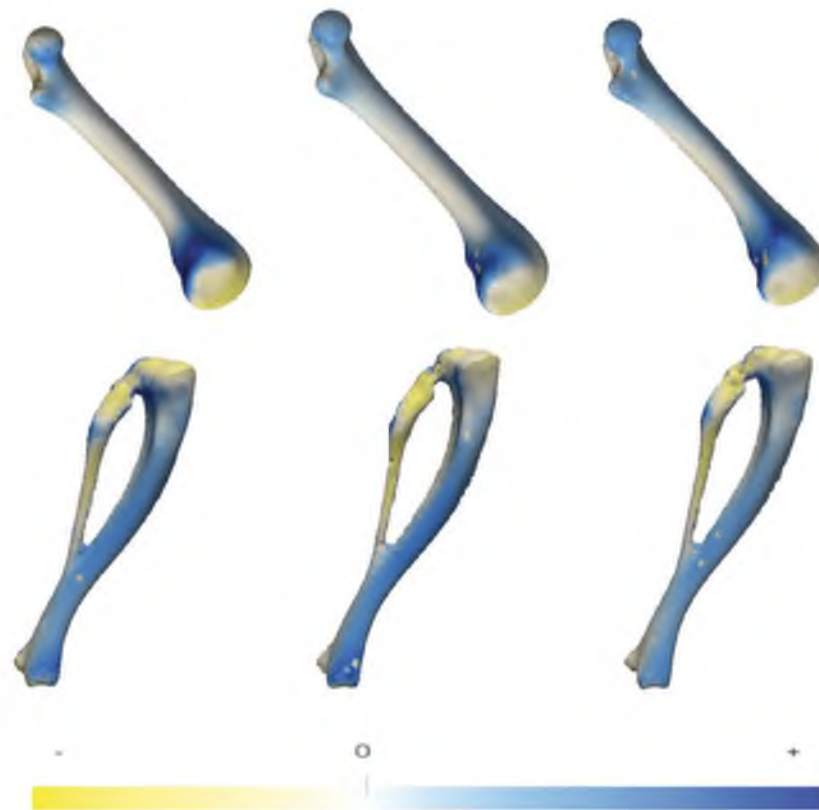


**Figure 7.6.** Mean shape of murine femora and tibiae following induction of homozygous loss of *Ext1* in a minority of chondrocytes at variable ages during skeletal growth. All three groups (Doxycycline beginning during week 1 on left, 2 in the middle, and 4 on right) demonstrated similar mean shape changes compared to controls, with shortening demonstrated by bone-end yellow-coloration indicating surface subtraction and metaphyseal widening demonstrated by blue-coloration indicating surface expansion. From K. B. Jones, M. Datar, S. Ravichandran, H. Jin, E. Jurrus, R. Whitaker, and M. R. Capecchi, Toward an understanding of the short bone phenotype associated with multiple osteochondromas, *J. Orthop. Res.*, vol. 31, no. 4, pp. 651-657. Copyright © 2013 by John Wiley Sons, Inc. Reprinted by permission of John Wiley & Sons, Inc.

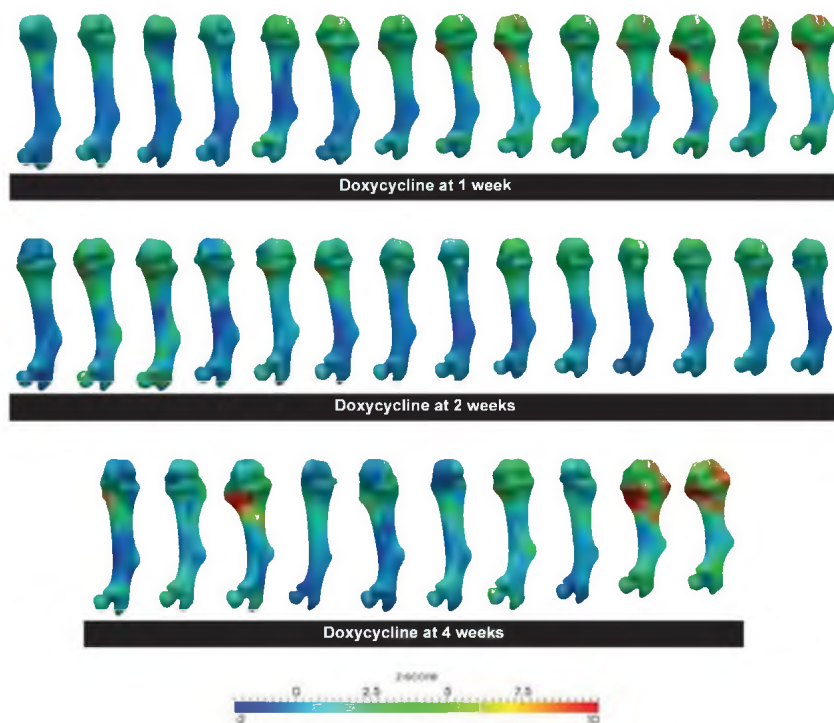


**Figure 7.7.** Metaphyseal widening does not consistently increase with decreasing length in the femora of mice that develop osteochondromas. Ordered from longest to shortest in each group, individual femora from mice treated with doxycycline at 1, 2, or 4 weeks age are depicted as rendered shapes, with colors indicating the deviations from the mean shape with regard to volume. While some of the shortest specimens have abundant red showing large deviations in volume, other specimens with large deviations are much longer in length. From K. B. Jones, M. Datar, S. Ravichandran, H. Jin, E. Jurrus, R. Whitaker, and M. R. Capecchi, Toward an understanding of the short bone phenotype associated with multiple osteochondromas, *J. Orthop. Res.*, vol. 31, no. 4, pp. 651657. Copyright © 2013 by John Wiley Sons, Inc. Reprinted by permission of John Wiley & Sons, Inc.

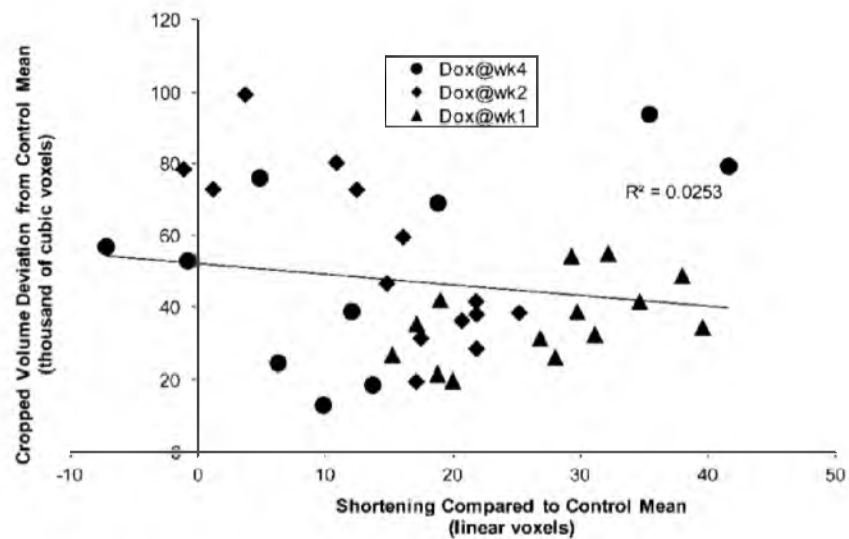


**Figure 7.8.** Femur length deviation correlates poorly with metaphyseal volumetric growth. Phenotypic metaphyseal widening, estimated by the deviation from the control mean in cropped volumes correlated poorly with less shortening, rather than more shortening, thus countering a simple steal phenomenon as the mechanism of shortening. From K. B. Jones, M. Datar, S. Ravichandran, H. Jin, E. Jurrus, R. Whitaker, and M. R. Capecchi, Toward an understanding of the short bone phenotype associated with multiple osteochondromas, *J. Orthop. Res.*, vol. 31, no. 4, pp. 651657. Copyright © 2013 by John Wiley Sons, Inc. Reprinted by permission of John Wiley & Sons, Inc.

shorter length. Induction at later ages resulted in less consistent shortening, but sometimes much greater total bone volumes. The natural variation in severity of osteochondroma formation did not correlate with reduced length. These data lead us to reject the model of a steal phenomenon at work in the pathogenesis of the short bone phenotype.

## 7.2 Applications in Cardiology

Availability of quality cardiac imaging data has led to an increasing number of studies to characterize the morphology and epidemiology of cardiac diseases [24, 25] and also to analyze data from clinical trials [26]. However, many of these images are used to investigate outcomes specific to a study and are not available for wider use [27]. There has been an effort to combine imaging data from multiple studies to build atlases and facilitate the study of population-wide changes in anatomy and function in the context of known cardiac conditions [28]. One example is the study by Lewandowski et al. to characterize differences in cardiac shape between healthy children born premature and those born full-term [29]. An atlas-based method is used to study the regional shape bias in population studies due to differing imaging protocols [27]. Atlas-based methods rely on a template created from a specific training set and thus might be limited in their application. For example, it is difficult to warp pathological shapes to an atlas created from a training set of healthy controls. Furthermore, shape differences related to underlying biological factors such as age are often neglected during atlas creation. The shape modeling methods described in this dissertation do not require a training set and are capable of modeling shape changes related to external factors such as age, thus providing a statistical framework to investigate clinical hypotheses.

This section describes the use of methods from Chapters 4 and 5 toward cardiac shape analysis in the context of ischemia and atrial fibrillation. A group comparison for the ischemia study, corroborating the results of [30], has been included in the MICCAI publication reproduced in Chapter 5. The other applications in this section have not been published previously.

### 7.2.1 Ischemia

One of the major causes of morbidity and mortality in the United States is heart failure caused by coronary artery disease with infarction and the consequent ischemic cardiomyopathy (ICM) [31]. Quantification of shape changes related to heart failure remodeling is challenging due to the nonregular shape of the left ventricle (LV) and the sparse availability of anatomical landmarks in the heart. The method to model nonregular shapes described

in Chapter 5 of this dissertation provides a framework to study anatomic variability and perform hypothesis testing in the context of LV remodeling. This study was performed in collaboration with Dr. Raimond Winslow from the Johns Hopkins University.

The data comprised of 25 end-diastole (ED) cardiac segmentations from 13 global nonischemic cardiomyopathy (NICM) controls and 12 ICM patients. Further description of data is provided in [32]. Four datasets (1 patient and 3 controls) displayed a feature (Fig. 7.9) that might be the result of incorrect segmentation or severe pathology. These datasets were excluded from the population, and the remaining 21 shapes were used to create a statistical model as described in Chapter 5.

The mean shape of the NICM group differed in shape and length of the long axis as compared to the ICM group and also in size and orientation of the opening at the atrial ventricular (AV) junction, as shown in Fig. 7.10. Another interesting observation was the variation in the atrial base point on the LV. These results were found to be consistent with



**Figure 7.9.** Example of skipped dataset: Note the ‘bump’ on the right

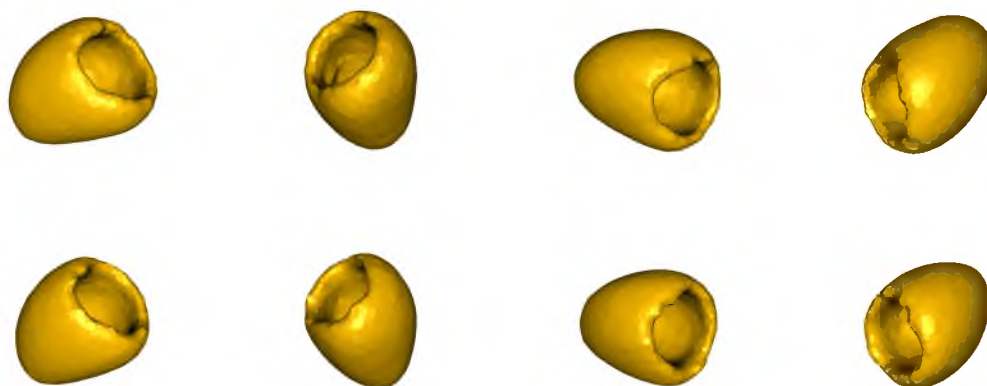


**Figure 7.10.** Multiple views of the group mean shapes: NICM group (top) and ICM group (bottom)

the inferences made from knowledge of the segmentation process. Since the LV wall was well segmented, there was no other source of variability in the images, indicating that the variation at the AV junction was real. Further, as shown in Fig. 7.11, the top modes of variation across groups captured variation in the same features as those described in the analysis of the mean shape.

A qualitative analysis of the within class variation also led to observed differences in the wall thickness between the two groups. This difference has been described as one of the distinguishing features separating the two groups in literature [30]. Further analysis of the differences in the group means is described in detail in Chapter 5.

### 7.2.2 Atrial Fibrillation

Atrial Fibrillation (AF) is a heart condition characterized by chaotic electrical activity and irregular contractions in the atria. AF is a progressive disease, with increasing fibrillation duration and frequency that is correlated with the electrical remodeling of left

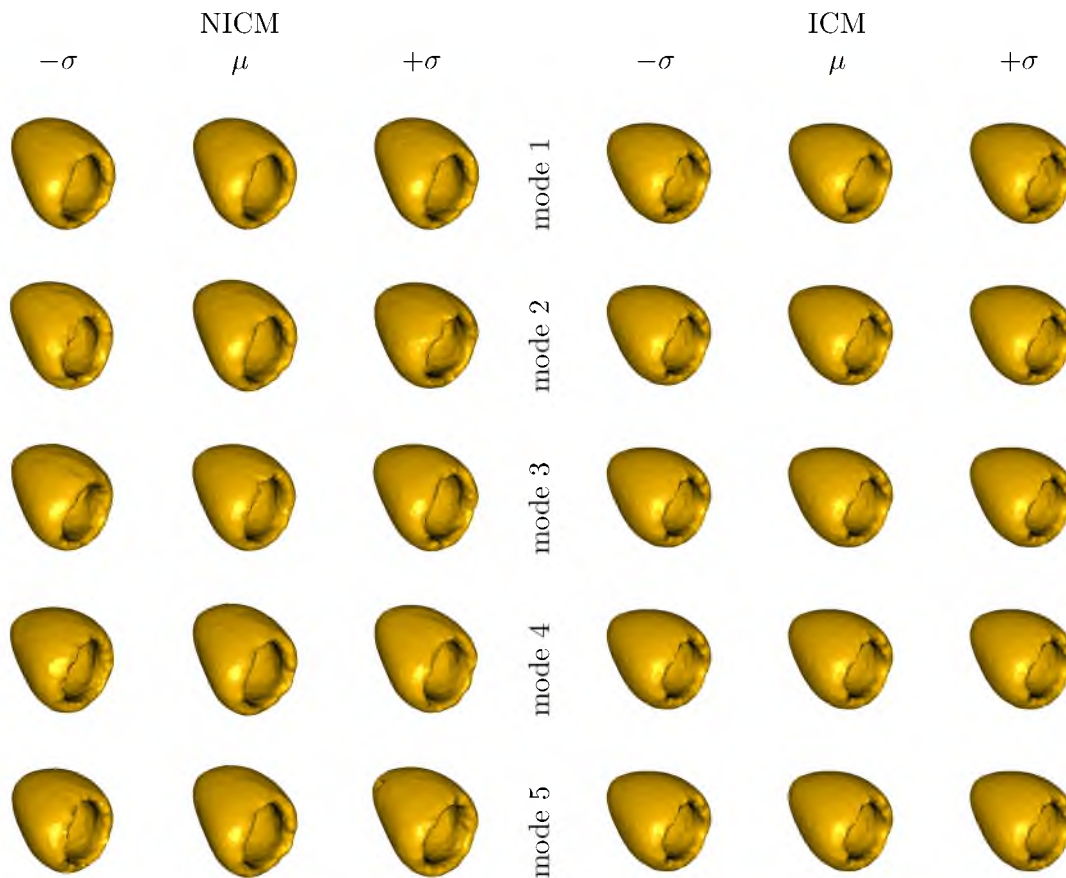


**Figure 7.11.** Group differences across five major modes in the range of  $[-\sigma, +\sigma]$

atrium (LA) tissue and an increase in LA volume. Studies have shown, however, that after successful radiofrequency ablation to cure AF, an enlarged LA often returns to a more normal volume again over time [33]. While volume changes have been observed, there has been little analysis of changes in the *shape* of the LA, which could provide greater insight into the mechanisms behind AF. Shape analysis of the LA is a challenging problem due to the high variability in LA shapes and may benefit from the increased statistical power offered by mixed-effects modeling.

This section describes two studies where the linear mixed-effects model described in Chapter 4 is applied in the context of AF.

### 7.2.2.1 Human Study

In collaboration with Dr. Josh Cates from the Comprehensive Arrhythmia Research and Management (CARMA) Center, the linear mixed-effects shape model described in this dissertation was applied to a proof-of-concept study of LA shape change after successful radiofrequency (RF) ablation.

The data for this study consisted of LA chamber segmentations (excluding the LA appendage) from MRI scans of 12 patients who successfully underwent RF ablation to cure AF. These shapes were retrospectively chosen from a database of patients for ongoing clinical studies at the CARMA Center. All patients underwent late-gadolinium enhancement (LGE) MRI scans and the LA chamber was manually segmented by an expert in cardiac anatomy. A linear mixed-effects correspondence model was constructed using two segmentations for each patient: the first immediately preablation and a second from approximately 3 months postablation. The explanatory variable for the model was time in days from ablation.

Fig. 7.12 shows the intercept shape of the LA model from four different viewing angles. The color encodes the dot product of the fixed-effect slope with the shape normal at that point. The results suggested shrinkage after ablation mainly in the inferior LA and

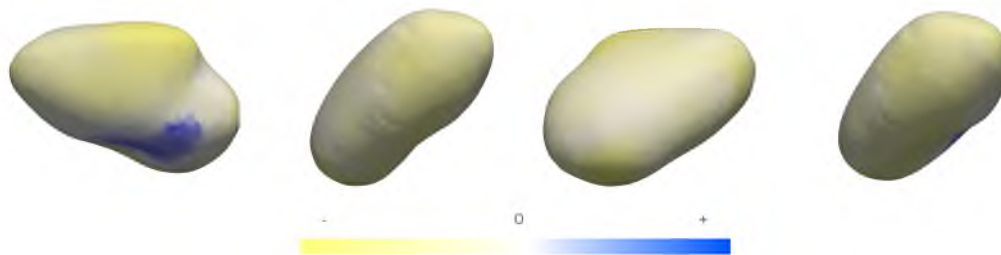


**Figure 7.12.** Visualization of the fixed effects for the left atrium data, (l-r) posterior, sagittal (left), anterior, and sagittal (right), respectively

the posterior region where the pulmonary veins empty into the LA, with some dilation concentrated in the inferior region of the posterior view. Further, an analysis of variance in the random-effects slopes across individuals showed that areas of high intersubject variability on the LA were concentrated around the posterior region, a result consistent with empirical observations in the literature regarding the high variability of pulmonary vein configurations. These shape differences between pre- and postoperative LA shapes was shown to be insignificant by a multivariate Hotelling  $T^2$  test ( $p > 0.05$ ).

These results indicate that mixed-effects models could be used to uncover subtle shape changes beyond simple volume differences and suggest that further investigation with a larger cohort of cases may be warranted to investigate clinical hypotheses regarding LA shape and its relationship to AF.

### 7.2.2.2 Canine Study

In collaboration with Jason Jensen and Dr. Josh Cates from the Comprehensive Arrhythmia Research and Management (CARMA) Center, the linear mixed-effects shape model described in this dissertation was used to investigate population trends in atrial shape change during AF in a canine model.

Data were obtained retrospectively from five different canines, treated according to IACUC standards. AF was induced through rapid atrial pacing (average  $319 \pm 150$  days). Volumetric segmentations of the LA blood pool were created from LGE-MRI using the CORVIEW software (Marreck Inc., SLC, UT). In order to account for high variability in the Left Atrial Appendage (LAA) and pulmonary veins (PV), four models were created for each MRI scan: with PV but without LAA, with neither PV nor LAA, with LAA but without PV, and with both LAA and PV. Canines were grouped according to cardiac phase, with 12 scans in diastole and 16 scans in systole. Linear mixed-effects models were constructed for each group using the number of days paced as the explanatory variable.

Mixed-effects analysis demonstrated trends of local contraction and expansion, consistent across all diastolic and systolic groups. A representative result is shown in Fig. 7.13 and displays the global LA blood pool shapes generated from the mixed-effects model at three time points over the period of pacing. Global trends showed a clear increase in atrial size over time (Fig. 7.13 (a-c)), but also captured the local shape changes (Fig. 7.13 (d)).

A permutation test based on the variance of individual slopes was performed to test the significance of the random-effects and after 100 permutations, indicated that the random-effects were indeed significant ( $p < 0.05$ ). A comparison was also made with the simple linear regression shape model described in Chapter 3, where only the first PCA mode was

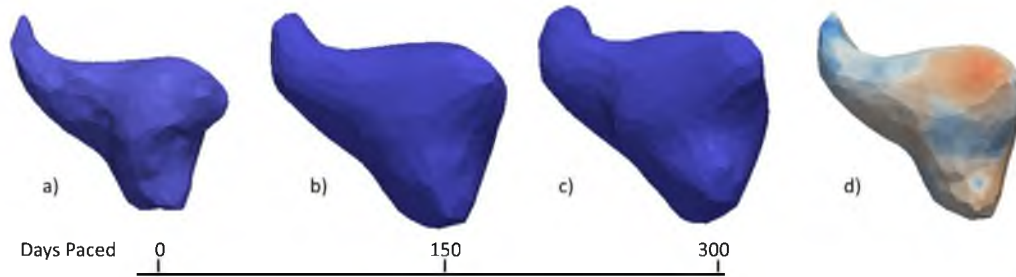


**Figure 7.13.** Representative result of mixed-effects analysis on canine LA shapes. (a–c) Global LA blood pool shape at three time points in long term canine AF model and (d) model demonstrating trends in local expansion (red) and contraction (blue) over time.

found to be statistically significant across groups ( $p < 0.05$ ) and denoted a general increase in size. This was true only for the diastolic category.

The linear mixed-effects model consistently detects subtle atrial shape changes across groups in spite of the variation in anatomy across individuals. Such a model can potentially be leveraged for clinical assessment of AF progression and correlation of shape change to function.

### 7.3 Preliminary Studies

This section describes various studies that were started using the methods described in this dissertation and showed promising preliminary results. These results are yet to be published, but the respective collaborations are currently being pursued with more rigor by various students at the SCI Institute, University of Utah.

#### 7.3.1 Huntington’s Disease

The objective of this study was to make the linear mixed-effects shape model, described in Chapter 4, accessible for further exploration of Huntington’s Disease (HD) based on the longitudinal data made available by the PREDICT-HD study, led by Dr. Hans Johnson at the University of Iowa. Preliminary work was done at the NA-MIC Summer Project Week 2013.

A subset of the PREDICT-HD database, with seven control subjects and six subjects representing varying probability of onset of HD symptom manifestation, was used for this study. All subjects had at least three scans acquired approximately 1 year apart. The input data consisted of five segmented subcortical structures (caudate, globus, hippocampus, putamen, thalamus) each from the left and right hemispheres of the brain, which were manually verified and cleaned [34]. These structures are labeled in Fig. 7.14. These

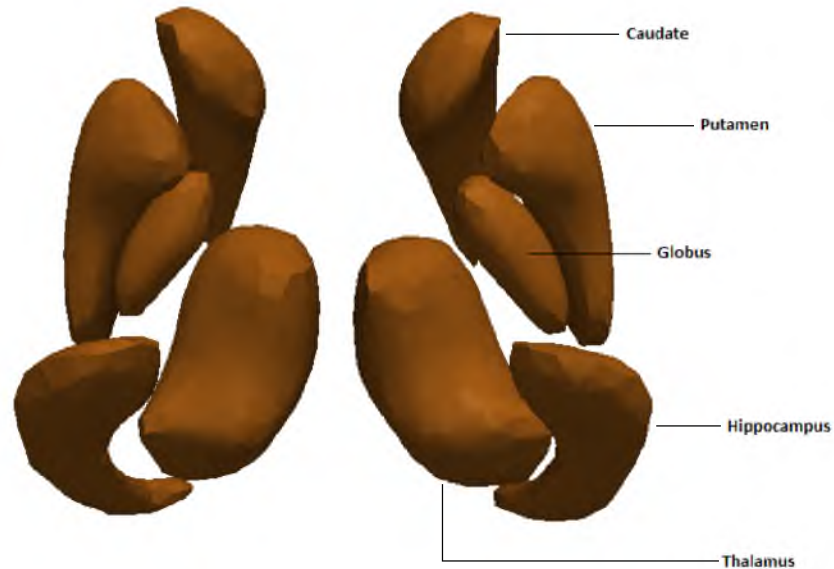


**Figure 7.14.** Subcortical structures segmented for shape analysis for the HD data

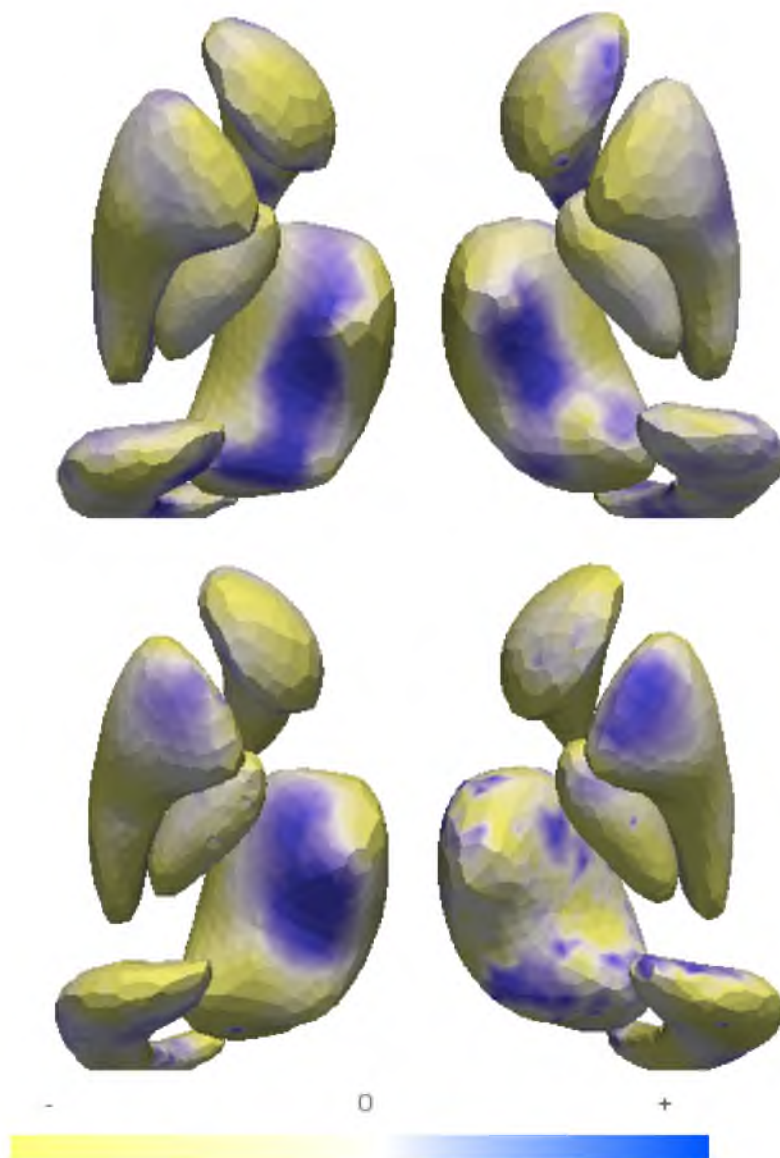
longitudinal data were used to generate a linear mixed-effects shape model as described in Chapter 4.

Fig. 7.15 gives an overview of the fixed-effects trends from the linear mixed-effects shape model. The color map is computed using the fixed-effects slope and indicates local expansion (blue) or contraction (yellow). The local expansion in the thalamus and the tip of the putamen is consistent with the morphological shape changes expected with HD progression. These results are encouraging, but will need to be confirmed with a comprehensive analysis of group differences. This was not carried out in the preliminary study due to the small number of cases available for each group.

### 7.3.2 Acetabular Cartilage in FAI

This study extended the analysis for CAM-FAI described in Sec. 7.1.1 to include the acetabulum shape. The aim was to display shape differences in acetabular cartilage between controls and dysplasia patients to give a preview of how form (i.e., shallow acetabulum) relates to function (e.g., altered cartilage contact pressures). Preliminary work for this study was done in Summer 2012.

The data consisted of 10 segmented acetabular cartilage shapes, with an equal number of healthy controls and patients with hip dysplasia. The major challenge with this dataset was the high amount of variability in the shapes, even within the same group. A statistical shape model was created for the acetabular cartilage using methods for nonregular shapes



**Figure 7.15.** Visualization of the fixed-effects slope for the Control group (top) and the HD group (bottom)

described in Chapter 5.

Dysplasia patients typically have a very shallow acetabulum compared to controls, visible in the shape of both the acetabular bone and the acetabular cartilage. This difference is qualitatively illustrated in the mean shapes as shown in Fig. 7.16, especially in the anterior perspective view. A Hotelling  $T^2$  test also found significant differences in the group means ( $p < 0.05$ ).

These results provide a proof of concept that the methods described in this dissertation can be applied to further analysis of acetabular cartilage shapes, in spite of the high amount of variability inherent in the population. These results have been included in a joint grant proposal between the Department of Orthopedics and the SCI Institute. The collaboration is being extended to the study of other orthopedic applications like design of shoulder implants, which will involve the use of methods from this dissertation to model the scapula.

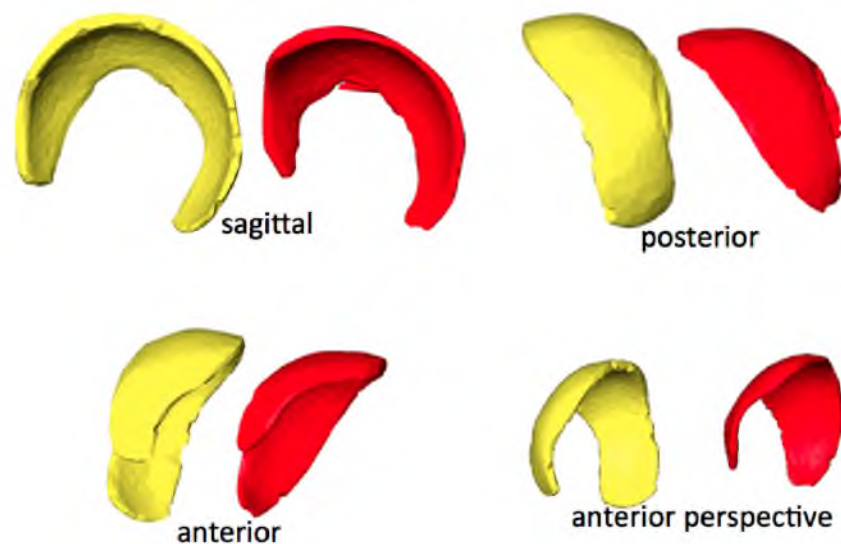


**Figure 7.16.** Four different views of the mean acetabular cartilage shape for the control (yellow) and patient (red) groups

## 7.4 References

- [1] M. Beck, M. Kalhor, M. Leunig, and R. Ganz, "Hip morphology influences the pattern of damage to the acetabular cartilage: femoroacetabular impingement as a cause of early osteoarthritis of the hip," *J. Bone Joint Surg. Br.*, vol. 87, no. 7, pp. 1012–1018, Jul 2005.
- [2] J. S. Gregory, D. Testi, A. Stewart, P. E. Undrill, D. M. Reid, and R. M. Aspden, "A method for assessment of the shape of the proximal femur and its relationship to osteoporotic hip fracture," *Osteoporos. Int.*, vol. 15, no. 1, pp. 5–11, Jan 2004.
- [3] D. C. Barratt, B. B. Ariff, K. N. Humphries, S. A. Thom, and A. D. Hughes, "Reconstruction and quantification of the carotid artery bifurcation from 3-D ultrasound images," *IEEE Trans. Med. Imag.*, vol. 23, no. 5, pp. 567–583, May 2004.
- [4] R. Bryan, P. S. Mohan, A. Hopkins, F. Galloway, M. Taylor, and P. B. Nair, "Statistical modelling of the whole human femur incorporating geometric and material properties," *Med. Eng. Phys.*, vol. 32, no. 1, pp. 57–65, Jan 2010.
- [5] R. Blanc, C. Seiler, G. Szekely, L. P. Nolte, and M. Reyes, "Statistical model based shape prediction from a combination of direct observations and various surrogates: application to orthopaedic research," *Med. Image. Anal.*, vol. 16, no. 6, pp. 1156–1166, Aug 2012.
- [6] S. Almooussa, C. Barton, A. D. Speirs, W. Gofton, and P. E. Beaulé, "Computer-assisted correction of cam-type femoroacetabular impingement: a Sawbones study," *J. Bone Joint. Surg. Am.*, vol. 93 Suppl 2, pp. 70–75, May 2011.
- [7] M. D. Harris, M. Datar, R. T. Whitaker, E. R. Jurrus, C. L. Peters, and A. E. Anderson, "Statistical shape modeling of cam femoroacetabular impingement," *J. Orthop. Res.*, Jul 2013.
- [8] R. Ganz, J. Parvizi, M. Beck, M. Leunig, H. Notzli, and K. A. Siebenrock, "Femoroacetabular impingement: a cause for osteoarthritis of the hip," *Clin. Orthop. Relat. Res.*, no. 417, pp. 112–120, Dec 2003.
- [9] M. Beck, M. Kalhor, M. Leunig, and R. Ganz, "Hip morphology influences the pattern of damage to the acetabular cartilage: femoroacetabular impingement as a cause of early osteoarthritis of the hip," *J. Bone Joint Surg. Br.*, vol. 87, no. 7, pp. 1012–1018, Jul. 2005.
- [10] P. E. Beaulé, E. Zaragoza, K. Motamedi, N. Copelan, and F. J. Dorey, "Three-dimensional computed tomography of the hip in the assessment of femoroacetabular impingement," *J. Orthop. Res.*, vol. 23, no. 6, pp. 1286–1292, Nov 2005.
- [11] K. S. Rakhra, A. M. Sheikh, D. Allen, and P. E. Beaulé, "Comparison of MRI alpha angle measurement planes in femoroacetabular impingement," *Clin. Orthop. Relat. Res.*, vol. 467, no. 3, pp. 660–665, Mar 2009.
- [12] J. C. Clohisy, J. C. Carlisle, R. Trousdale, Y. J. Kim, P. E. Beaulé, P. Morgan,

- K. Steger-May, P. L. Schoenecker, and M. Millis, "Radiographic evaluation of the hip has limited reliability," *Clin. Orthop. Relat. Res.*, vol. 467, no. 3, pp. 666–675, Mar 2009.
- [13] T. C. Pollard, R. N. Villar, M. R. Norton, E. D. Fern, M. R. Williams, D. J. Simpson, D. W. Murray, and A. J. Carr, "Femoroacetabular impingement and classification of the cam deformity: the reference interval in normal hips," *Acta. Orthop.*, vol. 81, no. 1, pp. 134–141, Feb 2010.
- [14] R. Sutter, T. J. Dietrich, P. O. Zingg, and C. W. Pfirrmann, "How useful is the alpha angle for discriminating between symptomatic patients with cam-type femoroacetabular impingement and asymptomatic volunteers?" *Radiology*, vol. 264, no. 2, pp. 514–521, Aug 2012.
- [15] M. D. Harris, A. E. Anderson, C. R. Henak, B. J. Ellis, C. L. Peters, and J. A. Weiss, "Finite element prediction of cartilage contact stresses in normal human hips," *J. Orthop. Res.*, vol. 30, no. 7, pp. 1133–1139, Jul 2012.
- [16] J. L. Horn, "A rationale and test for the number of factors in factor analysis," *Psychometrika*, vol. 30, no. 2, pp. 179–185, 1965.
- [17] L. W. Glorfeld, "An improvement on Horn's parallel analysis methodology for selecting the correct number of factors to retain," *Educ. Psychol. Meas.*, vol. 55, pp. 377–393, 1995.
- [18] K. B. Jones, M. Datar, S. Ravichandran, H. Jin, E. Jurrus, R. Whitaker, and M. R. Capecchi, "Toward an understanding of the short bone phenotype associated with multiple osteochondromas," *J. Orthop. Res.*, vol. 31, no. 4, pp. 651–657, Apr 2013.
- [19] J. V. Bovee, "Multiple osteochondromas," *Orphanet. J. Rare. Dis.*, vol. 3, p. 3, 2008.
- [20] K. B. Jones, "Glycobiology and the growth plate: current concepts in multiple hereditary exostoses," *J. Pediatr. Orthop.*, vol. 31, no. 5, pp. 577–586, 2011.
- [21] D. Stickens, B. M. Zak, N. Rougier, J. D. Esko, and Z. Werb, "Mice deficient in EXt2 lack heparan sulfate and develop exostoses," *Development*, vol. 132, no. 22, pp. 5055–5068, Nov 2005.
- [22] X. Lin, G. Wei, Z. Shi, L. Dryer, J. D. Esko, D. E. Wells, and M. M. Matzuk, "Disruption of gastrulation and heparan sulfate biosynthesis in EXT1-deficient mice," *Dev. Biol.*, vol. 224, no. 2, pp. 299–311, Aug 2000.
- [23] K. B. Jones, V. Piombo, C. Searby, G. Kurriger, B. Yang, F. Grabellus, P. J. Roughley, J. A. Morcuende, J. A. Buckwalter, M. R. Capecchi, A. Vortkamp, and V. C. Sheffield, "A mouse model of osteochondromagenesis from clonal inactivation of Ext1 in chondrocytes," *PNAS*, vol. 107, no. 5, pp. 2054–2059, Feb 2010.
- [24] D. E. Bild, D. A. Bluemke, G. L. Burke, R. Detrano, A. V. Diez Roux, A. R. Folsom, P. Greenland, D. R. Jacob, R. Kronmal, K. Liu, J. C. Nelson, D. O'Leary, M. F. Saad, S. Shea, M. Szklo, and R. P. Tracy, "Multi-ethnic study of atherosclerosis: objectives

- and design,” *Am. J. Epidemiol.*, vol. 156, no. 9, pp. 871–881, Nov 2002.
- [25] S. E. Petersen, P. M. Matthews, F. Bamberg, D. A. Bluemke, J. M. Francis, M. G. Friedrich, P. Leeson, E. Nagel, S. Plein, F. E. Rademakers, A. A. Young, S. Garratt, T. Peakman, J. Sellors, R. Collins, and S. Neubauer, “Imaging in population science: cardiovascular magnetic resonance in 100,000 participants of UK Biobank - rationale, challenges and approaches,” *J. Cardiovasc. Magn. Reson.*, vol. 15, p. 46, 2013.
- [26] A. Pitcher, D. Ashby, P. Elliott, and S. E. Petersen, “Cardiovascular MRI in clinical trials: expanded applications through novel surrogate endpoints,” *Heart*, vol. 97, no. 16, pp. 1286–1292, Aug 2011.
- [27] P. Medrano-Gracia, B. R. Cowan, D. A. Bluemke, J. P. Finn, A. H. Kadish, D. C. Lee, J. A. Lima, A. Suinesiaputra, and A. A. Young, “Atlas-based analysis of cardiac shape and function: correction of regional shape bias due to imaging protocol for population studies,” *J. Cardiovasc. Magn. Reson.*, vol. 15, p. 80, 2013.
- [28] A. A. Young and A. F. Frangi, “Computational cardiac atlases: from patient to population and back,” *Exp. Physiol.*, vol. 94, no. 5, pp. 578–596, May 2009.
- [29] A. J. Lewandowski, D. Augustine, P. Lamata, E. F. Davis, M. Lazdam, J. Francis, K. McCormick, A. R. Wilkinson, A. Singhal, A. Lucas, N. P. Smith, S. Neubauer, and P. Leeson, “Preterm heart in adult life: cardiovascular magnetic resonance reveals distinct differences in left ventricular mass, geometry, and function,” *Circulation*, vol. 127, no. 2, pp. 197–206, Jan 2013.
- [30] E. J. Eichhorn and M. R. Bristow, “Medical therapy can improve the biological properties of the chronically failing heart. A new era in the treatment of heart failure,” *Circulation*, vol. 94, no. 9, pp. 2285–2296, Nov 1996.
- [31] S. A. Hunt, D. W. Baker, M. H. Chin, M. P. Cinquegrani, A. M. Feldman, G. S. Francis, T. G. Ganiats, S. Goldstein, G. Gregoratos, M. L. Jessup, R. J. Noble, M. Packer, M. A. Silver, L. W. Stevenson, R. J. Gibbons, E. M. Antman, J. S. Alpert, D. P. Faxon, V. Fuster, A. K. Jacobs, L. F. Hiratzka, R. O. Russell, and S. C. Smith, “ACC/AHA guidelines for the evaluation and management of chronic heart failure in the adult: executive summary. A report of the American College of Cardiology/American Heart Association Task Force on Practice Guidelines (Committee to revise the 1995 Guidelines for the Evaluation and Management of Heart Failure),” *J. Am. Coll. Cardiol.*, vol. 38, no. 7, pp. 2101–2113, Dec 2001.
- [32] S. Ardekani, R. G. Weiss, A. C. Lardo, R. T. George, J. A. Lima, K. C. Wu, M. I. Miller, R. L. Winslow, and L. Younes, “Computational method for identifying and quantifying shape features of human left ventricular remodeling,” *Ann. Biomed. Eng.*, vol. 37, no. 6, pp. 1043–1054, Jun 2009.
- [33] K. Lemola, M. Sneider, B. Desjardins, I. Case, A. Chugh, B. Hall, P. Cheung, E. Good, J. Han, K. Tamirisa, F. Bogun, F. Pelosi, Jr, E. Kazerooni, F. Morady, and H. Oral, “Effects of left atrial ablation of atrial fibrillation on size of the left atrium and pulmonary veins,” *Heart Rhythm*, vol. 1, no. 5, pp. 576 – 581, 2004.

- [34] E. Young Kim and H. J. Johnson, “Robust multi-site MR data processing: iterative optimization of bias correction, tissue classification, and registration,” *Front. Neuroinform.*, vol. 7, p. 29, 2013.

## CHAPTER 8

### SUMMARY

This chapter concludes the dissertation with a brief summary of the contributions and a discussion of the shortcomings while using the ShapeWorks software. Some directions for future work are also listed.

#### 8.1 Research Contributions

This dissertation extends the PBM framework to enable modeling of shape change over time and also to improve correspondences for populations of complex shapes. The methods are further applied to address specific biomedical problems. Cross-sectional shape regression is introduced, and a novel permutation test is designed to test model significance. Longitudinal analysis of shape populations is made possible via the use of an LME shape model within the PBM framework. Additional features like surface normal entropy and geodesic distance to landmarks are introduced to obtain robust and consistent correspondences across geometrically complex and highly variable shapes.

The general methodology and robust implementation developed in this dissertation is further evaluated in the context of neurological, cardiac, and orthopedic applications. Statistical analysis is performed by extending existing multivariate methods and constructing novel permutation tests. The methods described in this dissertation, combined with the statistical analyses, have provided new ways to explore scientific hypotheses and the results represent a comprehensive validation of the engineering contributions of this work.

#### 8.2 Practical Considerations and Shortcomings

The statistical shape modeling methods described in this dissertation have been successfully applied to a variety of biomedical problems. However, there are some technical shortcomings that require careful consideration. As described in Chapter 2, the ShapeWorks pipeline consists of four stages: preprocessing, initialization, optimization, and analysis. A careful consideration of parameter values and settings is necessary in each of the first three stages. The analysis of results is specific to each hypothesis and has been performed outside

of ShapeWorks for the use cases described in this dissertation. The following paragraphs describe the various parameters and settings to be considered while using ShapeWorks for statistical shape modeling.

### 8.2.1 Preprocessing

An appropriate input to ShapeWorks is a set of implicit surfaces, such as a set of binary segmentations from which a distance transform representation can be computed. Typically, all shapes in a population are not acquired using the same scanner settings, leading to varying geometric parameters (e.g., bounding box). Aliasing artifacts resulting from numerical approximations are also observed in binary masks. Preprocessing such input data is tedious in the current implementation of ShapeWorks and needs to be performed carefully to avoid errors in subsequent stages of the pipeline.

An important consideration is the input geometry. The current implementation requires all shapes to have a common bounding box and the center of rotation (or coordinate  $(0, 0, 0)$ ) to be in the middle of the volume. This requires customized preprocessing steps for each application due to the lack of standardized acquisition settings for shape analysis studies. However, the capability to store and process geometric parameters related to input shapes will help alleviate this problem and aid implementation of generic, automated geometric preprocessing filters.

Further consideration is required while performing Gaussian smoothing to remove aliasing artifacts in the input data since many geometrically complex shapes are sensitive to the smoothing parameter. An incorrect setting may lead to holes in the shapes and result in numerical inaccuracies in further steps of the pipeline. A potential solution to this problem could be the automatic determination of the smoothing parameter based on local feature size.

### 8.2.2 Initialization

In the current implementation of ShapeWorks, correspondence initialization begins with a single particle on each implicit surface. This particle is duplicated, or *split*, to produce a neighboring particle at regular intervals in the initialization process. Initial particle positions can also be provided as a text input. In general, this procedure is reliable for classes of closed shapes with fairly smooth surfaces.

Careful consideration is required for initialization over nonregular surfaces similar to those described in Chapter 5, as particles can easily cross over to opposite sides (for thin structures or sharp features) of such shapes. The surface normal penalty is useful during the

initialization stage for such shapes. It helps initialization near sharp features by constraining not only the position, but also the direction of correspondences across shapes.

Local curvature adaptive sampling is a useful feature in the initialization process. However, it is important to note that the adaptivity parameter is unconstrained and an incorrect value can result in unexpected initial particle configurations or failure of the initialization process. In the current implementation, this parameter is set empirically. However, automatic computation of this parameter based on local feature size may help obtain a more stable initialization.

### 8.2.3 Optimization

The ShapeWorks optimization proceeds as described in Section 2.1, starting with an initial set of particle positions and a set of implicit surfaces (e.g., distance transforms). Optimization based on surface normals or geodesic distance features is highly sensitive to the complexity and variability inherent in the shape population being studied and can be unreliable if parameters are not set using domain knowledge and experimentation. For each of the methods described in this dissertation, the selection of features for optimization is critical and needs to be performed carefully. A learning approach might provide better control over reliability and sensitivity of the optimization process. Practical considerations specific to some of the methods from this dissertation are as follows.

The LME model described in Chapter 4 currently requires that all subjects have the same number of time points. Implementation level changes will be required to accommodate a varying number of time points for each subject. This will be a good feature to have since in theory the LME model has no such restrictions.

The use of geodesic distances described in Chapter 6 helps obtain robust correspondences for nonregular brain shapes, but in spite of an optimized data structure, the associated memory footprint is considerably large. One way to reduce the memory footprint would be to switch from implicit surfaces to surface meshes as inputs, allowing near real time computation of geodesic distances using efficient algorithms (Section 2.2) and releasing memory required to store pairwise geodesic distances. However, careful consideration will be required to extend the surface constraint to the mesh representation.

A similar trade-off is required to use the surface normal entropy as described in Chapter 5. Precomputing surface normals for all voxels is a memory intensive operation, while computing them on-the-fly along with the Fréchet mean and covariance for the entropy computation is computationally intensive and has an adverse effect on the speed of optimization. A practical solution would be to penalize correspondences for deviating from

local the average direction, thereby getting rid of the computationally intensive covariance calculation. However, the weight of this penalty term must then be chosen empirically.

### 8.3 Challenges and Future Work

This section describes the challenges that still remain within the scope of the topics addressed in the previous chapters and also prescribes possible solutions.

#### 8.3.1 Outlier Shapes

The PBM framework assumes a normal distribution in the shape space and models particle position  $p(\mathbf{Z} = \mathbf{z})$  parametrically using an anisotropic Gaussian with covariance  $\Sigma$ . Thus, the ensemble entropy is given as  $H(\mathbf{Z}) \approx \frac{1}{2} \log |\Sigma|$ . In practice, we have  $N$  shapes in  $\mathcal{R}^d$ , each sampled using  $M$  correspondences. Here,  $\Sigma$  is the classical covariance, estimated from the data and given as  $\Sigma = (dMN - 1)^{-1}(\mathbf{P} - \mu\mathbf{1}^T)(\mathbf{P} - \mu\mathbf{1}^T)^T$ , where  $\mathbf{P}$  are the sample vectors and  $\mu$  is the sample mean. This measure uses an  $L_2$  norm, making the model described by this covariance susceptible to outliers.

In order to construct a model description robust to outliers in the shape space, the classical covariance  $\Sigma$  could be closely approximated by the Absolute Deviation (AD) covariance  $\Sigma_{\text{AD}}$ , as described in [1]. The Mean (average) Absolute Deviation (MAD) is an  $L_1$  metric defined as

$$D(\mathbf{Y}) = E[\|\mathbf{Y} - \mu\|] \quad (8.1)$$

From [1], we have

$$c_\sigma = \frac{D(\mathbf{Y})}{\sigma(\mathbf{Y})} = \sqrt{\frac{2}{\pi}} \quad (8.2)$$

Considering  $\Sigma = \sigma^2$  and using (8.1) and (8.2), we can write the AD covariance as

$$\Sigma_{\text{AD}} = \frac{1}{c_\sigma^2} (D(\mathbf{Y}))^2 \quad (8.3)$$

This formulation of  $\Sigma_{\text{AD}}$  from (8.3) can be used in the entropy minimization scheme for the PBM framework. Since  $L_1$  metrics are known to be robust to outliers, it can be assumed that such an estimate of model covariance will be able to deal with outlier shapes.

A potential problem with this strategy may arise if  $\Sigma_{\text{AD}}$  does not preserve the properties of a covariance matrix (e.g., invertability). In such an event, the pseudoinverse may be used to compute an update for the correspondence position. It is also important to note that the results in [1] appear very preliminary and rigorous experimentation will be required to confirm that this paradigm will indeed work.

### 8.3.2 Missing Features

The original entropy formulation prescribed by the PBM framework in Section 2.1 introduces a generative statistical model of the form

$$\mathbf{z} = \boldsymbol{\mu} + \boldsymbol{\epsilon}, \boldsymbol{\epsilon} \sim \mathcal{N}(\mathbf{0}, \boldsymbol{\Sigma}) \quad (8.4)$$

for correspondence, where  $\mathbf{z} \in \mathbb{R}^{Nd}$  is an individual surface modeled as an instance of a random variable  $\mathbf{Z}$ ,  $\boldsymbol{\mu}$  is the vector of mean correspondences, and  $\boldsymbol{\epsilon}$  is normally distributed error.

The system is implemented such that each shape is sampled using the same number of correspondences. As such, there are no features missing in any configuration space. However, in case the ensemble has outlier shapes (i.e., shapes that do not belong to the population, or have missing parts), correspondences on such shapes may be incorrectly optimized. Since the model is described by the mean shape computed using an  $L_2$  norm, it is highly sensitive to such outliers and may fail to generalize. Moreover, the ensemble entropy is computed using distance from this mean, and such outliers affect optimization in the shape space and consequently in the configuration space as well.

One possible solution is to replace the mean shape with the median shape ( $L_1$  norm) in (8.4). Since the  $L_1$  norm is robust to noise and outliers, the median shape is a more robust representative of the ensemble and should not be affected very much by the presence of missing features. The ensemble entropy, computed using distance from the new median, might also provide a degree of robustness against outliers in the shape space as well.

While this formulation has advantages, the biggest challenge is to compute the median shape ( $L_1$  norm) at every iteration of the correspondence optimization process. [2] reports various ways of computing the median shape and also provides an algorithm invariant to rigid transformations. Since the correspondences move incrementally on a static shape ensemble, the computation of the median shape can possibly be allowed to lag for a few iterations without becoming degenerate.

### 8.3.3 Growth Models

Clinicians are not only interested in linear shape changes but would also like to view localized shape changes driven by a clinically relevant growth model to better correlate changes in anatomy with underlying biological parameters like age. It is therefore desirable to substitute the linear model described in Chapter 3 with a nonlinear model of growth, such as the Gompertz growth function [3].

The Gompertz function, given as  $f(t) = \alpha e^{\beta e^{\gamma t}}$ , uses intuitive parameters related to delay ( $\beta$ ), rate of change ( $\gamma$ ), and expected asymptotic value ( $\alpha$ ), which are useful in understanding and comparing growth trajectories. Considering  $f(t)$  to be the Gompertz growth function, the regression model parameter estimation described in Chapter 3 can be replaced with the estimation of the Gompertz parameters  $\alpha$ ,  $\beta$ , and  $\gamma$  using the Levenberg-Marquardt (nonlinear least squares) method. This method has been implemented within the ShapeWorks framework, and preliminary results are promising.

The inclusion of this nonlinear growth model does not change the assumptions or the inferential statistics of the population. However, if additional measurements related to growth (e.g., volume measurements, functional MRI activation maps) are available, it would be promising to look at the changes in these measurements localized to their source on the brain surface and governed by a clinically relevant growth model. With the further aim of modeling trajectories for individual subjects, a Gompertz mixed effects model, similar to the one described by Sadeghi et al. [4], may also be formulated.

## 8.4 References

- [1] D. Falie and L. David, “New algorithms of the absolute deviation covariance and correlation,” in *Proc. COMM*, Jun. 2010, pp. 57–60.
- [2] B. Berkels, G. Linkmann, and M. Rumpf, “A shape median based on symmetric area differences,” in *Proc. VMV*, 2008, pp. 399–407.
- [3] C. P. Winsor, “The gompertz curve as a growth curve.” *PNAS*, vol. 18, no. 1, pp. 1–8, 1932.
- [4] N. Sadeghi, M. Prastawa, P. T. Fletcher, J. H. Gilmore, W. Lin, and G. Gerig., “Statistical growth modeling of longitudinal DT-MRI for regional characterization of early brain development,” in *Proc. ISBI*, 2012, pp. 1507–1510.